

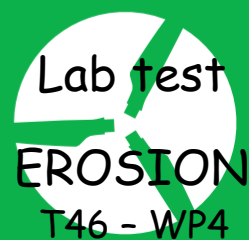
IEA Wind Task 46

Erosion of wind turbine blades

**Review on available  
technologies for laboratory  
erosion testing**

**Technical report**

Edited by William Finnegan and Jakob  
Ilsted Bech



**iea wind**

# **Technical Report**

## **Review on available technologies for laboratory erosion testing of wind turbine blades**

**Prepared for the**

**International Energy Agency Wind Implementing Agreement**

**Prepared by**

**William Finnegan, Jakob Ilsted Bech, Charlotte Bay Hasager, Edmond Tobin, Kirsten Dyer, Nicolai Frost-Jensen Johansen, Ioannis Katsivalis, Fernando Sánchez López, Ian Hamerton, Heiko Blattert, Lena Sühling, Julie Teuwen, Nicolas Quiévy, Ole Bang, Christian Rosenberg Petersen, Søren Fæster, Trevor Young**

**Authors names and affiliations here**

<b>Chapters</b>	<b>Authors</b>
Chapter 1 Introduction	William Finnegan, Jakob Ilsted Bech
Chapter 2 Rain erosion test	Edmond Tobin, Kirsten Dyer
Chapter 3 Impact tests and fatigue	Nicolai Frost-Jensen Johansen, William Finnegan, Kirsten Dyer, Jakob Ilsted Bech
Chapter 4 Viscoelastic properties	Jakob Ilsted Bech, William Finnegan, Ioannis Katsivalis, Trevor Young, Ian Hamerton, Heiko Blattert, Lena Sühling, Fernando Sánchez López
Chapter 5 Fracture mechanics of layered structures	William Finnegan, Jakob Ilsted Bech, Ioannis Katsivalis, Trevor Young, Fernando Sánchez López
Chapter 6 Microstructure and non-destructive analysis	Julie Teuwen, Ian Hamerton, Jakob Ilsted Bech, Nicolas Quievy, Ole Bang, Christian Rosenberg Petersen, Søren Fæster, William Finnegan
Chapter 7 Key conclusions/recommendations	William Finnegan, Jakob Ilsted Bech

**December 2022**

IEA Wind TCP functions within a framework created by the International Energy Agency (IEA). Views, findings, and publications of IEA Wind do not necessarily represent the views or policies of the IEA Secretariat or of all its individual member countries. IEA Wind is part of IEA’s Technology Collaboration Programme (TCP).

## Purpose

This report summarises the current state-of-the-art for laboratory erosion testing of wind turbine blades. This study was completed to provide a baseline for the activities in Work Package 4 of *IEA Wind Task 46 Erosion of wind turbine blades*. This report is released for public dissemination.

**IEA Wind Task 46 Participants during period 2021-2025**

Country	Contracting Party	Active Organizations
Belgium	The Federal Public Service of Economy, SMEs, Self-Employed and Energy	Engie
Canada	Natural Resources Canada	WEICan
Denmark	Danish Energy Agency	DTU (co-OA), Hempel, Ørsted A/S
Finland	Business Finland	VTT (co-OA)
Germany	Federal Ministry for Economic Affairs and Energy	Fraunhofer IWES, Covestro, Emil Frei (Freilacke), Nordex Energy SE, DNV
Ireland	Sustainable Energy Authority of Ireland	SETU Carlow, University of Galway, University of Limerick
Japan	New Energy and Industrial Technology Development Organization	AIST, Asahi Rubber, Osaka University, Tokyo Gas
Netherlands	RVO	TU Delft, Suzlon, TNO
Norway	Norwegian Water Resources and Energy Directorate	Equinor Energy AS, University of Bergen
Spain	CIEMAT	CENER, Aerox Advanced Polymers, CEU Cardenal Herrera University, Siemens Gamesa Renewable Energy, Nordex Energy Spain
United Kingdom	ORE Catapult	ORE Catapult, University of Bristol, Lancaster University
United States	U. S. Department of Energy	Cornell University, Sandia National Laboratories, 3M

## Table of Contents

Purpose .....	4
1 Introduction .....	11
2 Rain erosion test .....	13
2.1 Introduction .....	13
2.2 Whirling arm .....	13
2.2.1 Whirling arm designs.....	13
2.2.2 Wind turbine rain erosion tests standards .....	13
2.3 Water Jet .....	17
2.4 Wind Tunnel .....	17
2.5 Studies on the design characteristics .....	17
2.5.1 Water droplet formation and control.....	17
2.5.2 Test sample design and droplet impact.....	19
2.5.3 Summary .....	22
2.6 Test Parameters.....	23
2.6.1 Natural rainfall intensity .....	23
2.6.2 Droplet size and distribution.....	24
2.6.3 Impact velocity .....	24
2.7 Data presentation and comparison.....	25
2.7.1 Correlation of test facilities.....	25
2.7.2 Transferring RET to real world turbines.....	26
2.8 Reflections on rain erosion test methods .....	27
3 Impact tests and fatigue .....	28
3.1 Introduction.....	28
3.2 Single Point Impact Fatigue Tester (SPIFT).....	29
3.2.1 State of the art .....	30
3.2.2 Results, observations and failure modes .....	30
3.2.3 Relevance and current use for LEE.....	30
3.2.4 Opportunities and strengths .....	30
3.2.5 Limitations and weaknesses.....	31
3.2.6 Availability and access.....	31
3.3 Reflections on impact tests and fatigue .....	31
4 Viscoelastic properties.....	32
4.1 Introduction.....	32
4.2 Tensile test.....	32
4.3 Dynamic mechanical thermal analysis (DMTA) test.....	33
4.4 DMTA tests of two LEP materials .....	35

4.4.1	Methodology.....	35
4.4.2	Results.....	36
4.5	Acoustics.....	37
4.5.1	Ultrasonic Measurement of Speed of Sound of Thin Coating LEP Materials.....	40
5	Fracture mechanics of Layered structures.....	41
5.1	Introduction.....	41
5.2	Tensile pull-off test.....	42
5.3	Damage and fracture of filled elastomers.....	46
5.3.1	Fracture mechanisms.....	46
5.3.2	High strain rate fracture.....	48
5.3.3	Fatigue crack propagation in elastomers.....	49
5.4	Fracture tests for adhesion between polymers and a metal/composite substrate.....	49
5.5	Reflections on fracture mechanics of layered structures.....	51
6	Microstructure and non-destructive analysis.....	52
6.1	Microstructure characterisation (surface).....	52
6.1.1	Microscopy.....	52
6.1.2	AFM.....	54
6.1.3	Spectroscopy.....	55
6.1.4	Chemical structure.....	55
6.2	Gloss.....	56
6.2.1	Visual inspection.....	56
6.3	Microstructure characterisation (through thickness).....	56
6.3.1	Cross-sectional microscopy.....	56
6.3.2	X-ray computed tomography.....	56
6.3.3	Luminescence microscopy.....	58
6.3.4	Scanning electron microscopy (SEM) and Energy Dispersive X-Ray spectroscopy (EDX)	59
6.3.5	Nuclear magnetic resonance (NMR).....	61
6.4	Non-destructive testing methods.....	61
6.4.1	Microscopy.....	61
6.4.2	C-scan.....	62
6.4.3	Terahertz scanners.....	62
6.4.4	Optical coherence tomography.....	66
6.5	Reflections on microstructure characterisation and non-destructive testing methods....	68
7	Conclusions and recommendations for future work.....	70
	References.....	71

## List of Figures

Figure 1: Variation of droplet diameter with water pressure for a range of blunt needle gauges .....	18
Figure 2: Variation of droplet rate with water pressure for a range of blunt needle gauges .....	19
Figure 3: Variation in droplet rate with arm speed for each test sample .....	19
Figure 4: Test samples.....	20
Figure 5: Strike area results for flat plate test sample.....	20
Figure 6: Strike area test results for wedge test sample .....	21
Figure 7: Strike area test results for aerofoil test sample.....	21
Figure 8: Experimental set up of test rig at ETC.....	21
Figure 9: Number of droplets and strikes at varying speeds .....	22
Figure 10: Droplet trajectory at different standoff heights and speeds.....	22
Figure 11: The effect of rotational velocity and flow rate in determining elastic or brittle failure.....	23
Figure 12: Approximate division of strain rate regimes (in $s^{-1}$ ) and the experiments used to investigate these regimes (Siviour and Jordan, 2016), where the range suitable for impact testing has been indicated .....	28
Figure 13: An overview of the different impact testing methods .....	29
Figure 14: Schematic illustration of the SPIFT, on the figure is shown different noncontact instrumentation that can be added during testing.....	29
Figure 15: VN curves generated for 3 different LEP solutions tested in the SPIFT.....	30
Figure 16: Tensile test details, showing an illustration of a sample during the test (left) and typical stress-strain curves (right) as a test output.....	33
Figure 17: Schematic showing the DMTA experimental apparatus showing a dual cantilever sample holder. [image courtesy of Imad Ouchan, University of Bristol] .....	34
Figure 18: Schematic showing the DMTA experimental design in which viscoelastic behaviour is shown as a combination of elastic and viscous responses [image courtesy of Imad Ouchan, University of Bristol].....	34
Figure 19: Schematic showing dynamic mechanical behaviour of a viscoelastic polymer as a function of temperature showing the attribution of different responses to molecular motions. [image courtesy of Imad Ouchan, University of Bristol].....	35
Figure 20: Variation of storage/loss moduli and $\tan\delta$ over temperature for the highest examined frequency (100 Hz) for a) LEP 1 and b) LEP 2 .....	36
Figure 21: a) Storage modulus master curve for LEP 1 and b) $\tan\delta$ variation over a range of frequencies utilizing TTS for LEP 1 and 2 .....	37
Figure 22: Schematic showing the operation of the acoustic analyser, illustrating pulse and echo signals. [image courtesy of Imad Ouchan, University of Bristol]. .....	39
Figure 23: Acoustic analysis of metallic sample (9 cm thick) showing repeated reflections. [image courtesy of Imad Ouchan, University of Bristol].....	39
Figure 24: (Left) Thin Coating LEP used for UT coupon, (Right) Example of how a Time of Flight measurement is used in a tested coupon. Image from (Domenech et al., 2020) .....	40
Figure 25: Average Speed of Sound measurements with the 5 MHz probe.....	40
Figure 26: From Example on how different parts of structure may be loaded at different strain rates (Zhao <i>et al</i> ), 2021) .....	41

Figure 27: Illustration of the pull-off test Actuator Cross-Sectional View (left) and the various failure modes that can be expected (right).....	43
Figure 28: Examples of failure during the pull-out test, showing substrate failure at 10 MPa (left) and cohesive failure (within coating) at 6 MPa (right) .....	43
Figure 29: (a) Pull-off strength testing of composite laminates used for coating adhesion. Images of the failure in the laminate (b) .....	44
Figure 30: Developed peeling testing for interphase coating-laminate adhesion response quantification. (a) Developed specimens; (b) forces on testing; and (c) peeling testing system.....	44
Figure 31: (a) Force of failure for interphase adhesion testing: Coat 1 (Cured), average value of 19.3 N (averaged across six samples, plotted in different colours) and (b) Coat 2 (Semi-cured), average value of 25.1 N (averaged across six samples, plotted in different colours).....	45
Figure 32: Pull-off strength testing of specimen laminates used for LEP coating adhesion: (a) adhesive failure with no-primer intermediate layer application; (b) cohesive failure with primer application (the dolly adhesive effect can also be observed) .....	45
Figure 33: (a) Force of failure for interphase adhesion testing: LEP coating configuration with no-primer application, average value of 9.45 N and (b) LEP coating configuration with intermediate primer layer, average value of 29.31 N.....	46
Figure 34: Craze formation process of craze formation and development into micro crack as well as the toughening effect: (a) the nano-size ridges to indicate the nucleus of craze; (b) the coalescence of ridges to form the embryo of craze; (c) a mature craze consisting of fibrils and voids; (d) the development of craze into crack; (e) the interaction of crazes and the nucleus of new crazes; (f) numerous micro crazes and micro cracks ahead of a blunted crack revealing a toughening effect. From (Fan, Weerheijm and Sluys, 2015) .....	47
Figure 35: Scanning electron microscopy (SEM) images with high magnification (1000×) of coating system A. A, Cracks close to the surface are <i>seen to be closely connected with white elongated particles</i> . B, <i>Surface spalling are observed above white elongated particles</i> . (Mishnaevsky <i>et al.</i> , 2020) .....	47
Figure 36: Principle of recording a crack resistance curve with a single spectrum (Reincke <i>et al.</i> ) ....	48
Figure 37: Crack propagation in synthetic rubber. Crack length [cm] as a function of time [milliseconds] (Mason, 1958).....	48
Figure 38: Experimental and numerical peel curves for variation of the peel test speed. (from (Geißler and Kaliske, 2010)) .....	49
Figure 39: Plane strain tensile test with a crack. From (Eberlein, Fukada and Pasiaka, 2021).....	49
Figure 40: Common fracture specimens used to determine the fracture toughness of bonded interfaces: a) DCB, b) TDCB, c) MMB, d) ENF, e) ELS, f) 4-point ENF specimens. Figure adopted from da Silva, Öchsner (da Silva, Öchsner and Adams, 2011).....	51
Figure 41: Microscopy analysis of damage sample both through light microscopy (left) and height maps (right) [courtesy: Miguel Alonso, TUDelft] .....	53
Figure 42: Typical AFM images showing the changes in surface topology of coated samples due to droplet impact [Source: (Z. Zhang <i>et al.</i> , 2021)] .....	55
Figure 43: Virtual slice through a tomographic reconstruction of leading edge erosion specimen after testing showing cracks between the surface and bubbles within the top coat. From (Leon, Fæster and Rad, 2020) .....	57
Figure 44: Mechanism of ML in SAOED (Vc: interstitial vacancy; Vo: oxygen vacancy). [Image courtesy of Dr Kyungil Kong, University of Bristol].....	59

Figure 45: Cyclic loading along with measuring IR temperature; (a) initial position, (b) maximum position, (c) returning position. [image courtesy of Dr Kyungil, University of Bristol(Kong *et al.*, 2020)].  
 ..... 59

Figure 46: SEM image showing fibre breakage observed after 50 impacts of 20mm hailstones at a velocity around 90m/s [Source: Macdonald2019] ..... 60

Figure 47: SEM and EDX images: A, Scanning electron microscopy (SEM) image of the top coating with four energy-dispersive spectrometry (EDX) images of Si, K, Al, and Ti. [Modified from [Mishnaevsky2019]..... 61

Figure 48: C-scan image of a sample with delaminations due to hailstone impact [Courtesy of Huseyin Eryoruk, TUDelft]. ..... 62

Figure 49: TeraHertz waves are sub-millimetric waves in the electromagnetic spectrum. Picture from: <https://subterandt.com/company/about-terahertz/>..... 63

Figure 50: Illustration of THz pulsed time-domain spectroscopy for single (a) and multilayer (b) coating on metallic substrate. The coating thickness is proportional to the separation between reflection peaks. There is proportional relationship between the amplitude of individual reflections and the relative change in refractive index throughout the corresponding interface. From: [www.teraview.com](http://www.teraview.com)  
 ..... 63

Figure 51: (left) Notus system for non-destructive inspection of coating thickness and adhesion based on THz-TDS spectroscopy technology and (right) extended head position for leading edge inspection. On courtesy of das-Nano. .... 64

Figure 52: Configuration of sample parameters prior to measurement. Courtesy of das-Nano ..... 65

Figure 53: Overview of THz-TDS inspection results. Courtesy of das-Nano. .... 65

Figure 54: (UNPUBLISHED) Proof-of-concept study on defect detection in leading edge coatings for wind turbine blades. (a) Projectile impact crater viewed under microscope. (b) Sample photographs. (c) OCT surface topography from the edge of the impact crater where the surface was still relatively intact. (d) OCT subsurface volume projection from the same area as (c), revealing subsurface voids. (e),(f) OCT cross sections of the voids..... 67

Figure 55. (a) Photograph by Bax Lindhart © 2021 showing the prototype being tested at DTU Fotonik. (b,c) OCT prototype in action scanning marine coatings directly on marine vessels at the Yacht Service wharf in Copenhagen, Denmark. .... 68

## List of Tables

Table 1: List of whirling arm erosion test facilities with significant parameters identified..... 15

Table 2: Summary table of viscoelastic properties at  $10^2$  and  $10^6$  Hz ..... 37

## Executive Summary

This report is the first output of Work Package 4 ‘Laboratory testing of erosion’ in IEA Wind Task 46 ‘Erosion of wind turbine blades’. This initial step of Work Package 4 concentrates on reviewing and assessing the current technologies being employed for laboratory testing of erosion within the wind energy sector, in particular those being investigated by the members of the Work Package 4 collaborating partners rather than an exhaustive list of all possible tests.

In order to review the available technologies for laboratory testing of materials and systems for preventing erosion of wind turbine blades, the tests methods explored are grouped into five categories, as follows:

- Rain erosion tests
- Impact tests and fatigue
- Viscoelastic properties
- Fracture mechanics of Layered structures
- Microstructure and non-destructive analysis

For each of these categories, the relevant test methods were described and discussed, along with key results presented, where appropriate. At the end of the document, an effort has been made to form general conclusions and to identify areas for future investigation that can shape the research agenda to be completed as part of Work Package 4.

# 1 Introduction

This report presents the laboratory tests used to assess the performance of leading edge protection technologies, in particular relating to rain erosion. These tests serve a number of purposes, including: performance rating of leading edge protection; development of new systems and materials; studying erosion mechanisms; determining material properties for modelling; and characterizing environmental degradation. This overview includes description of test parameters and failure modes, where relevant.

Liquid impingement tests, such as the whirling arm rain erosion test (ASTM, 2010), (DNV-GL, 2018), (Fæster *et al.*, 2021) and the pulsating jet test (Zhang *et al.*, 2015), (Hu *et al.*, 2021), (Verma *et al.*, 2021) offer the most direct simulation of rain erosion. The rain erosion process is characterized by repeated impacts causing high strain rates, eventually causing fatigue failure by crack initiation and propagation and by delamination. The whirling arm rain erosion test is the industry standard for testing leading edge protection (ASTM, 2010) (DNV-GL, 2018), where test results are used for benchmarking coatings and for estimation of lifetime (Hasager *et al.*, 2020).

Much of the historical leading edge erosion research focuses on rain erosion, implying that this is the predominant causal factor. However, a recent study (Law and Koutsos, 2020) showed that the impact of excessive airborne particles from seawater aerosols or from adverse local environments, such as nearby quarries, greatly increases the levels of leading edge erosion. Therefore, the current testing of leading edge protection coatings or tapes, which have been developed based on a rain erosion resistivity test, does little to prove its ability to withstand solid particle erosion and may drive coating design in the wrong direction. As a result, a range of other test and characterization methods are used for studying rain erosion and developing new protection, (Pugh *et al.*, 2021). Fatigue tests, high strain rate tests (Siviour *et al.*, 2005), (Sørensen, 2002) and delamination tests (Cortés *et al.*, 2017) are important for characterizing the basic mechanical material properties, which, in part, determine the durability of leading edge protective layers. Other important parameters are microstructure (Mishnaevsky *et al.*, 2020) and layer thickness, where various types of microscopy characterization methods and non-destructive testing play important roles. Knowledge on micro structure, layer structure and mechanical properties are crucial for numerical modelling of impact and erosion, which is used to enhance the understanding of erosion and the role of various parameters as well as developing new, improved materials and protective structures. Finally, the properties of protective layers and materials may change over time due degradation caused by UV exposure, hydrolysis, thermal cycling and other sources of degradation. Such behaviour and material stability is characterized by ageing tests (Xie *et al.*, 2019).

This report aims to summarise the main testing methods that have been employed for assessing the performance of materials and systems used for leading edge protection of wind turbine blades, including methods for investigating their microstructure and non-destructive analysis. Therefore, in this report, the tests methods are grouped into five categories, where each category is given a chapter, as follows:

1. Rain erosion tests, *lead author: Edmond Tobin*
2. Impact tests and fatigue, *lead author: Nicolai Frost-Jensen Johansen*
3. Viscoelastic properties, *lead author: Jakob Ilsted Bech*
4. Fracture mechanics of Layered structures, *lead author: William Finnegan*
5. Microstructure and non-destructive analysis, *lead author: Julie Teuwen*

The overall aim of this report is to review and assess the available technologies for laboratory erosion testing of wind turbine blades. In addition, this report is intended to provide the participants in Work Package 4, along with other participants in IEA Wind Task 46, with an overview of the state of the art and technologies available for testing erosion protection structures and materials.

## 2 Rain erosion test

*Edmond Tobin, Kirsten Dyer*

### 2.1 Introduction

Rain erosion testing is one of the most important test when assessing materials and systems used for leading edge protection of wind turbine blades. Currently there are four main methods known to be in use, which are detailed in this chapter. These are:

1. Whirling arm
2. Pulsating/interrupted water jet on stationary sample
3. Continuous/interrupted water jet on continuously moving sample
4. Wind tunnel testing

### 2.2 Whirling arm

#### 2.2.1 Whirling arm designs

The first testing of materials for resistance to liquid impact began in the 1920's (Honegger, 1924)(Honegger, 1927). This first test method consisted of a steam jet nozzle which was directed at prism shaped samples. The samples were mounted on a disc and the impact velocity was produced rotating the disc though the steam jet. A second "wheel and jet" type rig was described by (Cook, 1928) who rotated a turbine through a spray of water from two jet nozzles. The theoretical droplet impact velocities varied from 140–233  $\text{ms}^{-1}$  over the turbine blade length. Further developments were made in wheel and jet method facilities following the initial designs however, as described by (Heymann, 1979), the main defining aspect of the wheel and jet method is that the number of impacts of the test coupon is directly linked to the number of cycles and number of jets. It should also be noted that the method is theoretically described as a two dimensional impact as the jet is considered constant in the axial direction (Field, Lesser and Dear, 1985). Another issue with the test method is the repetitive impact position, termed as a non-distributed impact.

The whirling arm method incorporates a sample mounted at the end of an arm or arms, which is rotated through an artificial rain field produced by nozzles or needles (Eskilsson, 1965)(Busch *et al.*, 1966)(Hurley and Schmitt Jr, 1970)(Tobin *et al.*, 2011). Despite the relative simplicity of this concept, different design approaches have been tried. Differences between machines lie in their approach to rain-field generation, number of samples, size of samples and shape of samples. The whirling arm with distributed impacts rain erosion tester is presently the de facto test method within the wind turbine industry. With the most common single design being the RET, developed and manufactured by R&D A/S with 13 machines in commission, as of the middle of 2022.

#### 2.2.2 Wind turbine rain erosion tests standards

The following section outlines the present standards for rain erosion testing, in regards to wind turbines.

**ASTM G73 - 10: Standard Test Method for Liquid Impingement Erosion Using Rotating Apparatus**

ASTM G73-10, is an older standard that cover a wide gamut of Test Method for Liquid Impingement Erosion Using Rotating Apparatus. This includes both randomly distributed droplet impacts and repeated impacts at a single point. The standard focuses on identifying the incubation period of a coating, as it recognises that post incubation erosion can behave unpredictably. The standard uses two main rationalisations of the fatigue load, that of total impingement  $H_0[m]$  and the dimensionless number of impacts "specific impacts"  $N_0$ . As further explained in Section 8.6, the use of  $H_0$  and  $N_0$  provides a better foundation for comparing results between testing set-ups like the new SPIFT. However, it does also make it easier to transfer lifetime to real world conditions as results are ideally machine agnostic.

**DNVGL-RP-0171: Testing of rotor blade erosion protection systems**

The DNVGL-RP-0171[39] a newly published recommended best practice, for rotor blade erosion testing. At its core DNVGL-RP-0171 elaborates upon ASTM G73-10, by modifying the testing and data analyses to better suit the new style of tester developed by R&D A/S. This is necessary as ASTM G73-10 is designed to use small test coupons rotating in a uniform rain field, whereas the R&D A/S style tester uses a diverging rain field and long blade samples. This results in a radial speed and rain intensity gradient in the tester as explained in Chapter 8.5. This difference in design also means that incubation detection cannot be performed by mass loss data but rather uses optical methods as described in Section 8.4. There is, however, a point of contention between DNVGL-RP-0171 and ASTM G73-10 in that DNVGL-RP-0171 does not use impingement  $H_0$  as a rationalisation but relies solely on a modified "specific impacts" to failure which in the case of DNVGL-RP-0171 is expressed as impacts/ $m^2$  not the dimensionless  $N_0$  of ASTM G73-10.

**Table 1: List of whirling arm erosion test facilities with significant parameters identified**

<u>Operational Facilities</u>	<u>Type</u>	<u>Arm length</u>	<u>Rain Generation</u>	<u>Drop size</u>	<u>Rainfall Intensity</u>	<u>Velocity</u>	<u>Specimen configuration</u>
<i>UDRI</i>	Rotating Arm	2.44m diameter / 2 arms	96 needles	1.8 - 2.2mm	25.4mm/h	up to 290m/s	rectangular or circular 25.4mm
<i>Polytech</i>	Rotating Arm	3 arms	evenly distributed sprinkler heads	1-2 mm	30-35mm/h	160m/s tip 143m/s middle 126m/s inner	airfoil - 225mm long
<i>SAAB</i>	Rotating arm	1 arm (2.19meters)	6 rain generators, oscillated steel tubes of various diameters	1.2, 1.8 and 2 mm	1.4mm/h to 25mm/h	up to 300m/s	50mm diameter, 5-10mm thickness
<i>WARER (University of Limerick)</i>	Rotating arm	1 arm (0.6m)	36 needles	2mm	25.4mm/h	up to 178m/s	25 mm
<i>RETR Strathclyde University</i>	Rotating arm	2 arms 0.3155m radius	25 needles	1.7 to 2.8mm possible at lower velocities	25.4 mm/h	up to 78m/s	30mm diameter or 30 x 30 x 2mm
<i>Fraunhofer IWES</i>	Rotating Arm			0.5 - 6mm		up to 160m/s	
<i>ETC</i>	horizontal rotating arm		72 needles at 5° each	1.8 to 2.5mm	6l/hr	up to 150m/s	60mm length of R&D AS specimen

<i>NPL</i>	vertical rotating arm with 2 samples		nozzle			up to 500m/s	Flat rectangular 4 x 25 mm
<i>SINTEF</i>	vertical rotating arm with 2 samples and a spray nozzle		nozzle			up to 180m/s	
<i>Darwind</i>	Water Jet with cylindrical cutting of water stream						
<i>R&amp;D AS (at 13 different locations)</i>	Rotating arm	1.23m	600 needles	2.3 to 2.5mm	up to 57mm/hr	to up to 173m/sm/s	airfoil – 450 mm
<b>Status Unknown</b>							
<i>FARM (Naval Air Warfare Centre)</i>	Rotating Arm	1 arm (1.2m)		2 - 2.5mm	12 - 25.4mm/h	134 - 610 m/s	25.4mm diameter, 1.5 to 3mm thickness
<i>RELIUS (BASF)</i>	Rotating arm	2 arms		5 - 6mm	30-35mm/h	up to 140m/s	airfoil ~ 60mm long
<i>DERA (Defence Evaluation and Research Agency)</i>	Rotating Arm			2mm	25mm/h	up to 223m/s	25mm square

Table 1 provides a list of whirling arm test facilities (ASTM, 2010), (DNV-GL, 2018), (Fæster *et al.*, 2021), divided into categories of currently operation, status unknown. Specifics of the design parameters, e.g. one arm, three arms, variable rainfall rate, droplet size, impact speeds, coupon shape, impact frequency/mm, axis of rotation are identified and quantified.

### 2.3 Water Jet

The water jet testing system (Zhang *et al.*, 2015), (Hu *et al.*, 2021), (Verma *et al.*, 2021) has a number of design variations, which includes a stationary sample, moving sample, continuous jet, interrupted jet or pulsating jet (ultrasonics induced).

### 2.4 Wind Tunnel

Patent from Boeing on rain erosion testing using a wind tunnel. Some rigs exist and testing has been completed in them. Patent from Boeing on rain erosion testing using a wind tunnel ([link](#)).

### 2.5 Studies on the design characteristics

Comparisons between different rain erosion test rigs seldom look past a comparison of the difference in time to incubation or failure of the same material to understand the influence of the test rig design and impact characteristics. ORE Catapult, who own and operate an R&D AS RET commissioned the Energy Technology Centre (ETC) in the UK to design and build a pilot rain erosion test rig and undertake studies on the design parameter influences. A whirling arm test rig, water droplet delivery system and test sample geometries were designed, built and commissioned. A test program was developed and undertaken to assess relationships between rig operating parameters, droplet formation, droplet control and droplet impact conditions. A CFD model was also created to allow the influence of other parameters such as specimen length, number of arms and needle location in relation to the sample to be explored

Using results derived from high-speed video footage and high resolution imaging, relationships were developed and observations were made that informed a series of design modifications and upgrades to the rig to improve impact efficiency and further develop droplet control strategies. These included changing from two to a single whirling arm to prevent aerodynamic flow between arms influencing droplet impacts, a new larger and more aerodynamic test sample geometry to capture a greater number of droplet impacts, precision machining to improve circularity of the water pipework on which the single row of needles was located to achieve better droplet control, the addition of shrouds around droplet forming needles to prevent aerodynamic droplet break-up and the location of droplet formers closer to the test sample. The final rig configuration had aerodynamic test samples travelling at up to 120 m/s with repeatable, controllable water droplets of 2.25 mm diameter striking the sample. The precision impact of the droplets in the same location was noted to cause rapid degradation, by up to 87%, of viscoelastic LEPs in comparison to the R&D AS test rig despite having a lower number of droplet impacts.

#### 2.5.1 Water droplet formation and control

Several types of water droplet generation systems were investigated including:

- Spray nozzles
- Rainfall simulators
- Droplet former nozzles
- Hypodermic and blunt needles

Of the four methods explored, the blunt needles were selected as the most suitable method for the proposed rain erosion rig. The principle reasons for this selection of the blunt needles were spray nozzles and rainfall simulators are not able to produce controlled water droplets with precise droplet diameters and drop rates. These methods are suitable for production of rain droplets at the full spectrum of diameters for a given rain intensity, e.g. droplets of 0.5 mm to 3 mm in diameter at 1 mm/hr intensity. Droplet former nozzles are suitable for producing repeatable droplets at a single diameter and drop rate. However, their design is more complex than simple needles and they typically produce water droplets greater than 3 mm in diameter. Hypodermic and blunt end needles have been demonstrated to produce water droplets with controllable diameter and drop rate. Furthermore, these are widely available in a wide range of sizes and configuration, offering maximum flexibility to optimise droplet control.

Tests were performed using a range of blunt needles with a luer lock to control water flow rate. Droplet sizes were observed using a high-speed camera and a mesh grid. The results are shown of droplet size and droplet formation rate against water pressure respectively in the following two graphs.

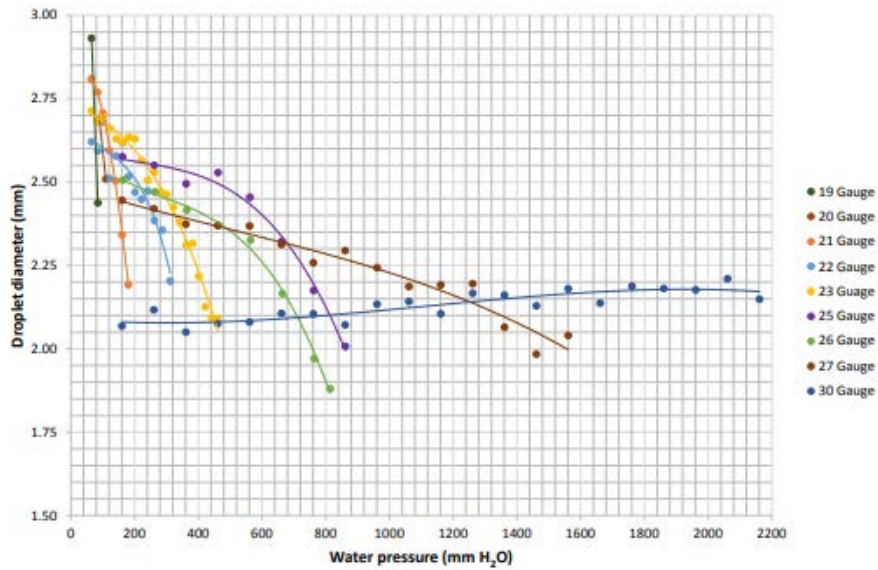


Figure 1: Variation of droplet diameter with water pressure for a range of blunt needle gauges

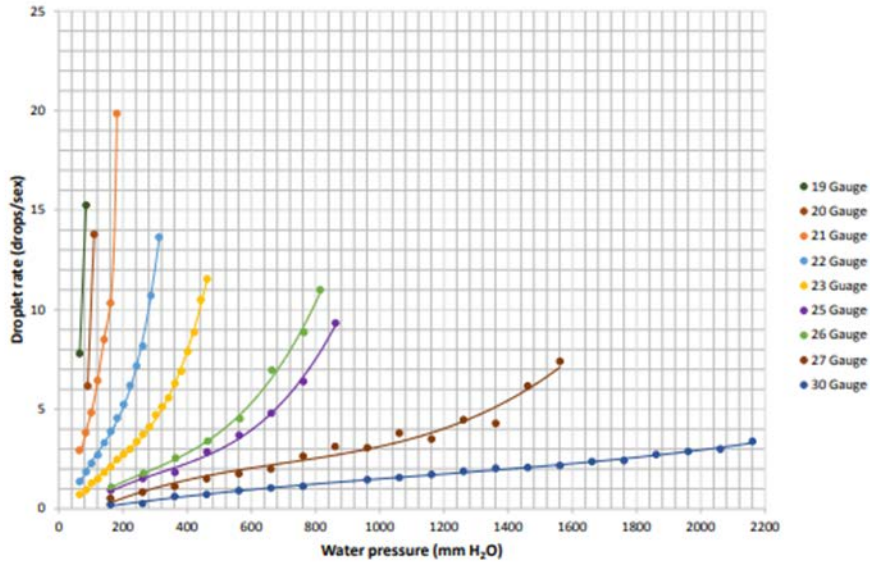


Figure 2: Variation of droplet rate with water pressure for a range of blunt needle gauges

### 2.5.2 Test sample design and droplet impact

Three test sample designs were developed for experimentation on the test rig, namely:

- Flat plate test sample – the simplest geometry for blade/coating manufacturers to produce test coupons for erosion testing
- Wedge test sample – this type of geometry is used in other rain erosion test facilities
- Aerofoil (NACA 0018) test sample – This will be the most aerodynamic geometry and is expected to provide the best test conditions in the test chamber, minimising air swirl and turbulence

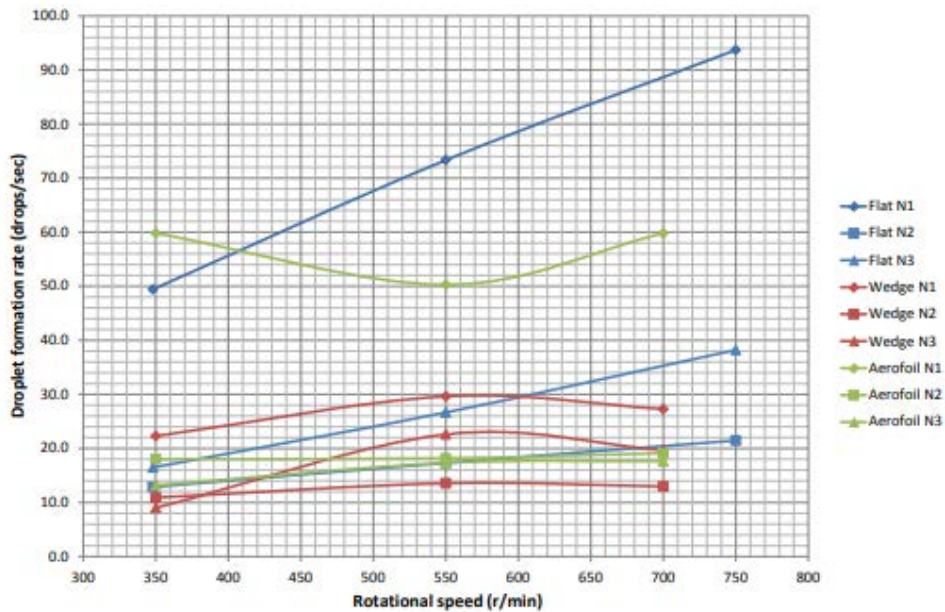


Figure 3: Variation in droplet rate with arm speed for each test sample

In the ETC rig, the rotor plane is very close to the bottom of the needles and it was found that this influenced the droplet formation rate as shown below for the different sample types. In the re-design, shrouds were placed on the needles to remove this effect. It can also be seen that the 1<sup>st</sup> needle droplet formation is significantly more affected than the subsequent needles. The sample geometries, incline angle and rotational speed were also found to affect strike density and location as shown in the following figures.

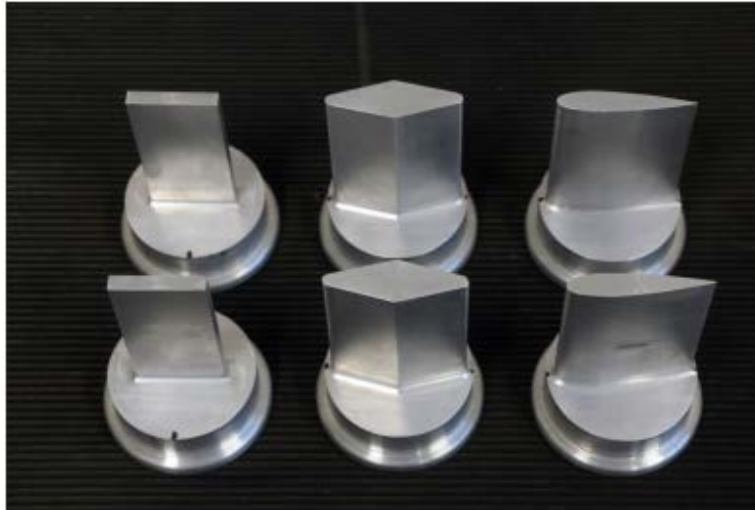


Figure 4: Test samples

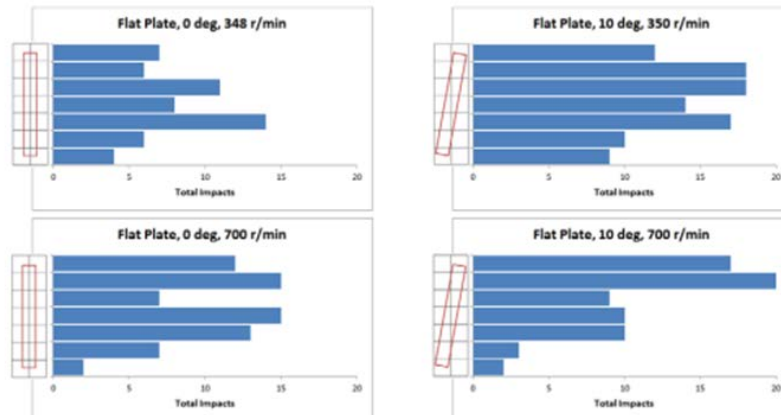


Figure 5: Strike area results for flat plate test sample

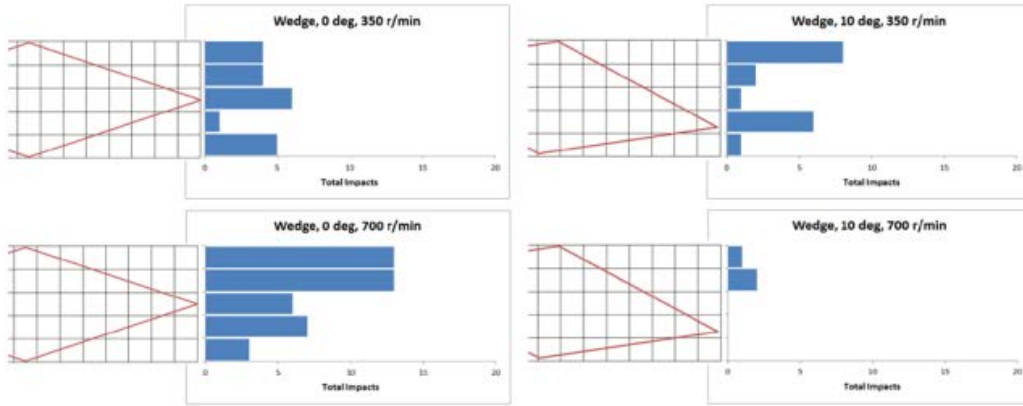


Figure 6: Strike area test results for wedge test sample

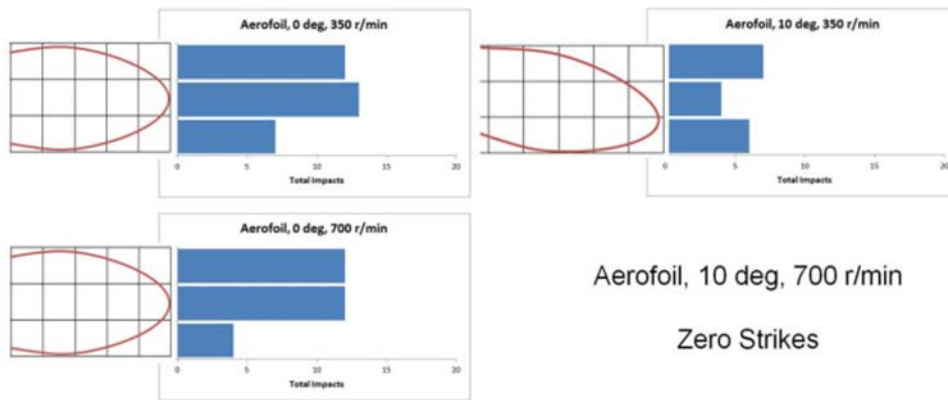


Figure 7: Strike area test results for aerofoil test sample



Figure 8: Experimental set up of test rig at ETC

Due to these effects the test rig was redesigned to a single arm with an R&D AS specimen geometry. On the new design the number of droplet strikes on the sample improved significantly as shown below.

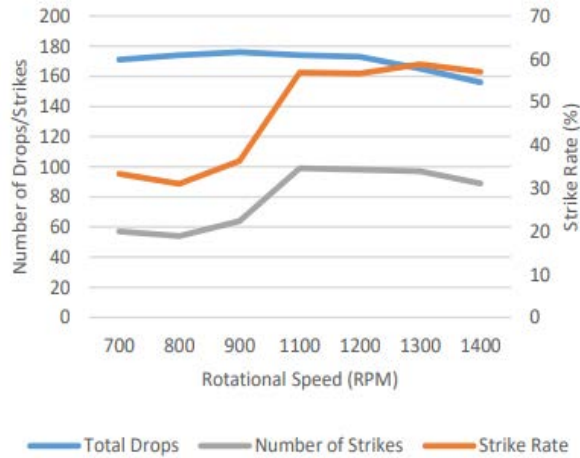


Figure 9: Number of droplets and strikes at varying speeds

A further investigation was performed to see the number of strikes could be altered by increasing the distance between the end of the needle shroud and the rotational plane of the specimen. At higher distances the falling droplets are closer to their terminal velocity but are more susceptible to aerodynamic influences as shown below.

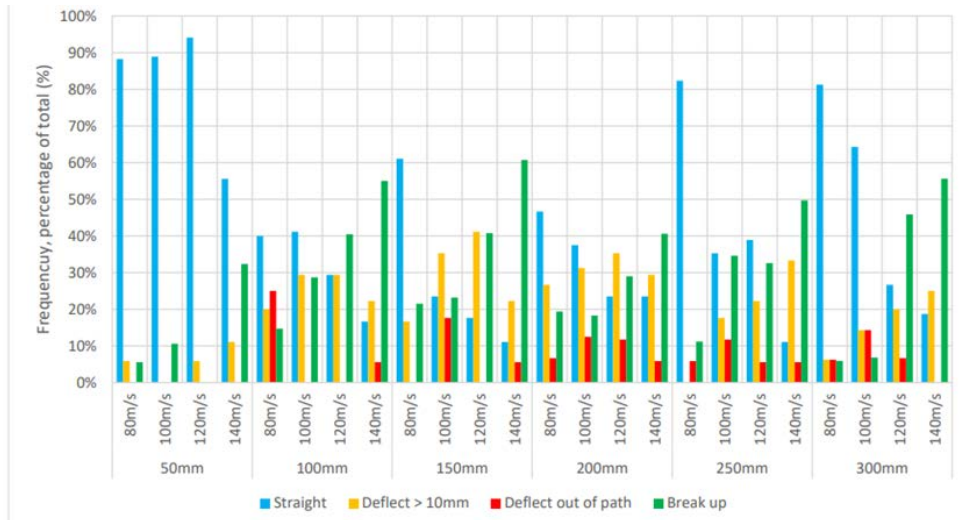


Figure 10: Droplet trajectory at different standoff heights and speeds

### 2.5.3 Summary

The study performed by ETC and OREC showed the complexity of creating droplets of different sizes and creating a repeatable impact density over the sample geometry. Factors which must be included are the droplet formation method, the height of the droplet formation method above the rotating sample, the sample geometry, the angle of the sample, the rotational speed and the flow rate. Underlying many of these factors is the aerodynamic design of the test rig itself. It also showed the very significant influence of the design on the failure of the LEP.

## 2.6 Test Parameters

### 2.6.1 Natural rainfall intensity

There are a number of parameters that are significant in order to simulate natural rain erosion effects; rainfall intensity is one of these parameters. As weather conditions vary widely around the world, rainfall conditions that are prevalent and possible can range considerably. The conditions in temperate climates will be less extreme than those of the tropical regions. Rainfall rates of below 2 mmh<sup>-1</sup> are common in temperate climates and can exist over large areas (1000-1500 km by 300 km) (Ministry of Defence 2000). In tropical climates, rainfall rates of 2 – 10 mmh<sup>-1</sup> are associated with hurricanes and monsoon, existing over a similar area. Heavy convective rainfall refers to 10 – 25 mmh<sup>-1</sup> and is seen over smaller areas of 150 – 200 km by 15 km. Rainfall rates above 25 mmh<sup>-1</sup> are not considered common and occur in general over 1 – 5 km (Ministry of Defence 2000). Extremes occur in all cases with very short minute intervals of up to 120mm/hr possible in UK offshore and temperate climates can also receive very high rainfall rates over short periods of time. Specific areas such as the Himalayas will have a higher incidence rate of these extreme rainfall intensities (Ministry of Defence 2000).

The use of the rainfall rate of 25 mmh<sup>-1</sup> or 25.4 mmh<sup>-1</sup> (1 inch per hour) was proposed as a standardised test variable by Langbein (Fyall and King, 1965). The rainfall rate had been previously used during test campaigns without being standardised (Lapp, Stutzman and Wahl, 1956). It was also stated in two documents (Military Specification 1975, Ministry of Defence 1999) that in order for materials to reach the military specification for radome materials, rain erosion tests should be completed at a rainfall rate of 25.4 mmh<sup>-1</sup> (1 inch per hour) which is the equivalent of the average 2mm droplet size in flight in thunderstorm conditions, the most extreme flight case.

DNVGL RP 0171 and DNVGL RP 0573 do not specify the rainfall intensity that should be used for RET tests on wind turbines despite the rainfall intensity having the second largest influence on the test behind rotational speed. The combination of rainfall intensity and rotational speed has been found by ORE Catapult to be related to a transition in polymer failure mode. This is not seen in metals.

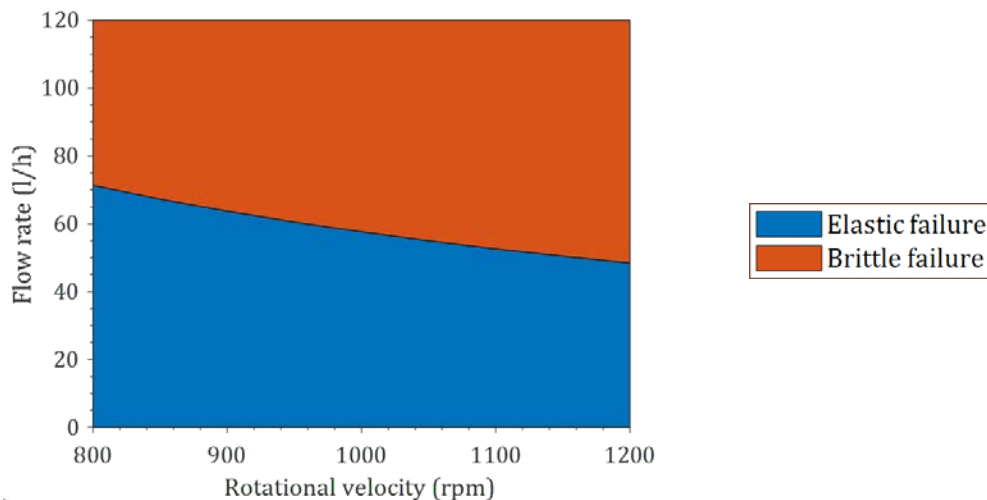


Figure 11: The effect of rotational velocity and flow rate in determining elastic or brittle failure

### 2.6.2 Droplet size and distribution

Within natural rainfall there is a distribution of droplet sizes. A number of researchers have historically published data on experimental observations and methods for numerical modelling this distribution. Data from correlations between radar echoes and rain intensity was published by (Marshall, 1948). This model described the number of droplets of a certain size that occur in rainfall of a particular intensity. This model led to the association of droplet size with rainfall intensity. The associated droplet size is a median droplet size by overall mass within an arbitrary rainfall intensity. This droplet size relationship to rainfall intensity led to rain erosion simulations stating a droplet size along with rainfall intensity when presenting data (Fyall, 1965). It also allowed erosion tests to be conducted with only a single droplet size rather than attempting to produce an artificial rainfall field with a natural size distribution. Further to the work completed by (Marshall, 1948), a number of more recent studies were completed to confirm and update the droplet distribution model (Cherry *et al.*, 1979)(Ulbrich, 1983)(Uijlenhoet, 2001)(Villermaux and Bossa, 2009)(Williams and Gage, 2009). These studies were, in general, conducted to improve the interpretation of radar echoes to give more accuracy in forecasting meteorological events. However, the basic form of the Marshall and Palmer Law is still used.

Along with the rainfall intensity and the droplet size comes the concept of the relative volume concentration of water in the atmosphere. It was noted by (Fyall, 1965) that this was a method of simulating the likelihood of a droplet impact during flight. The droplet concentration is then related to the volume of water in the atmosphere which is another form of the rainfall intensity. Using the droplet concentration, it is possible to estimate the number of theoretical droplet impacts. A key factor in this relationship is the terminal velocity of the droplet (Gunn and Kinzer, 1949).

Rain droplet shapes have also been investigated (Jones, 1959). The shape on impact has an effect on the maximum pressure achieved within the drop due to the effective curvature being a significant parameter. (Jones, 1959) found that the droplet shapes oscillate about a mean shape and that the mean shape varies uniformly with the mass of the droplet.

### 2.6.3 Impact velocity

The test parameter of impact velocity is directly linked to the application in which the material being tested is to be used. The first tests in a whirling arm rig by (Robertson, Lobisser and Stein, 1946) were completed at  $116 \text{ ms}^{-1}$  (260 mph). The material being tested was a glass cloth laminate for a radome application. Further testing for the aircraft industry was completed by (LAPP, STUTZMAN and WAHL, 1954)(Lapp, Stutzman and Wahl, 1956) at velocities between  $67 - 268 \text{ ms}^{-1}$  (150 – 600 mph). An extensive range of materials were tested in a period from 1947 to 1955 at the Cornell Aeronautical Laboratories by Lapp and his colleagues. From this test program, it was stated that  $223 \text{ ms}^{-1}$  (500 mph) was considered the standard test velocity (Lapp, Stutzman and Wahl, 1956). Over the course of the next twenty years, the standard test velocity used for rain erosion testing of aircraft materials was  $223 \text{ ms}^{-1}$  (Wahl, 1965)(King and Gunn, 1970). However, as the types of materials being applied to aircraft changed (specifically, the use of fibre reinforced composite materials), a lower test velocity became relevant. (Schmitt Jr, 1974) mentioned the used of  $178 \text{ ms}^{-1}$  (400 mph) for the test of a polycarbonate material. This was then followed by another reference to testing at the lower velocity by (SCHMITT, 1979). This study involved composite and honeycomb materials, with both test

velocities ( $178 \text{ ms}^{-1}$  and  $223 \text{ ms}^{-1}$ ) being used to investigate the rain erosion resistance of the materials. Another study by (Schroder, 1979) used two test velocities,  $223 \text{ ms}^{-1}$  and  $350 \text{ ms}^{-1}$  to investigate the characteristics of lightning protection coatings. Following on from this, Boeing Commercial Airplane Company produced a series of reports on aircraft surface coatings (Boeing Commercial Airplane Company 1979, 1980, 1983). Within these studies, rain erosion testing, flight time prediction or estimated service life and aircraft in-service testing was completed. The analysis of the flight profile of a commercial aircraft was investigated as part of the estimate service life of the coating. It was found that most severe rain erosion cases occurred at  $223 \text{ ms}^{-1}$  or above; however, relatively long lengths of time were estimated to be spent in the  $178 \text{ ms}^{-1}$  velocity regime during commercial flight operations. Modern test standards for military specifications with the purpose of determining the rain erosion resistance of materials for subsonic aircraft exterior applications, state that rain erosion testing should be completed at  $223 \text{ ms}^{-1}$  (Airbus Industrie 1989, 2001) and with a 2 mm droplet size (Military Specification 2014).

The impact velocity has the greatest influence on the performance of an LEP in the RET test as can be seen in the graph combined with rainfall intensity. DNVGL RP 0573 requires two tests to characterize the behaviour of an LEP for the wind industry HALT at 160m/s tip speed and ALT at 100m/s tip speed.

## 2.7 Data presentation and comparison

### 2.7.1 Correlation of test facilities

Several different experimental test apparatus have been developed, which use different test methodologies that were derived from the specific conditions to be simulated. This has led to a number of difficulties when attempting to correlate test results obtained for different materials or different facilities.

In order to compare and correlate the results from these varying test methods, the variables need to be identified. Droplet size, impact frequency, rainfall intensity and impact velocity are the main variables that drive the testing conditions. The effect these variables can have on test results has been discussed in detail previously by (Field *et al.*, 1994). Standard test procedures and methods have also been developed ASTM G73-10, and a standard set of test conditions are outlined in by the Ministry of Defence (1999). However, the test conditions are generally set by the individual facility and often depend on the materials and flight conditions that are to be replicated. In general, the mean penetration depth of the erosion is used as the correlating parameter. This parameter is derived from mass loss measurements and the use of the density of the material to calculate the volume removed. The exposed area, or the erosion scar area, is measured and the volume is then divided by this area to give a mean depth. This process however, does not work effectively for coated materials as the density will inevitably vary between coating and substrate materials. New 3D surface measurements, detailed in ISO 25178-2:2012 for example, can enable direct volume loss measurements to be obtained; however, the accuracy, measurable area, computational time and power required, and cost for this type large-scale visualisation, means that such techniques are not widely used.

A significant inter-laboratory study, which involved a ten different liquid impact erosion test facilities, was described by (Heymann, 1979). Six of the facilities were the typical type whirling arm rain erosion method with droplets, while four facilities used cylindrical jets. Of these four facilities, three were the

typical wheel and jet method while one was an arm and jet type. A series of five different metallic materials along with perspex and neoprene coating were tested. Statistical analysis for the results allowed for formulas to be produced that could predict rationalised and normalised erosion resistance of materials. A detailed explanation of the formulas is given in (Heymann, 1970). Severity factors were calculated for each facility based on the results, with dependences calculated for droplets and jets. However, it was noted that the erosion rates predictive accuracy was much better than that of the incubation period. The results from these tests and formulas are included in ASTM G-73-10, although the calculation of these correlations is difficult due to the large number of parameters to be quantified.

Attempts to correlate water-jet test facilities with whirling arm test facilities have been previously undertaken (Deom and Balageas, 1995)(Tobin *et al.*, 2011)(Tobin, Young and Raps, 2012). Infrared transparent materials were used by (Deom and Balageas, 1995) and the incubation time was used as the correlating factor. The percentage transmission loss was measured on samples of Ge, ZnS and MgF<sub>2</sub> tested at various impact speeds, and a 10% loss in transmission was defined as the optical incubation time. In this case a correlation factor of 1.21 was used to convert the measured 0.8 mm jet impact velocity to a calculated equivalent 2 mm droplet impact speed for the water-jet test. This factor gave a good correlation with the observed results from the whirling arm test. A number of correlation studies were completed to relate in-flight rain erosion to laboratory results (Methven and Fairhead, 1960)(Schmitt Jr, 1968). The main issue in these studies was the ability to quantify the actual conditions that the aircraft operated in, which led to large inconsistency in the correlation of the results – specifically, the quantification of the droplet size distribution and the actual instantaneous rainfall rates.

### **2.7.2 Transferring RET to real world turbines**

As the goal with performing RET testing is to evaluate the life time, it is worth considering how to transfer the results to real world turbines. This is very much a non-trivial task and no easy formula or factor exists that can transfer a given amount of hours into one universal lifetime. The problem is that over an assumed 25+ year lifespan different turbines are likely to experience wildly different meteorological conditions. Here in order to evaluate the erosion potential of a given site, high temporal resolution rain data is needed. Another problem is that despite the large number of turbines in operation, which can potential yield real world coating life data, the material and RET data are essentially unknown.

One approach, as used by Eisenberg (Eisenberg, Laustsen and Stege, 2018), has been to use meteorological data and in-field observations of erosion and combined this with the Springer model to fill in the blanks when RET data was missing. It is claimed in the paper that the model shows good correlation to real world turbines. However, as the underlying material and meteorological data is proprietary, it is difficult to verify or use this model. Furthermore, there are several limitations to the Springer model in regards to non-linear materials. Another approach is the one used by Jakob Ilsted Bech in (Bech, Hasager and Bak, 2018). This model uses high temporal resolution rain and wind data from DMI (the Danish Meteorological Institute) measured at selected locations in Denmark.

Detailed RET testing was then conducted on a reference coating, in a whirling arm RET. Rationalisations was used to generate a reference curve for the coating life. Then, based on the the meteorological times series, all rain events were evaluated for the damage potential. Afterwards, the

real world lifetime was calculated using Palmgren-Miner (Palmgren, 1924). This model is still in development, but shows promise as a method for transferring RET results to real world conditions. However, as the availability of high temporal resolution rain data is limited, using this model is outside of the scope of this thesis. The hope is that at some point a tool similar to the New European Wind Atlas (NEWA) could be made for rain erosion potential.

ETC parametric study on droplet dynamics. CFD analysis completed at ORE, DTU, and Fraunhofer – Tobias Weis.

## **2.8 Reflections on rain erosion test methods**

There is potential future work in possible new design characteristics for rain erosion testing in a laboratory setting.

Further issues that are still of concern that could be addressed, in general, are:

- **Recovery:** Many modern LEPs are viscoelastic and have time dependent behaviour. On a wind turbine rain periods are interspersed with dry periods where there is potential for viscoelastic recovery to occur. This has been noted to influence the time to failure in RET tests via inspection periods or non-test periods over the weekends.
- **Single droplet size / droplet size distribution:** Different droplet sizes induce different stresses into LEPs as shown by FEA models. The influence in RET of testing only one droplet size compared to a real world distribution is not yet understood.
- **Sequencing:** Combined high velocity-intensity tests show embrittlement of the polymer, whilst lower velocity-intensity test show ductile failure. And as mentioned above dry periods could allow recovery. The order of sequence in which they occur could be critical if the embrittlement is sufficient to be unrecoverable.

### 3 Impact tests and fatigue

Nicolai Frost-Jensen Johansen, William Finnegan, Kirsten Dyer, Jakob Ilsted Bech

#### 3.1 Introduction

One of the defining characteristics of rain erosion on blade coatings is that it results from fatigue damage that is induced from many smaller impacts. Therefore, at a minimum, the duration of these impacts must be:

$$t = d/v$$

Where  $d$  is the diameter of the droplet and  $v$  is the impact speed. For example, for a wind turbine operating with tip speeds of approximately 100m/s that is impacted by  $\varnothing$ 1mm droplets will result in a minimum impact duration of approximately  $10 \times 10^{-6}$ . With modern soft polyurethane coatings, local deformation above 10% is possible resulting from these droplet impacts, resulting in a shock loading, which can be deduced from Figure 12.

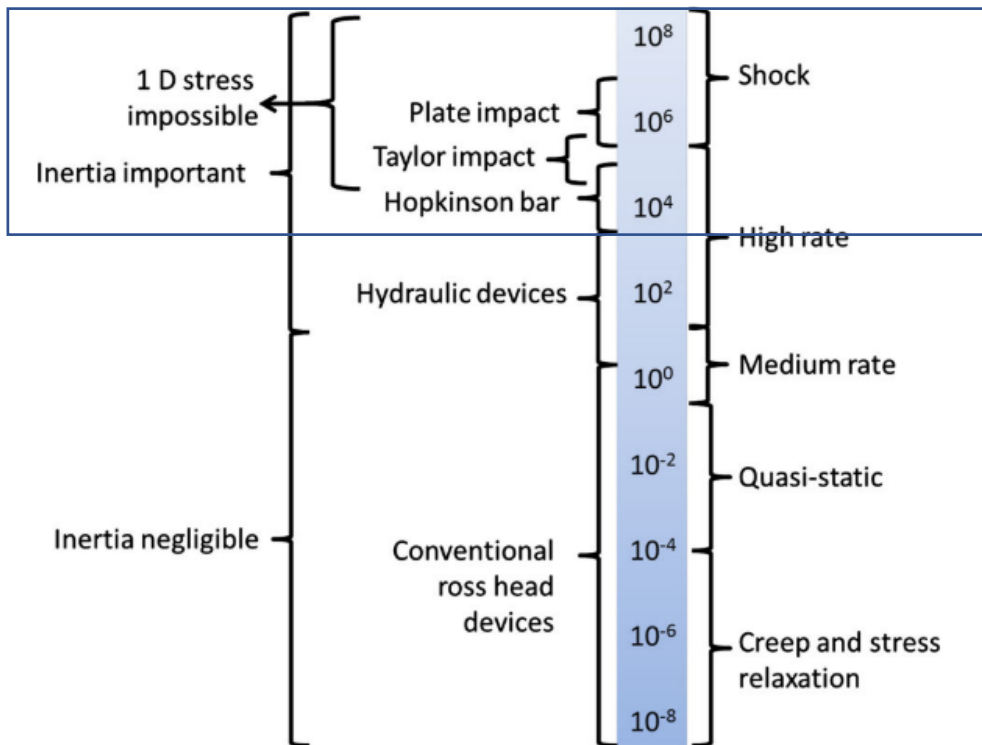


Figure 12: Approximate division of strain rate regimes (in  $s^{-1}$ ) and the experiments used to investigate these regimes (Siviour and Jordan, 2016), where the range suitable for impact testing has been indicated

Therefore, during laboratory-scale mechanical testing, it is essential that these load conditions are replicated. This chapter aims to outline some of the methods presently available and give suggestions

for other methods that might provide additional information. Broadly, impact testers have been separated into two groups, which is illustrated in Figure 13:

- Testing for fatigue
- Testing for material properties

Figure 13 gives an overview of the testing technologies considered for each category (in blue) and the resultant primary output data from each test (in orange).

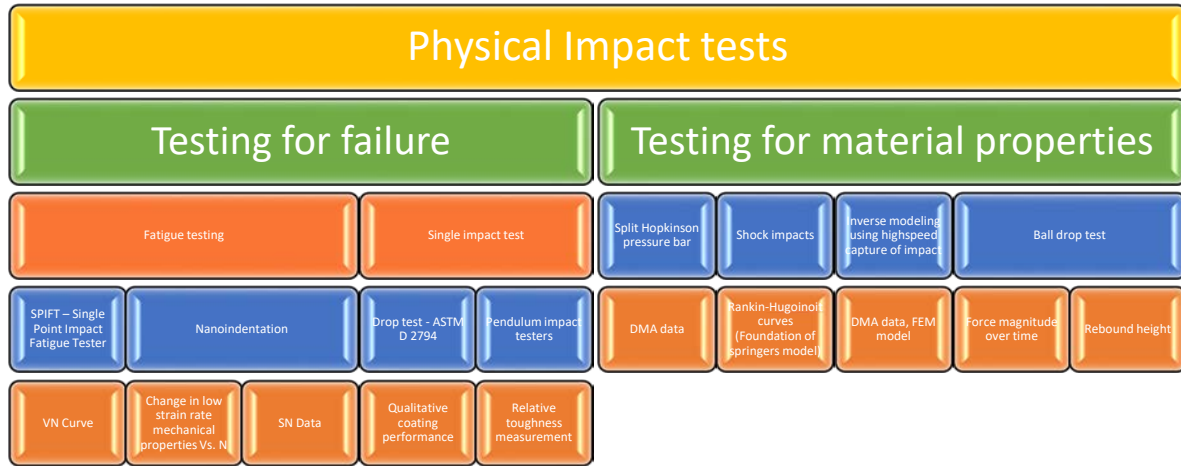


Figure 13: An overview of the different impact testing methods

In this chapter, the Single Point Impact Fatigue Tester (SPIFT) is discussed, considering how the method may aid in coating development and characterization, where the main goal is to induce failure in the coating or material. The erosion of modern materials is, in most cases, best described as a fatigue process, and not as failure resulting from single impacts.

### 3.2 Single Point Impact Fatigue Tester (SPIFT)

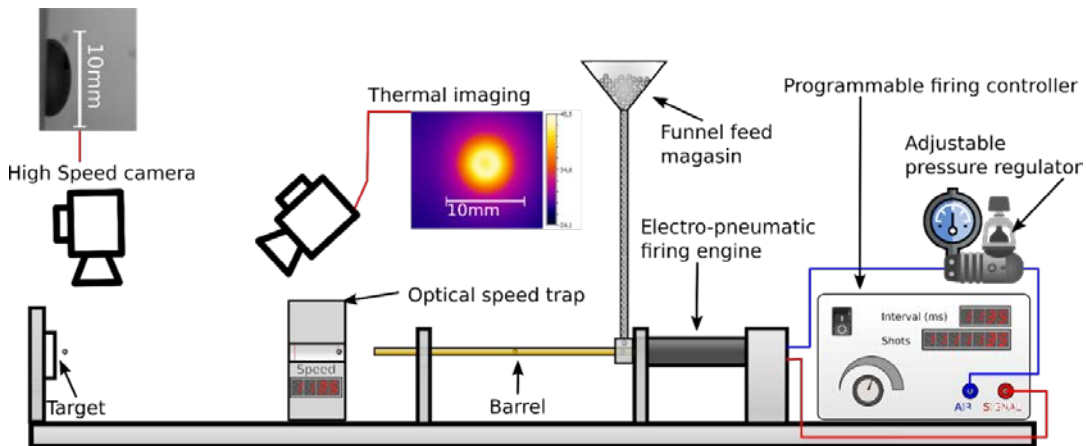


Figure 14: Schematic illustration of the SPIFT, on the figure is shown different noncontact instrumentation that can be added during testing.

### 3.2.1 State of the art

The Single Point Impact Fatigue Tester (Fraisie *et al.*, 2018)(Adler, 1999) aims to generate a repeated and controlled impact under the following conditions:

- Impact speed:
  - 90 – 170 m/s
- Impact rate:
  - 0-5Hz
- Projectile properties:
  - 0.14g
  - 6mm diameter
  - Nitrile rubber
- Impact energy

### 3.2.2 Results, observations and failure modes

The main result from the SPIFT is generated VN curves as seen in Figure 15.

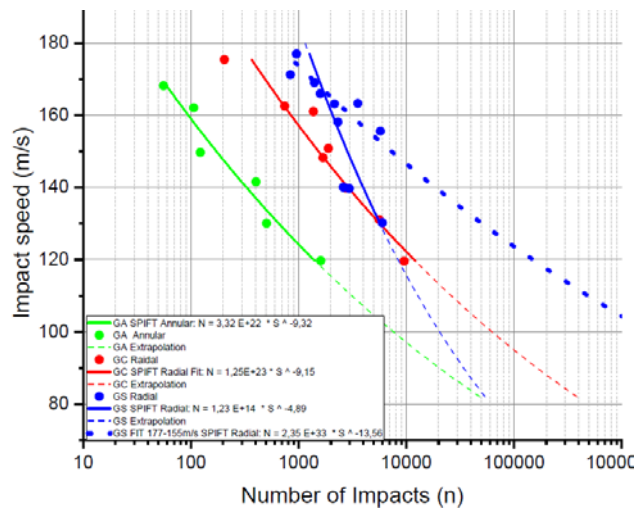


Figure 15: VN curves generated for 3 different LEP solutions tested in the SPIFT

### 3.2.3 Relevance and current use for LEE

Presently it is one of the few tools available to us that is capable of inducing mechanical impact fatigue, and it is part of the modelling workflow being developed within the Duraledge project.

### 3.2.4 Opportunities and strengths

Due to the relative simplicity of the test, there are many possibilities for in-situ instrumenting the test. Examples of these is the use of in-situ microscopy to evaluate the incubation point. Infrared thermography to measure surface temperature and temperature distribution. High-speed video in order to observe the full impact. Acoustic Emissions equipment, which can detect internal damage

during test. The biggest strength of the SPIFT is that the impact rate can be controlled from 0-5Hz this combined with thermography allows for testing without the problem of accumulating heating resulting from viscoelastic effects.

### **3.2.5 Limitations and weaknesses**

Presently the test is limited to 6mm projectiles; this is very large compared to real droplets. The SPIFT induced damaged cannot be directly transferred to rain erosion performance without an advanced material model. Presently the test is not actively cooled so any test will be at or above ambient temperature.

### **3.2.6 Availability and access**

Presently, there is only one SPIFT located at DTU RISØ. The setup is an operational prototype at an approximate TRL of 7. The SPIFT is available for collaborative project work, e.g. the work done in association with Kingston on graphene reinforced PU.

## **3.3 Reflections on impact tests and fatigue**

Using the modelling framework from Duraledge, we aim to verify that by combing VN curves from SPIFT with DMA data that it is possible to predict incubation when comparing to a whirling arm RET. We are considering constructing a higher version 2 tester at a higher TRL level better suited for continuous testing. We are considering to add a climate chamber in order to be able to test a sub ambient conditions.

Potential future projects could include:

- Investigate the effect of impact rate in fatigue performance
- Compare the results of the SPIFT with the results from a water jet test
- High speed video measurement of coating deformation/material model validation
- Testing new coating formulations in flat panels
  - The effect of reinforcing particles

## 4 Viscoelastic properties

*Jakob Ilsted Bech, William Finnegan, Ioannis Katsivalis, Trevor Young, Ian Hamerton, Heiko Blattert, Lena Sühling, Fernando Sánchez López*

*Drop impact on wind turbine blades is related with high strain rates. To understand and model the response at high strain rates of materials, polymers in particular, dynamic tests are required (Siviour and Jordan, 2016)*

### 4.1 Introduction

As discussed in Section 3, a high strain rate regime is induced due to the impact of rain and particles on wind turbine blades. Therefore, to understand and model the response at high strain rates of blade and leading edge protection materials, polymers in particular, dynamic tests are required (Siviour and Jordan, 2016). Polymers are viscoelastic materials *i.e.* their dynamic mechanical behaviour has both viscous and elastic components. This means that there is dependence on time and frequency which influence whether the material behaviours predominantly like a purely elastic solid, or a Newtonian fluid (Ferry, 1980). The time dependence means that if the stress on a polymer is held constant, then the strain increases with time (termed creep), whereas if the strain is held constant, the stress decreases with time (which is termed relaxation). Viscoelastic polymers have the ability to recover from deformation (unless a yield point has been exceeded resulting the covalent bonds having been broken), but hysteresis occurs on cyclic loading due to dissipation of mechanical energy. The effective stiffness depends on the rate of the application of the load (strain-rate dependence) and polymers also show a temperature dependence.

Therefore, this chapter discusses tensile testing for baseline material properties of materials and the most suitable test for investigating the viscoelastic properties of a material: dynamic mechanical thermal analysis (DMTA) test. In addition, the use of acoustics for non-destructive analysis for determining the viscoelastic properties of coating materials is discussed.

### 4.2 Tensile test

During the tensile test, a specimen is stretched at a constant speed until it breaks. The force and the elongation are measured, where the tensile stress acting on the specimen is defined as the quotient of the measured force and the initial cross-sectional area of the specimen. DIN EN ISO 527-3 specifies how the tensile strength of films and sheets is determined. The typical stress-strain graphs that are the main output from the tensile test are shown in Figure 16. The first curve is measured for brittle materials, while the second and third curves are the result of measuring tough materials with a yield point. Tough materials without a yield point result in curve four.

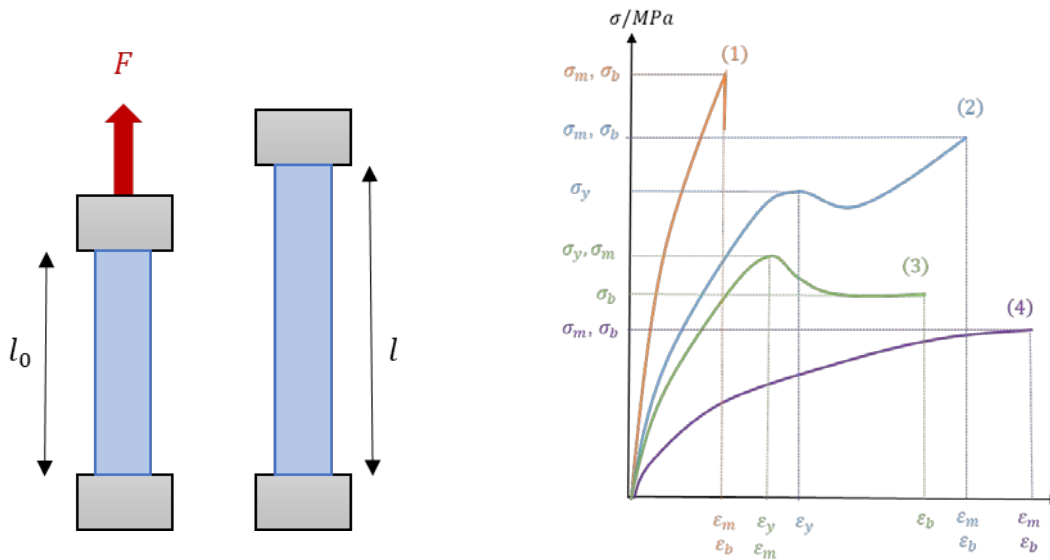


Figure 16: Tensile test details, showing an illustration of a sample during the test (left) and typical stress-strain curves (right) as a test output

The ASTM D412 ‘Standard Test Methods for Vulcanized Rubber and Thermoplastic Elastomers’ provides standard methods and conditions for determining the tensile stress, tensile strength and yield point of the materials. The failure with elastomers, which are typically the leading edge protection coatings, sees a deformation fracture after a lot of necking (long necking region) due to its high ductility. Therefore, this would be loosely classified as Model 1 fracture due to the tensile load. Due to the high elongation of the specimens, other testing methods are often sought to assess the material properties of the leading edge protection systems. Therefore, there hasn’t been much work done on this for this specific application but at a smaller-scale for biomedical applications (Kanyanta and Ivankovic, 2010) and in exploring the tensile strength of particle reinforced elastomeric composites (Lee, 2016). In addition, there has been work completed that investigates the fracture properties of polyurethane-based materials that have been combined with other materials, including blending with plasticized PVC (Ha *et al.*, 1998), particle reinforced elastomeric composites (Lee, 2016) and surface-modified carbon nanotube composites (Tayfun *et al.*, 2017).

The tensile test can be used to determine and compare mechanical properties of LEPs. It is possible to determine the mechanical behaviour at different temperatures. In the wind energy sector, testing ranges between - 30 °C and 50 °C (DNVGL-RP-0573).

### 4.3 Dynamic mechanical thermal analysis (DMTA) test

Dynamic mechanical analysis (and its close relative dynamic mechanical thermal analysis) allows interrogation of dynamic material properties under controlled conditions (*e.g.* at variety of temperatures, heating rates, oscillation frequencies, and strain rates) (Menard and Menard, 2020). DMTA measures individual material viscoelastic characteristics, but is limited to small deformation ranges (where linear viscoelasticity behaviour is observed). The behaviour is dependent on amplitude,

strain rate and temperature and so the practical experiment involves the controlled oscillation of a material (typically in the form of an oblong sample held in a single or dual cantilever fixture), which can be seen in Figure 17.

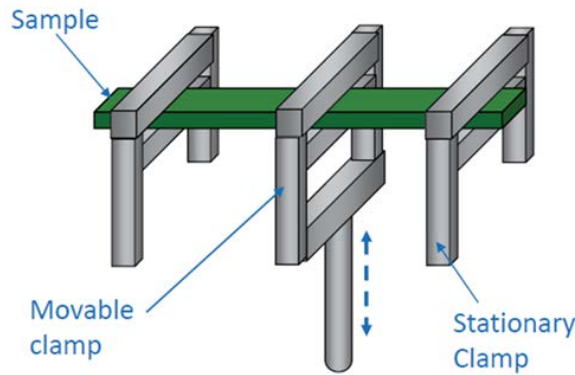


**Figure 17: Schematic showing the DMTA experimental apparatus showing a dual cantilever sample holder. [image courtesy of Imad Ouchan, University of Bristol]**

The viscoelastic behaviour is probed by recording the data as a combination of elastic and viscous responses. The more elastic the material, the shorter the phase lag,  $\delta$ , the greater the viscous response, the larger the lag. The degree to which the response is out of phase with the applied force (usually quoted as the tangent of the phase angle) of the lag ( $\tan\delta$ ) giving an indication of its damping characteristics of the material, which is shown in Figure 18.

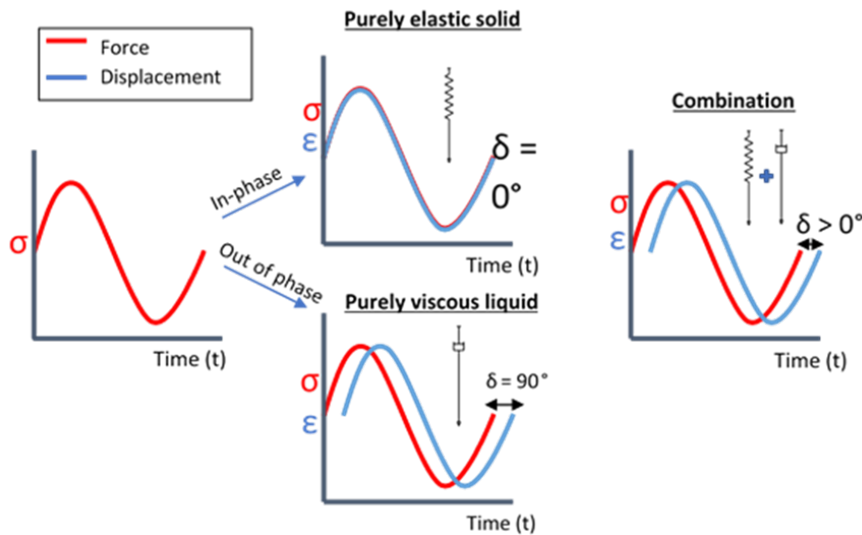


**Figure 18: Schematic showing the DMTA experimental design in which viscoelastic behaviour is shown as a combination of elastic and viscous responses [image courtesy of Imad Ouchan, University of Bristol].**

A common temperature sweep DMTA experiment in which the oscillation frequency is held constant while the temperature is raised at a fixed rate (Figure 19) allows the changes in modulus to be acquired as a function of temperature. These can be related to chemical or structural features which are influenced by *e.g.* chemical packing such as the degree of crystallinity (in semi-crystalline polymers) or the crosslink density (in cross-linked networks) and thus the glass transition temperature,  $T_g$ .

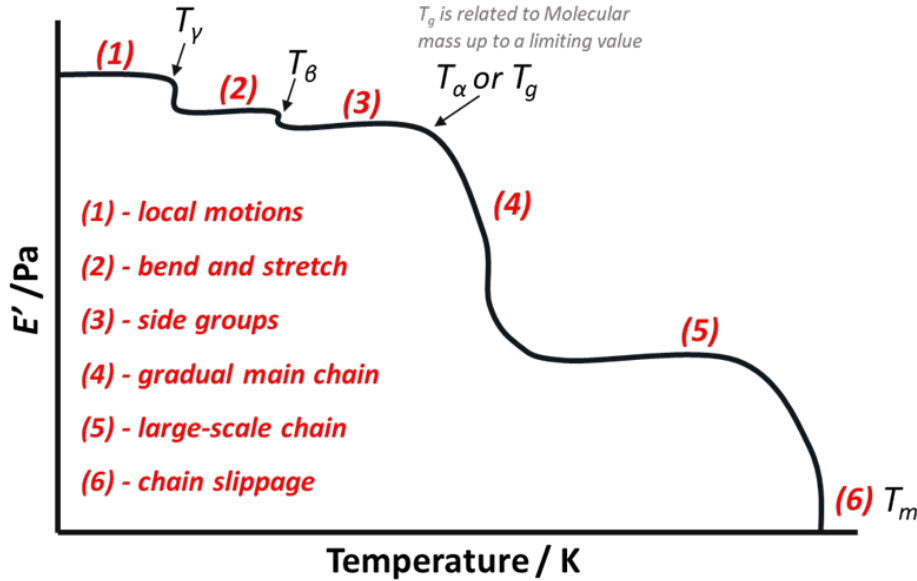


Figure 19: Schematic showing dynamic mechanical behaviour of a viscoelastic polymer as a function of temperature showing the attribution of different responses to molecular motions. [image courtesy of Imad Ouchan, University of Bristol].

Consequently, the DMTA technique may be used to probe changes in the structure that might occur due to erosion and ageing. For example, a reduction in crosslink density through chain scission/bond cleavage would reduce the effective molecular weight of the network, thus reducing *e.g.*  $T_g$  and modulus by facilitating main chain motion. Similarly, a change in the degree of crystallinity of a semi-crystalline polymer (*e.g.* resulting from work hardening or thermal annealing (Tcharkhtchi *et al.*, 2014) and cooling) would also lead to discernible changes in the melting temperature ( $T_m$ ) or the thermal transitions due to the entanglement or alignment of side groups (Galeski, 2002).

#### 4.4 DMTA tests of two LEP materials

##### 4.4.1 Methodology

DMTA testing was carried out aiming to characterize the viscoelastic properties of the two LEP materials tested, where more detailed results are given in (Katsivalis *et al.*, 2022). Due to the flexible and soft nature of the tested LEP materials, the tensile mode of DMTA was used. Temperature sweep tests (temperature range:  $-80^\circ\text{C}$  to  $80^\circ\text{C}$ ) were performed for different frequencies (1, 10, 45, 100 Hz) aiming to identify the variations of storage and loss moduli, and also, the energy dissipation potential of each material by identifying the value of  $\tan\delta$ .

Rectangular thin specimens, with dimensions 20 x 5 x 1 mm, were cut from the LEP material sheets and were used for the DMTA testing which was conducted according to (ASTM, 2015). The amplitude of the applied extension was 10  $\mu\text{m}$  which resulted to a strain of about 0.05% and thus ensuring no plastic deformations were introduced to the specimens. During DMTA, the load and extension are recorded and are converted to stress and strain; thus, allowing to calculate the elastic and damping components of the stiffness response of the specimens.

The Time Temperature Superposition (TTS) (Siviour and Jordan, 2016) principle was used to adjust the DMTA data to the high strain rates experienced during RET by creating master curves for the storage/loss moduli and  $\tan\delta$  over a range of frequencies.

#### 4.4.2 Results

Figure 1 shows the variation of the storage/loss moduli and  $\tan\delta$  for the highest frequency examined (100 Hz) for both materials. A similar material behaviour was observed; at lower temperatures, the polymers are at their glassy state with very high values for the storage modulus. As temperature increases, the polymers enter the glass transition region, they become softer, and the loss modulus and  $\tan\delta$  reach their peak. After the glass transition, with increasing temperature, the rubbery region follows and both storage and loss modulus decrease significantly. Increasing the testing frequency leads to a shift of the glass transition and the peak of the  $\tan\delta$  at higher temperatures.

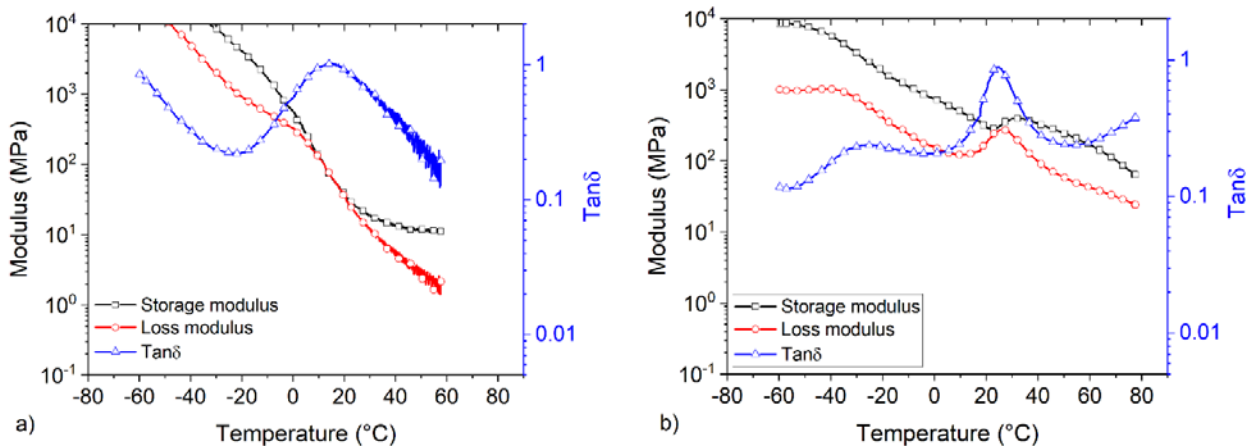


**Figure 20: Variation of storage/loss moduli and  $\tan\delta$  over temperature for the highest examined frequency (100 Hz) for a) LEP 1 and b) LEP 2**

TTS suggests that there is an analogy in the strain rate and temperature response of viscoelastic materials. More specifically, polymer materials are stiffer in lower temperature and higher strain rates and softer at higher temperatures and lower strain rates. Considering that the strain rates generated during droplet impacts are in the region of  $10^6$  Hz (Herring *et al.*, 2019), it was considered beneficial to utilize TTS to estimate the stiffness response of the LEP materials at such strain rates.

The data extracted from the different frequencies were used to create master curves for the storage/loss moduli taking as a reference point the data at 17°C. Figure 4a shows a characteristic master curve for the storage modulus of LEP 1 while Figure 4b shows the  $\tan\delta$  as a function of strain rate for both examined LEP systems. Table 1 summarizes the storage and loss moduli along with the

$\tan\delta$  at 17°C (temperature inside the WARER chamber during testing) for the highest examined frequency (100 Hz) and for a frequency representative of the droplet impacts ( $10^6$  Hz).

**Table 2: Summary table of viscoelastic properties at  $10^2$  and  $10^6$  Hz**

Frequency:	$10^2$ Hz			$10^6$ Hz		
Material	Storage modulus (MPa)	Loss modulus (MPa)	$\tan\delta$	Storage modulus (MPa)	Loss modulus (MPa)	$\tan\delta$
LEP 1	38.00	32.17	0.85	664.78	323.3	0.49
LEP 2	299.41	112.08	0.37	401.59	91.56	0.29

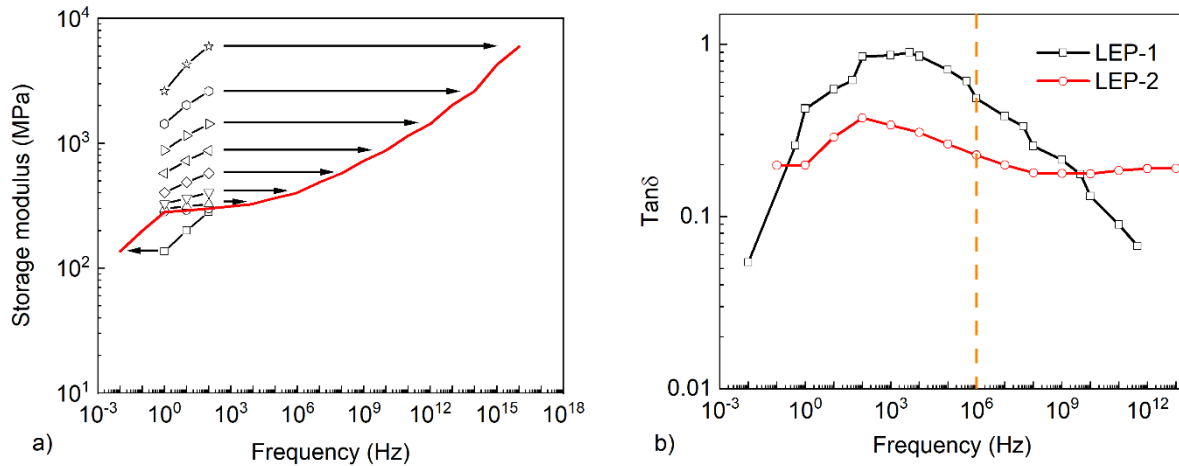


**Figure 21: a) Storage modulus master curve for LEP 1 and b)  $\tan\delta$  variation over a range of frequencies utilizing TTS for LEP 1 and 2**

#### 4.5 Acoustics

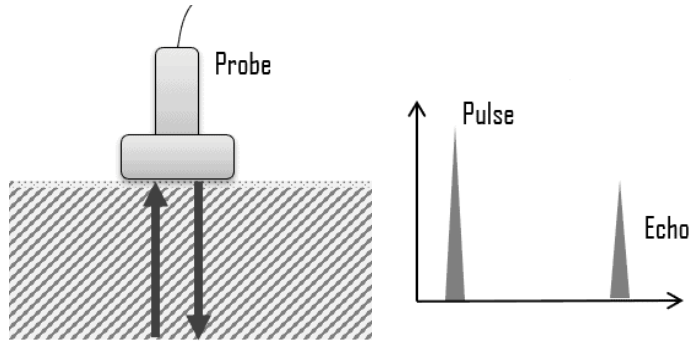
The speed of sound of viscoelastic materials is directly related with its modulus of elasticity (Brinson and Brinson, 2015). The viscoelastic characterization of the LEP materials at the appropriate working frequency range is limited for dynamic tests based on the vibration of rods or beams (Beda *et al.*, 2013) and possible using ultrasonic waves (Sasmita *et al.*, 2019). Moreover, the use of the ultrasound technique in thin film applications has additional issues as coupled thickness layer determination (Grate, Wenzel and White, 1992). It is important to point out here that the frequency sensitivity of ultrasound velocities is usually weak, of order tens m/s/decade, as described in (Sinha and Buckley, 2007) but since it depends mainly on the polymers relaxation and  $T_g$ , it may be a remarkable source of property variations in the erosion performance analysis.

The ultrasonic technique is an important procedure for viscoelastic materials' characterization at high strain rates. It is broadly used for developing precise measurements of speed of sound and attenuation. These two variables are the bases for accurately evaluating elastic moduli, and for assessing mechanical properties at high frequencies. Layer thickness and the speed of sound are important linked parameters also to account for LEP system configuration. If one of the parameters is known, the other one can be determined by simple time-of-flight (TOF) measurement of ultrasound.

An ultrasound examination is based on the propagation of ultrasonic waves in the part to be examined and the follow-up of the transmitted signal (called transmission technique), or of the signal reflected or diffracted by any surface or discontinuity (called reflection technique). Both techniques can use a single probe that acts as a transmitter and receiver, or a double probe, or separate transmitter and receiver probes. In the same way, the following two techniques can involve an intermediate reflection coming from one or more surfaces of the examined object:

- The transmission technique (ISO 16823 'Non-Destructive Testing—Ultrasonic Testing—Transmission Technique') contains a more detailed description of this technique) is based on the measurement of the signal attenuation after the passage of an ultrasonic wave through the examined part.
- The reflection technique (pulse echo technique, (ISO 16810 'Non-Destructive Testing—Ultrasonic Testing—General Principles' and ISO 16811 'Non-Destructive Testing—Ultrasonic Testing—Sensitivity and Range Setting') uses the reflected or diffracted signal from any interface of interest inside the examined object. This signal is characterized by its amplitude and its position on the time base, the latter being a function of the distance between the reflector and the probe. The location of the reflector is determined by knowledge of this distance, the direction of wave propagation, and the position of the probe. Contact with the test object is generally preferred over separation by a liquid buffer or immersion coupling medium. Although it is applicable, in general terms, to discontinuities in materials and applications, other techniques like the time-of-flight diffraction (TOFD, ISO 16828 'Non-Destructive Testing—Ultrasonic Testing—Time-of-Flight Diffraction Technique as a Method for Detection and Sizing of Discontinuities') can be used for both detection and sizing of discontinuities provided is performed with necessary consideration of geometry, acoustical properties of the materials, and the sensitivity of the examination.

Current analytical methods use a pulse-echo technique (J. Zhang *et al.*, 2021) *i.e.* measuring the time it takes a fixed pulse (typically from a 10 MHz transducer) to travel through the sample and back again allows us to calculate the speed of sound in the medium, shown in Figure 22.



$$\text{Speed of sound} = \frac{\text{Distance travelled}}{\text{Time of Flight}}$$

**Figure 22: Schematic showing the operation of the acoustic analyser, illustrating pulse and echo signals.**  
 [image courtesy of Imad Ouchan, University of Bristol].

When testing an ideal case (*i.e.* a monolithic metal) multiple discrete clear peaks (showing repeated reflections) are visible, each diminishing with each reflection from which transit times can be determined (Figure 23).

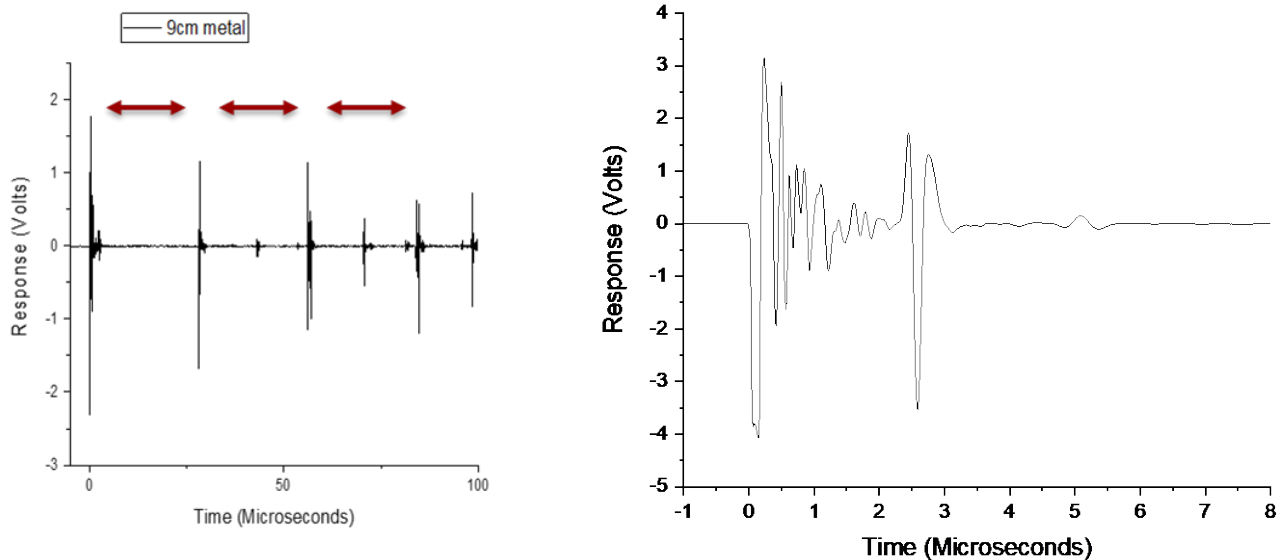


**Figure 23: Acoustic analysis of metallic sample (9 cm thick) showing repeated reflections.**  
 [image courtesy of Imad Ouchan, University of Bristol].

However, testing viscoelastic polymers can prove somewhat more difficult. The behaviour is more complex and the thickness of the sample has an influence on the behaviour observed. In thicker samples, the sound must travel further and loses its intensity due to attenuation caused by the viscoelasticity of the polymer. For thinner samples the acoustic signals overlap with other peaks such as initial cross-talk which is present due to surface mismatches that can mask reflections.

Ultrasonic non-destructive analysis has been proposed for the inspection of protective coating materials (Malikov *et al.*, 2021). In order to overcome the problems described above (*i.e.* the small amplitude of the second echo from the back wall of the coating layer), Malikov *et al.* proposed an advanced ultrasonic signal analysis in which an ultrasonic delay line was applied due to the high attenuation of the coating layer. A short-time Fourier transform (STFT) of the waveform was implemented to measure the thickness and state of bonding of coating materials (a convolutional neural network was applied to automatically determine the bonding state of the coatings).

#### 4.5.1 Ultrasonic Measurement of Speed of Sound of Thin Coating LEP Materials

Ultrasonic testing was undertaken (Domenech *et al.*, 2020) using a pulse echo mode (ISO 16810 ‘Ultrasonic testing — General principles’), and ISO 16811 ‘Non-destructive testing — Ultrasonic testing’). This technique is based on analysing the propagation of ultrasonic wave through the tested material. At each interface of the material, there is a spike in the ultrasonic response. This allows for the measuring the speed of sound through the material by finding the distance between the front-wall echo (spike response of the front face) and the back-wall echo and matching this to the material’s actual physical measured thickness, see Figure 24. Ultrasonic scanning was employed to determine the acoustic impedance of neat LEP coating and filler materials. This allowed for the measurement of material impedance at varying probe frequencies, providing information on viscoelastic response of the selected materials that are considered in the LEP configuration for this range of frequencies. Figure 25 shows the average speed of sound measurements for a 5 MHz probe.

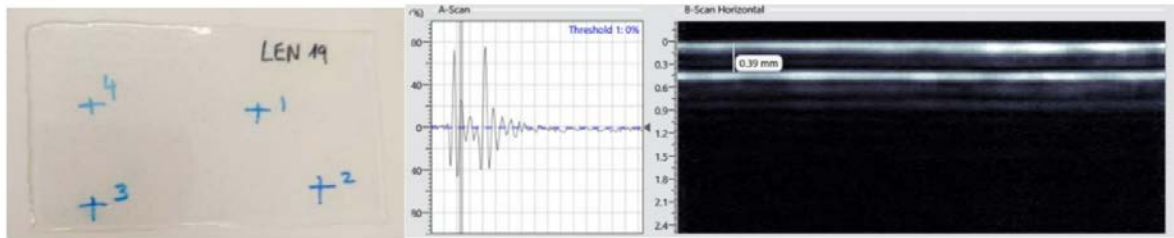


Figure 24: (Left) Thin Coating LEP used for UT coupon, (Right) Example of how a Time of Flight measurement is used in a tested coupon. Image from (Domenech et al., 2020)

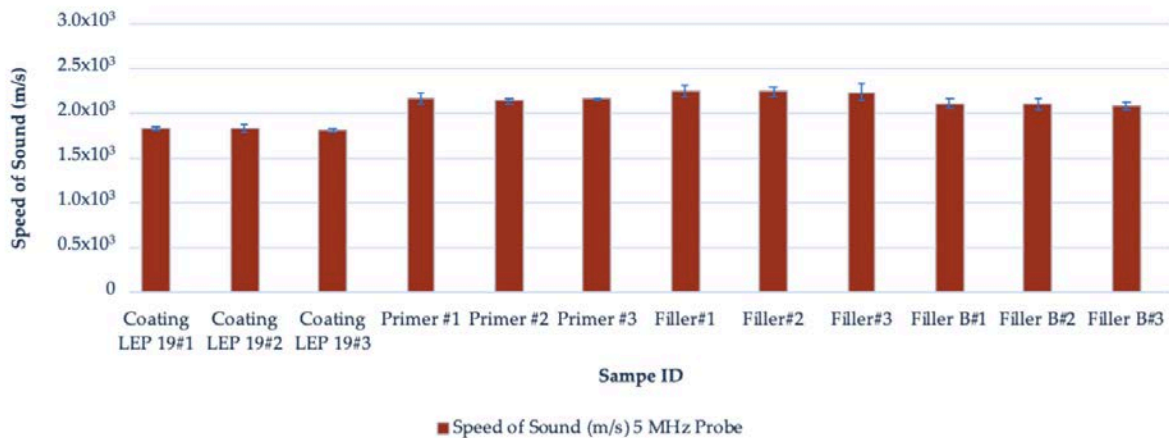


Figure 25: Average Speed of Sound measurements with the 5 MHz probe

## 5 Fracture mechanics of Layered structures

William Finnegan, Jakob Ilsted Bech, Ioannis Katsivalis, Trevor Young, Fernando Sánchez López

*Fatigue cracks and delamination of layered structures are common failure modes observed in leading edge erosion (Cortés et al., 2017)*

### 5.1 Introduction

The classical coating on a wind turbine blade is a gelcoat or top coat with a binder of thermosetting polyester or polyurethane and inorganic filler particles. It has a glass transition temperature ( $T_g$ ) above field operation temperature, so the polymer is in its glassy state (high storage modulus and low damping). This means, that impact imposes relatively high stresses – associated with high loading of molecular bonds - and low absolute strains. Recent development have led to so-called Leading Edge Protection (LEP) coatings, which are based on polyurethane binders. LEP coatings typically have  $T_g$  below the operational temperature. This means, that they appear soft with a viscoelastic behaviour. Impact on these polymers is associated with lower stresses and higher strains. Other leading edge protection solutions are tapes and pre-cast elastomer shields that are bonded onto the leading edges of blades. These are also typically viscoelastic at ambient temperatures.

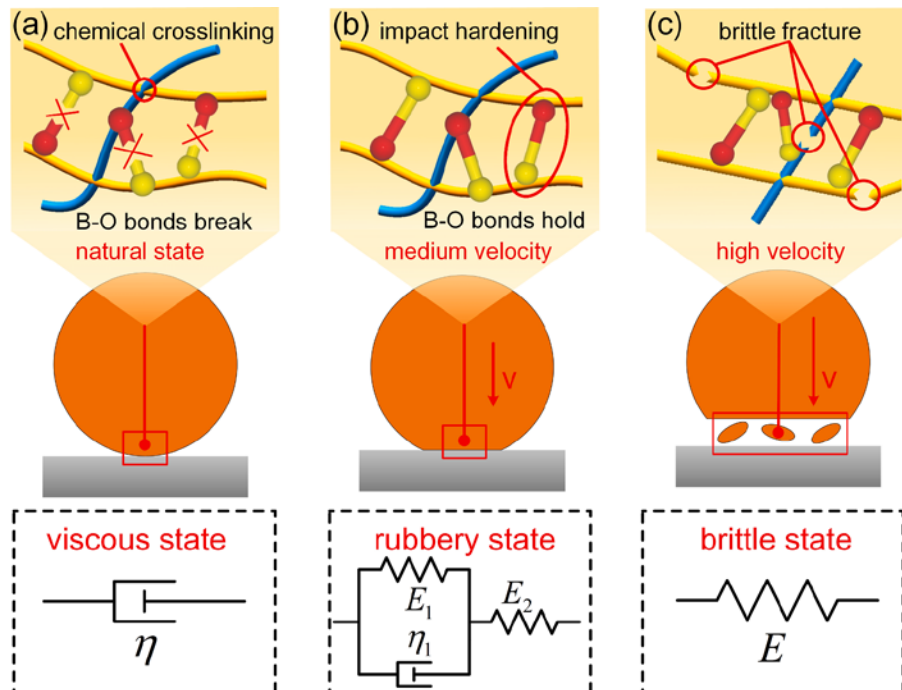


Figure 26: From Example on how different parts of structure may be loaded at different strain rates (Zhao et al., 2021)

When exploring fractures in the materials used for LEP systems, the following tests have shown to be useful:

- Tensile test
- X-cut adhesion test
- Tensile pull-off test
- Strain rate dependent interface testing
- Double cantilever beam (DCB) test
- Tension-tension fatigue test
- Single impact test

This chapter will discuss the tensile pull-off test, along with a discussion on damage and fracture of filled elastomers, including cracking during tensile testing, and the fracture tests for adhesion between polymers and a metal/composite substrate, including the DCB test. Many of the other tests have already been discussed in other chapters of this report.

## 5.2 Tensile pull-off test

The tensile pull-off method for adhesion testing involves gluing a test dolly to the coated surface and then pulling the dolly by exerting a force perpendicular to the surface to remove the dolly with the coating from the substrate. The force at which this occurs, and the type of failure obtained is recorded as a measure of the adhesion properties of the coating. Usually, international Standard ISO 4624:2016 is used for determining the adhesion of the sample on a single coating or a multi-coat system of paint, varnish or related product. These test methods have been found useful in comparing the adhesion behaviour of different coatings. The test may be applied using a wide range of substrates. For LEP systems, the typical target value is  $\geq 5$  MPa, on average and independent measures.

The major components of a pull-off adhesion tester are a pressure source, a pressure gage and an actuator. During operation, the flat face of a pull stub (dolly) is adhered to the coating to be evaluated. After allowing for the bonding adhesive to cure, a coupling connector from the actuator is attached to the dolly. By activating the pressure source, pressure is slowly increased to the actuator within the system. When the pressure in the actuator becomes larger than the bond strength between the coating and the substrate, separation occurs and the actuator-dolly assembly lifts the coating from the substrate, where a cross-sectional view of the actuator is shown in Figure 27 (left). The maximum pressure indicator of the system's pressure gauge provides a direct reading of the pressure at which the pull-off occurred. The various failure modes that can be expected during the pull-out test are illustrated in Figure 27 (right).

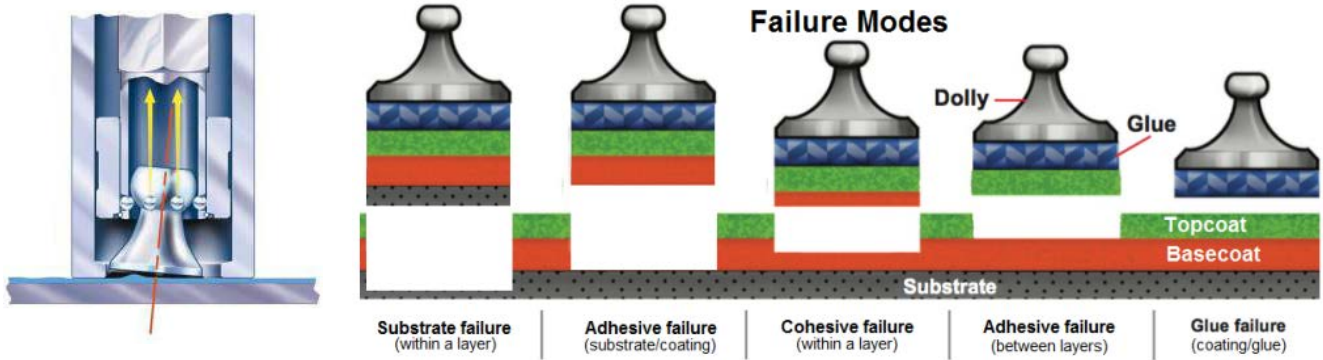


**Figure 27: Illustration of the pull-off test Actuator Cross-Sectional View (left) and the various failure modes that can be expected (right)**

Two examples of failures are shown in Figure 28, showing failure in the substrate and failure in the coating.

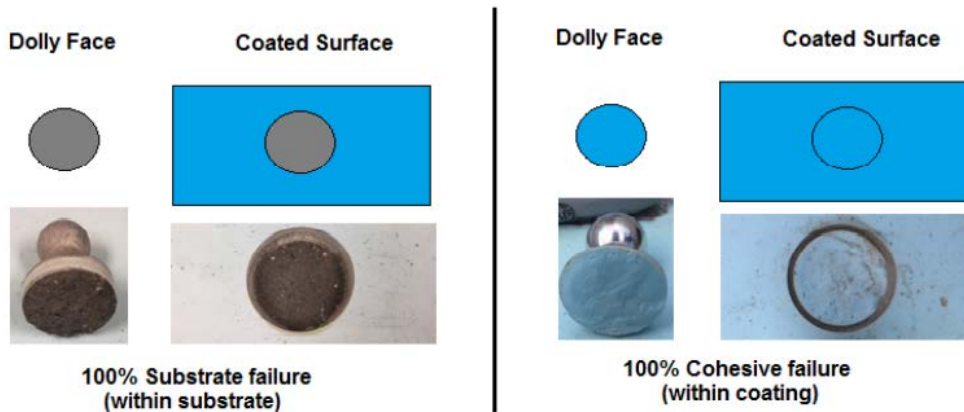


**Figure 28: Examples of failure during the pull-out test, showing substrate failure at 10 MPa (left) and cohesive failure (within coating) at 6 MPa (right)**

The typical mechanical testing used in the wind turbine industry for material qualification is developed in (Cortés *et al.*, 2017) order to assess the macroscopic behaviour of the laminates and how it is influenced by the coating-laminate interface strength. In Figure 29, pull-off strength testing of the samples shows different cases in which the failure is in the composite laminate, and hence the ability of the coating to assure the required target strength. No information regarding the interphase strength is given in cases where the failure does not take place in the coating or in the interphase, but it does indicate a limit value. Figure 30 shows a specially developed peeling test for interphase coating–laminate adhesion response quantification. The samples are moulded over a rigid substrate, where the coating is bonded with a special adhesive and hence the differences on the adhesion laminate-coating depending on its curing can be measured. Figure 31 specifies the failure load for peeling interphase adhesion testing. Coat 1 (Cured) has an average value 19.3 N and Coat 2 (Semi-cured,) of 25.1. The ISO 28501-1 ‘Adhesives - Peel Test for A Flexible-Bonded-To-Rigid Test Specimen Assembly - Part 1’ describes a 90-degree peel test for determining the peel resistance of a bonded assembly of two adherents where at least one adhered is flexible. If a normal tensile testing machine

is used, the peel angle will not be constant at exactly 90 degrees. If a constant angle of 90 degrees is required, a roller peeling device is used. It is suitable to be used with less flexible adherents for which a 180 degrees peel test is not suitable because the adherents crack, break or delaminate. Adhesives testing techniques are used in (Kinloch *et al.*, 2012) to characterize the interface fracture energy of polymers in a similar procedure.

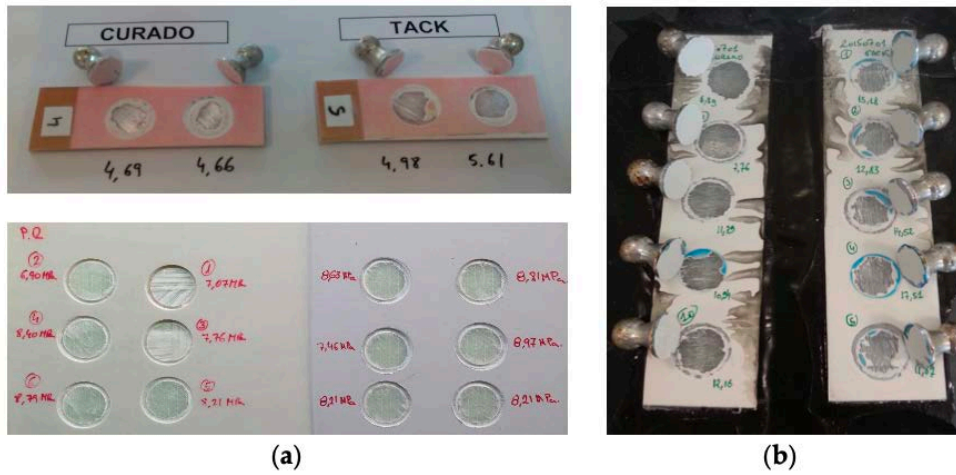


Figure 29: (a) Pull-off strength testing of composite laminates used for coating adhesion. Images of the failure in the laminate (b)

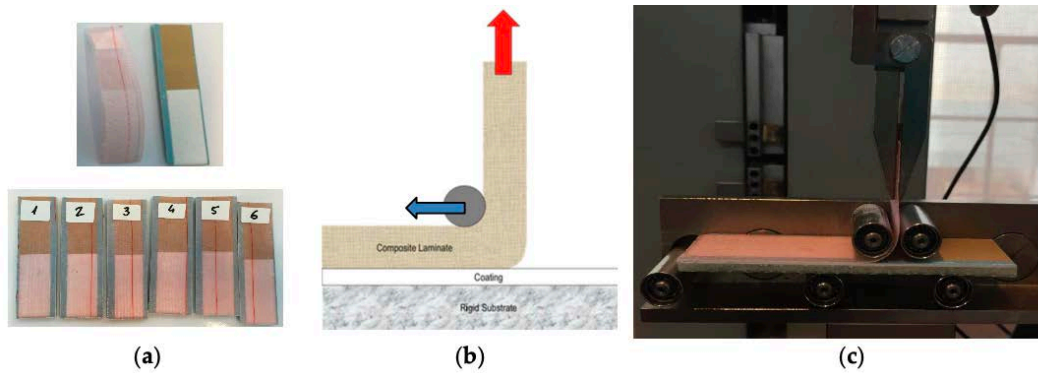
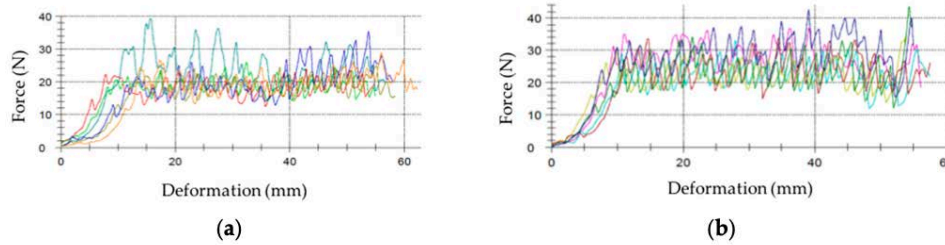


Figure 30: Developed peeling testing for interphase coating-laminate adhesion response quantification. (a) Developed specimens; (b) forces on testing; and (c) peeling testing system



**Figure 31: (a) Force of failure for interphase adhesion testing: Coat 1 (Cured), average value of 19.3 N (averaged across six samples, plotted in different colours) and (b) Coat 2 (Semi-cured), average value of 25.1 N (averaged across six samples, plotted in different colours)**

In the same work, it is shown in Figure 32 the pull-off testing of the samples in a LEP system with different configuration comparing the adhesive failure for the no-primer configuration (with a value of 5.6 MPa) and the cohesive failure (6.77 MPa) of the specimens that include the primer layer (b). The LEP in the no-primer coupon has been cleanly pulled off, whereas the primer coupon has not come off as easily. Figure 33 demonstrates the improved interphase coating–laminate adhesion response when the primer layer is included, with a force load for peeling with a value of 29.3 N (averaged across five samples), versus a value of 9.45 N for the no-primer configuration. It is clear that the primer significantly improves the adhesion of the LEP to the filler. The inclusion of the primer layer increases the fracture energy revealed by the peeling testing values.



**Figure 32: Pull-off strength testing of specimen laminates used for LEP coating adhesion: (a) adhesive failure with no-primer intermediate layer application; (b) cohesive failure with primer application (the dolly adhesive effect can also be observed)**

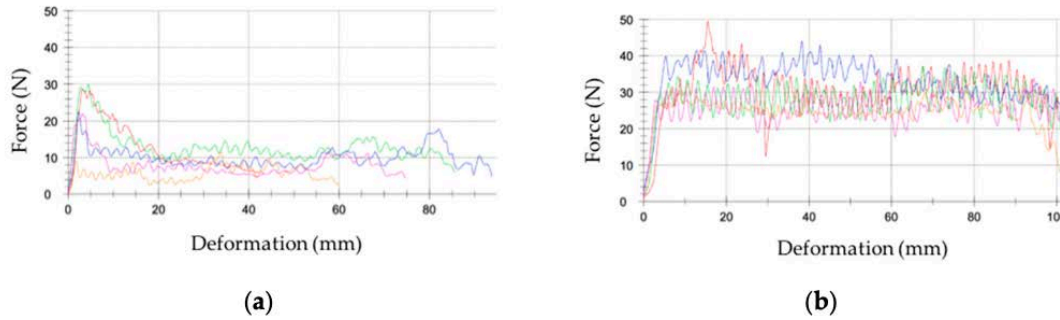


**Figure 33: (a) Force of failure for interphase adhesion testing: LEP coating configuration with no-primer application, average value of 9.45 N and (b) LEP coating configuration with intermediate primer layer, average value of 29.31 N**

### 5.3 Damage and fracture of filled elastomers

The fracture of polymers and filled polymers may act on different scales. For neat polymers there are three main mechanisms of fracture: breaking of hydrogen bonds, breaking of crosslinks and scissoring of molecular chains. For filled polymers and elastomers like coatings with particular fillers de-bonding of particle-binder interface may be a fourth mechanism. Furthermore the filler particles may create stress concentrations leading to crack initiation in the polymer. Stress concentrations at embedded particles depend on their size and shape and mechanical and physical properties.

#### 5.3.1 Fracture mechanisms

Fan et al. (Fan, Weerheijm and Sluys, 2015) studied high strain rate fracture of a clear elastomeric polyurethane with a glass transition temperature of 2°C at low strain rate. They identify a glass transition strain rate at room temperature of 450 s<sup>-1</sup>. They also show, how fracture in the PU initiates as nano-size ridges and crazes and develop into cracks, see Figure 34.

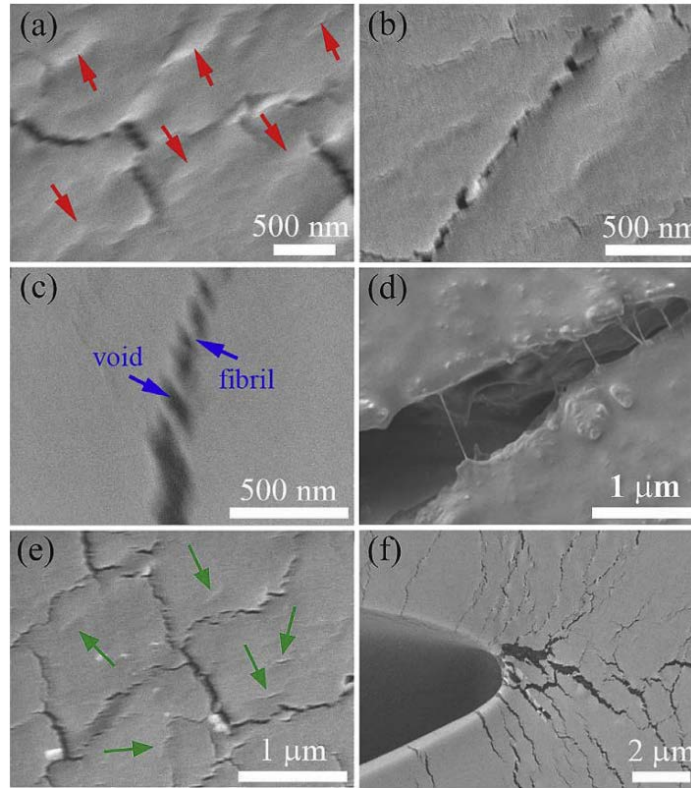


**Figure 34: Crazing process of craze formation and development into micro crack as well as the toughening effect: (a) the nano-size ridges to indicate the nucleus of craze; (b) the coalescence of ridges to form the embryo of craze; (c) a mature craze consisting of fibrils and voids; (d) the development of craze into crack; (e) the interaction of crazes and the nucleus of new crazes; (f) numerous micro crazes and micro cracks ahead of a blunted crack revealing a toughening effect. From (Fan, Weerheijm and Sluys, 2015)**

(Mishnaevsky *et al.*, 2020) observed de-bonding between binder and large filler particles in a coating after rain erosion test. Images with high magnification of damage in this coating system are shown in Figure 35.

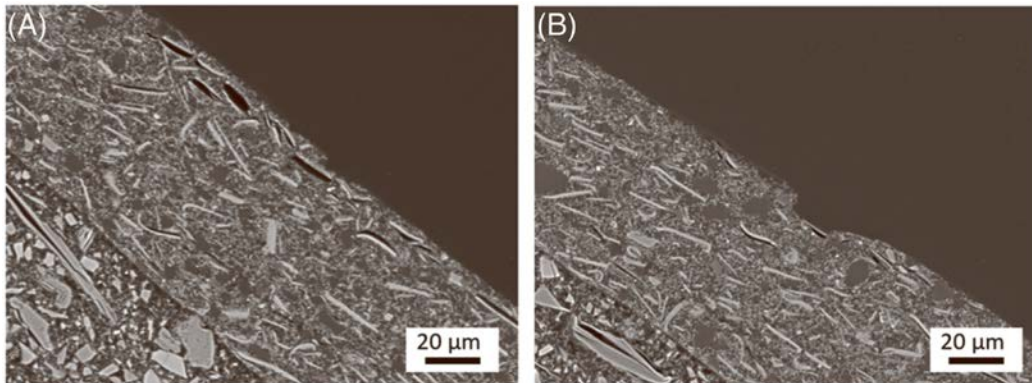


**Figure 35: Scanning electron microscopy (SEM) images with high magnification (1000×) of coating system A. A, Cracks close to the surface are seen to be closely connected with white elongated particles. B, Surface spalling are observed above white elongated particles. (Mishnaevsky *et al.*, 2020)**

### 5.3.2 High strain rate fracture

High speed Crack resistance curves can be obtained with engineered impact tensile test and high speed camera (Reincke, Grellmann and Heinrich, 2006). For natural rubber with filler of layered silicate, the tearing energy  $J_d$  depends on filler contents.

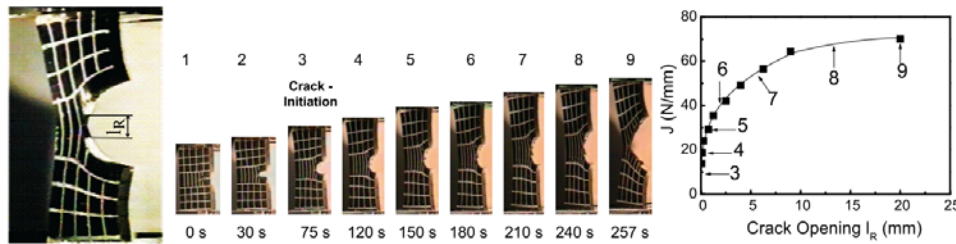


Figure 36: Principle of recording a crack resistance curve with a single spectrum (Reincke et al.)

Mason (Mason, 1958) Studied the fracture surfaces and crack propagation velocities for natural and synthetic rubber, which is shown in Figure 37. They observed that the crack propagation velocity varies over time, and brittle fracture relates with high speed and smooth fracture surfaces.

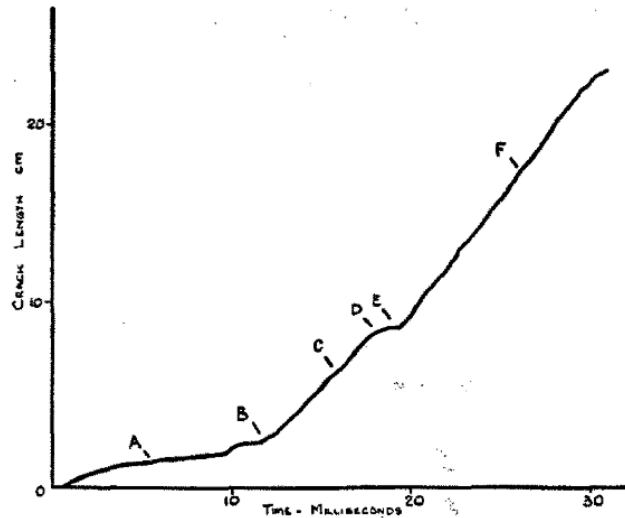
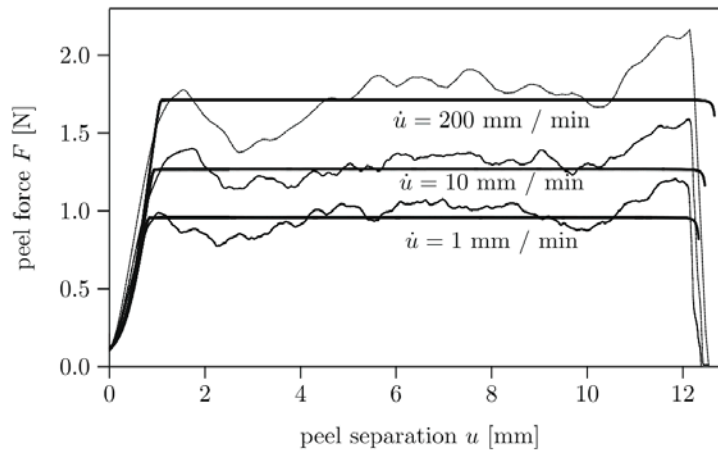


Figure 37: Crack propagation in synthetic rubber. Crack length [cm] as a function of time [milliseconds] (Mason, 1958)

In regards adhesion tests (treated previously in this document), and considering strain rate dependency on interface due viscoelastic behaviour, a compact representation of the fracture mechanical basis, kinematic and constitutive issues are given in the first part of the work of (Geißler and Kaliske, 2010). It analysed developments of cohesive finite element methods for time-dependent fracture so is able to consider rate-dependent separation effects during the crack opening process. On the basis of a rheological model assumption, a novel viscoelastic extension for cohesive traction separation laws was presented and the resultant characteristic behaviour compared for different

loading conditions. It is interesting for adopting an industrial application of a peel foil specimen, the time- dependent characteristics as well as some aspects of parameter identification.



**Figure 38: Experimental and numerical peel curves for variation of the peel test speed. (from (Geißler and Kaliske, 2010))**

### 5.3.3 Fatigue crack propagation in elastomers

Eberlein et al. (Eberlein, Fukada and Pasięka, 2021) studied cyclic fatigue crack growth in a PU elastomer using a plane strain tensile test with a crack. Figure 39 shows the schematic test setup.

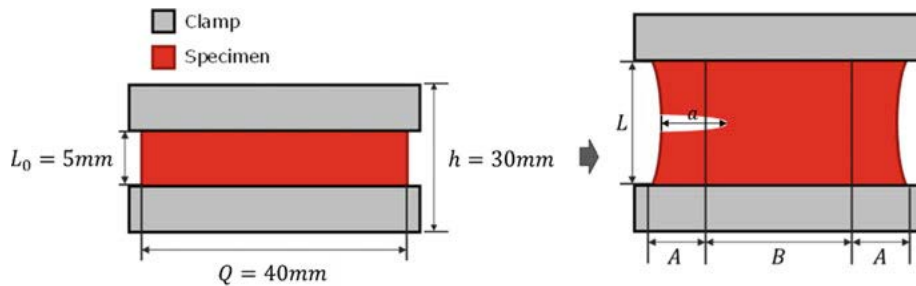


**Figure 39: Plane strain tensile test with a crack. From (Eberlein, Fukada and Pasięka, 2021)**

The tensile test, which is described in Section 4.2, can be used to determine and compare mechanical properties of LEPs. It is possible to determine the mechanical behaviour at different temperatures. In the wind energy sector, testing ranges between - 30 °C and 50 °C (DNVGL-RP-0573). The area under the tensile curve to fracture, produced during tensile testing, is called the toughness modulus.

## 5.4 Fracture tests for adhesion between polymers and a metal/composite substrate

Evaluating the adhesion between a polymer and a metal/composite substrate often requires fracture tests with the ability to measure the interfacial fracture toughness. It is worth noting that to account

for complex loading scenarios, the fracture toughness typically needs to be evaluated at both the opening (mode I) and the shearing (modes II and III) modes.

Normally, the determination of these properties in mode I is achieved using the Double Cantilever Beam (DCB) test (Figure 40 a) (Fernandes and Campilho, 2017). ASTM D3433-9 (Standard, 2012) describes the DCB test for similar metal substrates, and the method has been used extensively. There are also several variations for the DCB specimen such as the asymmetrical DCB (Katsivalis *et al.*, 2020) and the tapered DCB specimens (Figure 40 b) (Ranade *et al.*, 2014).

Similarly, for the determination of the interfacial fracture properties in the shearing modes, the End Notched Flexure (ENF) test is most commonly used (Figure 40 d) (de Moura, 2006)(Borg, Nilsson and Simonsson, 2004)(da Silva, Öchsner and Adams, 2011). ENF generally generates significant stresses in both substrates and when high stresses need to be avoided, mixed mode tests can be used as an alternative. The Single Leg Bending (SLB) test (Hong and Yoon, 1990), for example, is a simple modification of the ENF test which introduces mode-mixity (Lee *et al.*, 2010), but also significantly reduces the stresses in the substrates. The Mixed Mode Bending (MMB) specimen (Figure 40 c) is also a quite common testing method where the mode mixity ratio can be adjusted (Chen *et al.*, 1999). It is worth noting that the last few years more tests have been developed/proposed for the measurement of the interfacial fracture toughness under shear loading such as the End Loaded Split (ELS) specimen (Figure 40 e) which was also recently standardised by ISO 15114 'Fibre-reinforced plastic composites' and the 4-point ENF specimen (Figure 40 f).

These tests are designed for adhesive materials which are typically sandwiched between two stiffer substrates and therefore might be less relevant for the interfacial fracture toughness evaluation of the coatings typically used in wind turbine blades. However, they can provide ideas and be used together with the coating tests that were described in this section. It is also worth noting that many of these tests have been used in fatigue (Jiang *et al.*, 2021) and also in high-strain rate (Cho *et al.*, 2012) applications (but lower compared to the strain rates of interest for rain erosion related research).

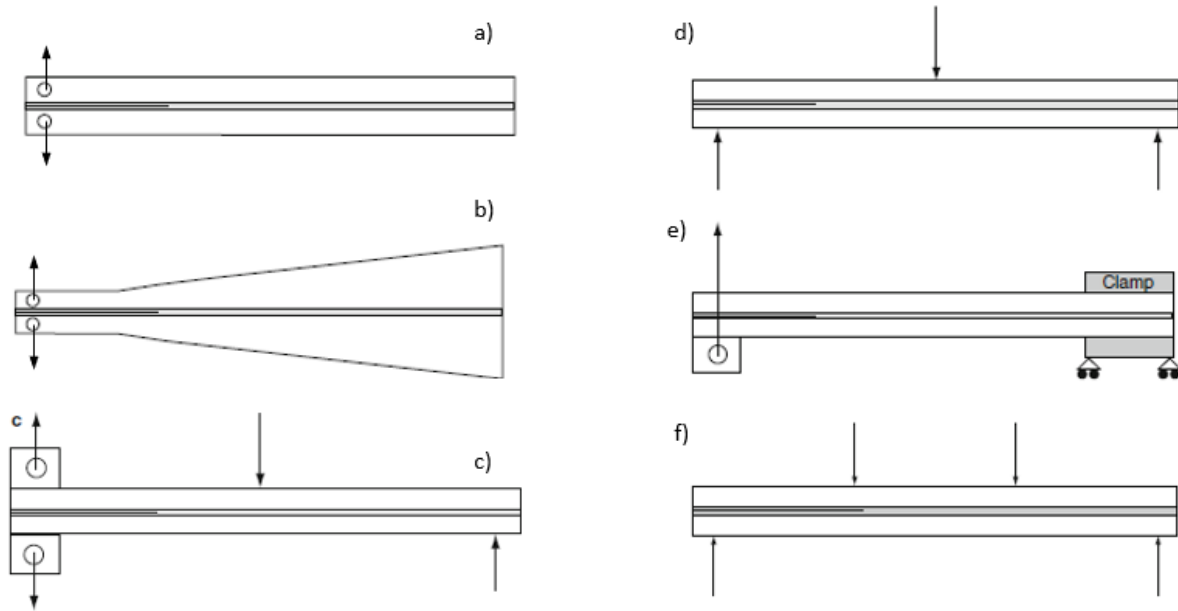


**Figure 40: Common fracture specimens used to determine the fracture toughness of bonded interfaces: a) DCB, b) TDCB, c) MMB, d) ENF, e) ELS, f) 4-point ENF specimens. Figure adopted from da Silva, Öchsner (da Silva, Öchsner and Adams, 2011)**

## 5.5 Reflections on fracture mechanics of layered structures

The current LEP systems being used are based on polyurethane binders, meaning that they are soft with a viscoelastic behaviour. The impact during operation, due to rain and particles, on the LEP systems are associated with lower stresses and higher strains. However, this is difficult to replicate in laboratory conditions using traditional tensile testing. Furthermore, the conditions experienced by the material during this test are not representative to what would be seen in operation as high elastic strains would be prevented by the wind blade substrate that it is adhered to. Therefore, the research has focused on the interfaces between the layers that make up the LEP systems. The tensile pull-off test and the DCB test, along with discussion on damage and fracture of filled elastomers and the fracture tests for adhesion between polymers and a composite substrate, have been presented. Further adaptations of these tests could be investigated to improve adhesion of LEP systems to the wind blade substrate, along with incorporating impact testing for initial trials of materials for the next generation of LEP systems.

## 6 Microstructure and non-destructive analysis

*Julie Teuwen, Ian Hamerton, Jakob Ilsted Bech, Nicolas Quievy, Ole Bang, Christian Rosenberg Petersen, Søren Fæster, William Finnegan*

*Characterizing the microstructure is important for understanding leading edge erosion (Cortés et al., 2017), (Mishnaevsky et al., 2020), (Fæster et al., 2021)*

*The surface morphology and roughness can also influence the stresses from drop impact (Kirols et al., 2015), (Fujisawa et al., 2018), (O'Carroll et al., 2018)*

### 6.1 Microstructure characterisation (surface)

In the following sections we will be considering different methods for microstructure characterisation relevant to erosion testing with the main goal to present the methods relevant to identify the failure modes and damage progression due to erosion as well as quantify the effects of erosion. Herein we will consider two sub categories: surface characterization and non-destructive testing methods through thickness.

Typically, the erosion process begins with non-visible damage beneath the surface, then barely visible damage on the surface where surface roughness is expected to increase, but the mass loss is not measurable yet (incubation period). After the incubation period, the surface material starts to yield, roughness is increased due to the continuous droplet impacts and lateral jetting strips out imperfections, forming pits and leading to mass loss (O'Carroll, 2018).

#### 6.1.1 Microscopy

Studies have shown that roughness is a good parameter to assess rain erosion (O'Carroll, 2018). Due to stress waves, the lateral jetting can cause imperfections present in the surface to be stripped away caused by stress waves, increasing surface roughness and eventually, leading to mass loss of the coating. Several studies (Fujisawa *et al.*, 2018)(Bowden and Brunton, 1961)(Heymann, 1967)(Kirols *et al.*, 2015)(Field, 1991) have demonstrated that the initial surface roughness can strongly influence the incubation period.

Surface roughness can be measured through microscopy (Roughness Measurement as per ISO 21920:2021). Optical profilometers such as ContourX-100 Optical Profilometer and Keyence VX5000 can give 2D/3D high-resolution measurements in short times, have stitching capabilities to create high resolution measurements over large areas. It can be used to measure profile, roughness, flatness, wear volume, or comparing 3D scan data to reference surfaces. The working principle of the profimeter is emitting structured light through several double-telecentric lenses to reduce distortion. Distortions in the light bands caused by height differences are converted to height using triangulation.

Several analyses can be run from the profilometers data that are useful for erosion: surface roughness, surface texture, volume loss (which can be related back to the typical mass loss), coating thickness variations, damage area, damage locations, depth, width and height of damage, damage radii and

nature of the damage: such as cracks, pitting or loss of adhesion between substrate and coatings through 3D imaging and measurement system able to investigate the height-map of the damaged area, roughness changes over an entire area. In Figure 41, an example of the height map of a damaged area is shown. It is a robust techniques and can also be used to monitor wet coatings, but it is only a surface technique to measure topography, so it can only measure relative decrease in wet film thickness as the coating is cured. Overall, the main drawback is that no subsurface information can be obtained with this technique.

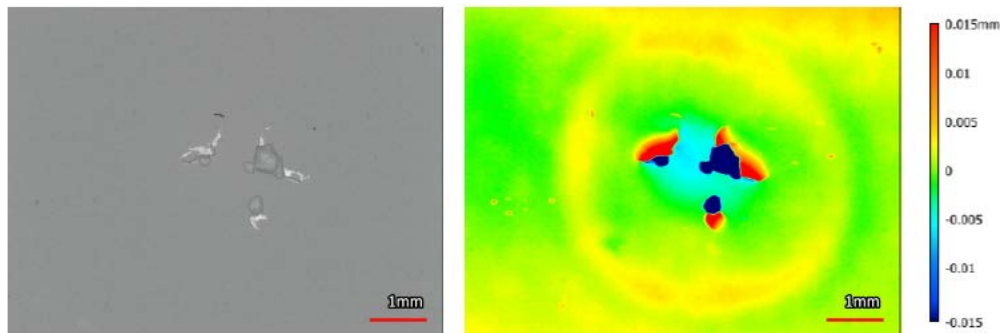


**Figure 41: Microscopy analysis of damage sample both through light microscopy (left) and height maps (right) [courtesy: Miguel Alonso, TUDelft]**

Other than profilometers, confocal laser microscopes (Tobin *et al.*, 2015), portable surface roughness tester such as Hommel Tester T1000, or contact type roughness meter (Fujisawa *et al.*, 2018), and AFM (see section 6.1.2) can be used to assess the changes in surface roughness due to erosion.

Several roughness parameters can be analysed that change during the incubation period of samples subjected to erosion:

- Height parameters
  - Sa: Arithmetic mean height
  - Sq: Root mean squared height
  - Sp: Maximum peak
  - Sv: Maximum valley
  - Sz: Maximum height
  - Ssk: Skewness
  - Sku: Kustosis
- Feature parameters:
  - Spc: Arithmetic mean peak curvature
  - Spd: Density of peaks
- Hybrid parameters

- Sdq: Root mean square gradient (surface slope)
- Sdr: Developed interfacial area ratio
- Functional parameters (material ratio):
  - Sk: Core height
  - Smr: Peak material portion
  - Smr2: Valley material portion
  - Spk: Reduced peak height
  - Svk: Reduced valley depth

It is important for the community to identify what surface roughness is as it is not a single parameter, assess the most important roughness parameters and which parameters are important from a structural degradation point of view and which parameters are more relevant for aerodynamic simulations. Typically arithmetic mean height is used to determine the surface roughness. Tobin et al. (Tobin *et al.*, 2015) measured the surface topography through analysis of arithmetic mean surface profile (PSa), and the average primary profile peak-to-valley (PSz) was identified as the second significant topographical measurement. The use of these surface topographical measurements can also be used for the comparison of test results. They concluded that to provide relevant data and topographical measurements, averaging of the surface (either large areas or several measurements over different areas) is necessary.

### 6.1.2 AFM

AFM is high-resolution scanning probe microscopy (SPM) - resolution in the order of fractions of a nanometer (nm). AFM creates images by scanning a small cantilever over the surface of a sample, which can characterise the electrical, magnetic, mechanical, and morphological properties of materials, such as surface roughness and elastic modulus. AFM typically has an integrated inverted optical microscope. For erosion research, AFM is used for the characterization of morphology of structure and surface roughness of the structure (Dashtkar *et al.*, 2019).

Zhang et al. (Z. Zhang *et al.*, 2021) used AFM to study the surface topology variations as a function of the duration of the rain erosion testing experiments. They used the AFM in tapping model, and used the drive voltage, the piezo displacement data and cantilever deflection of the AFM probe to analyse the results. An AFM probe with a nominal conical radius of 20 nm and an opening angle of 20 degree was used for the topology imaging of the coated surface. It is important to calibrate the radius of the AFM probe prior to the characterization of materials. A typical AFM picture is given in Figure 42. AFM can be used qualitatively (observing changes in the topography) and quantitatively. When characterizing the surface topology, the average surface roughness (Ra) and the root-mean-square (Rq) values can be obtained and used to quantify the changes of the surface topology characteristics of the tested surfaces. Due to the high resolution, nano- and micro-scale texture and roughness with

different sizes and heights (hierarchical structures) can be observed. The observations are however limited to small sizes in the samples.

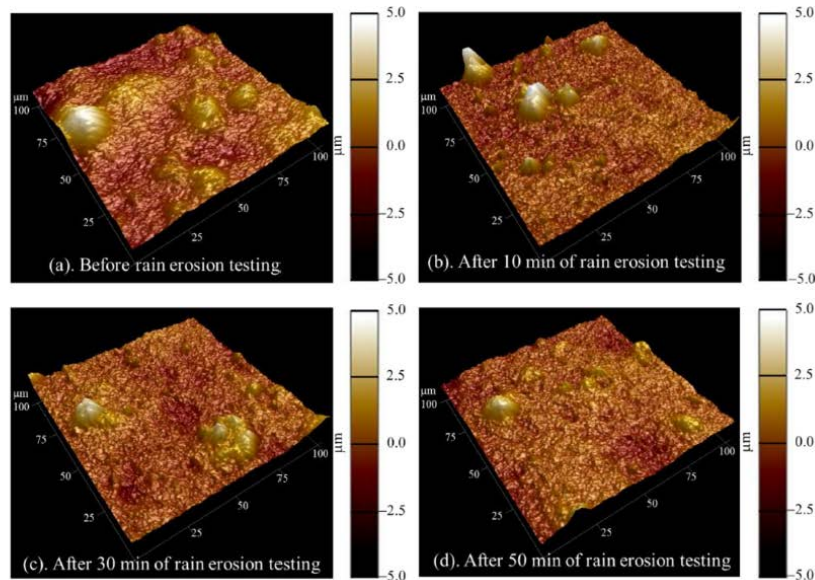


**Figure 42: Typical AFM images showing the changes in surface topology of coated samples due to droplet impact [Source: (Z. Zhang *et al.*, 2021)]**

### 6.1.3 Spectroscopy

The application of spectral characterisation to determine character of the materials, and how it might be used to determine how they change, is included here for completeness. Fourier transform infrared (FTIR) and Raman spectroscopy are complementary forms of vibrational spectroscopy and very common non-destructive analytical techniques. The underlying principle of FTIR spectroscopy involves the detection of the absorption of light by a compound, in the IR region (i.e. the mid infrared  $4000 - 600 \text{ cm}^{-1}$ ) of the electromagnetic spectrum. In order to absorb light the molecule must couple with the incoming radiation and this happens most strongly with bonds within the structure that can exhibit a ‘dipole moment’ where electrons within a bond are not shared equally (*e.g.* O-H, C=O, C-O, C-N, *etc.*). Raman is a complementary method as it relies on the inelastic scattering of photons (Raman scattering) when the sample is irradiated with laser radiation. Whereas FTIR relies on the presence of strong dipoles, Raman spectroscopy is most sensitive to the presence of polarisable bonds (*e.g.* C=C), but it is relatively inefficient and requires high powered lasers, or longer analysis times (and is more affected by fluorescence), which can swamp the signals from the sample. Both techniques are particularly useful for identifying the presence (or confirming the absence) of functional groups. Thus, FTIR may be used to determine the degree of cure exhibited by an amine-cured epoxy resin in a composite matrix, or confirm the degree of crystallinity or tacticity in an acrylic polymer.

### 6.1.4 Chemical structure

The techniques used to determine chemical structures, are included here for completeness, but reader is directed to Chapter 7, where these techniques are applied to monitor the extent of material degradation during use and are discussed in more depth.

## 6.2 Gloss

The glossiness of a surface is correlated to the surface roughness. Whether a surface has a shiny or matte appearance is called gloss (Marrion, 2004), which is due to the reflection of incident light. First of all, gloss is measured when coating is applied to the blades and is assessed on two critical factors: the particle size of the fillers and pigments in the coating material and b) the ratio between the polymer and the solid fillers/pigments. Typically, the higher the binder content, the glossier the coating (Arabatzis *et al.*, 2019). Secondly, the changes in glossiness of the surface can be used to measure surface changes after erosion testing (Leishman *et al.*, 2022).

A gloss meter can be used to measure specular reflection gloss of a surface. Gloss is determined by projecting a beam of light at a fixed intensity and angle onto a surface and measuring the amount of reflected light at an equal but opposite angle. In the gloss meter the incident light beam can be set to a certain angle. The test standard for glossiness is defined in ISO 2813:2014.

### 6.2.1 Visual inspection

Surface damage can be analysed with visual inspection or surface photography, especially useful for larger damages. The analysis however will only be 2D and can include surface damage area identification.

## 6.3 Microstructure characterisation (through thickness)

### 6.3.1 Cross-sectional microscopy

The coating structure, thickness and the interfaces between coating and substrates can be analysed through cross-sectional microscopy. The coated panels need to be cut, potted in a reactive epoxy resin (under vacuum to prevent bubble formation), then sanded, and polished to have a smooth cross-sectional surface for imaging. Samples are typically sanded in a series of steps using 120, 320, 600, 800, and 1200 grit silicon carbide sandpapers and polished with a slurry of 0.05  $\mu\text{m}$  particle size Gamma Alumina to expose a smooth cross-sectional surface of the coating system (Wen and Dušek, 2017). It can be used for quick measurements of the thickness of substrate and coating, void distribution over the coating, substrate or interfaces but care needs to be taken in the representativeness of the section analysed compared to the entire panel. The information from the microscopes (see section 6.1.1) is only a 2D image, especially for voids the shape of the voids can't be captured by the cross-sectional microscopy, nor can the results be extrapolated to 3D information.

### 6.3.2 X-ray computed tomography

X-ray computed tomography (CT) is a non-destructive technique that generates a 3D density map of the investigated specimen. A series of projection images are obtained by rotating the specimen and acquiring a projection image at each angular position. Each projection image reveal the attenuation of the X-ray beam that passes through the sample from that specific angular position.

By combining the information from a series of projections from different angular positions, a three dimensional map of the attenuation within the specimen can be reconstructed. Thus the technique is ideal for investigating samples that contain particles, impurities, air bubbles, cracks, etc. which have a different density than the matrix material of the specimen.

Features with high density will appear bright in a tomographic reconstruction and low density regions will appear dark. The three dimensional nature of the reconstructed volumes allow positioning virtual cross sections through the volume in different directions. Figure 43 show two virtual cross sections through a tomographic reconstruction of a RET specimen after testing (Leon, Fæster and Rad, 2020). The glass fibre composite is located in the bottom of the figure where the individual glass fibers are observed as light grey circular cross sections. A layer of putty is located on top of the composite and are observed to contain high absorbing filler particles – white particles within the putty layer. X-ray tomography do not give any information about the chemical composition .The top coating is located on top of the putty and contain several features with the same dark contrast as the air surrounding the specimen. These features are air bubbles and cracks connecting the air bubbles to the surface. These features are air bubbles and cracks connecting the air bubbles to the surface.

The effect of air bubbles in the coating have been investigated by Fæster et al (Fæster *et al.*, 2021). Other similar studies where X-ray tomography have been used to investigate the damage mechanism in leading edge erosion can be found in (Mishnaevsky Jr *et al.*, 2020)(Hasager *et al.*, 2021). Spallation from the surface can be observed in Figure 1 as missing parts of the top surface. Nash et al have determined the missing volume by analysing tomographic reconstructions at different erosion stages (Nash *et al.*, 2021).

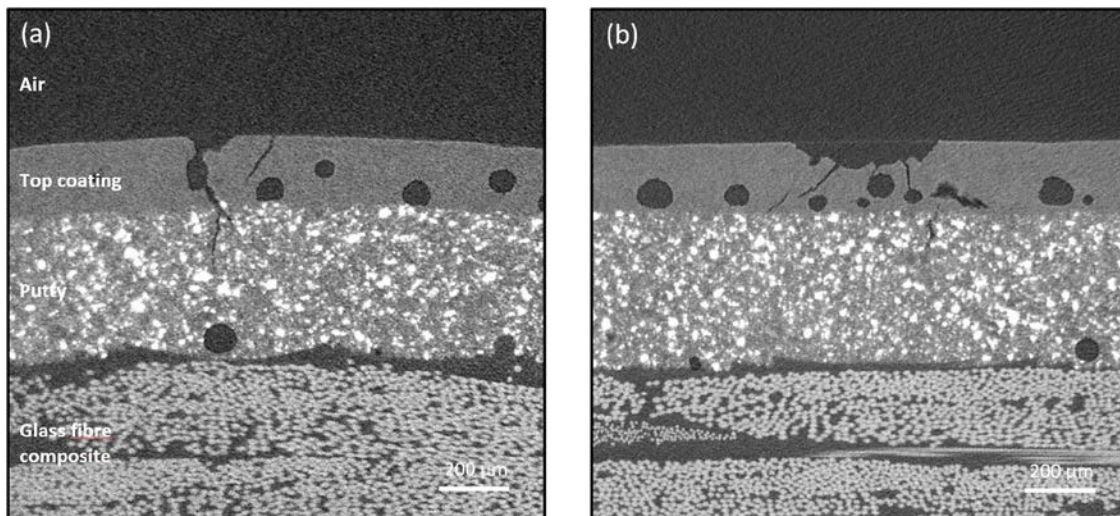


**Figure 43: Virtual slice through a tomographic reconstruction of leading edge erosion specimen after testing showing cracks between the surface and bubbles within the top coat. From (Leon, Fæster and Rad, 2020)**

X-ray tomography can be performed on laboratory equipment as well as at large facilities like synchrotrons. The X-ray source in laboratory equipment generates a conic beam of photons. Due to the cone beam a geometric magnification is obtained. Reducing the distance between source and object allows for larger magnifications and an improved spatial resolution, but it also reduces the field of view. Typical scan times are in the order of hours.

Synchrotron tomography typically employs a parallel beam geometry and offers a significant advantage by its nearly parallel beam of high brilliance and very high flux - at least 1000 times larger than laboratory X-ray sources (Requena *et al.*, 2009)(Kastner *et al.*, 2010). The spatial resolution can be increased by applying monochromatic radiation, which also allows the generation of phase contrast of internal interfaces between phases. In order to realize the advantages of synchrotron X-

ray sources the specimens typically have to be 5-10 mm, which is a limitation when investigating leading edge erosion. However synchrotron tomography allow reconstruction with very high spatial resolution, down to 40 nm (Requena *et al.*, 2009) and very fast scan times are achievable – down to the order of seconds for a full scan (Babin *et al.*, 2006).

X-ray tomography is regarded as a non-destructive technique and it is therefore possible to scan a rain erosion test sample several times during testing (Garcea, Wang and Withers, 2018), which will allow observation of how cracks propagate within the material below the surface during rain erosion.

When some polymer samples are investigated by X-ray tomography they change colour, due to an oxidation process on the surface. How deep and to what extent, this affects the materials properties needs to be investigated for a given material.

The technique can be used for 2D inspection to detect defects and 3D scanning of smaller objects inside a closed scanner with rotating sample or X-ray stage. This ensures complete penetration and imaging of the entire structure but limits the size of the samples that can be 3D scanned.

### 6.3.3 Luminescence microscopy

In contrast with black body radiation (*i.e.* thermal electromagnetic radiation) and incandescence (light emitted from heating), luminescence describes the spontaneous emission of light induced variously by chemical reaction, electrical energy, subatomic motions, or by applying stress to some crystalline materials (Valeur and Berberan-Santos, 2011). In the context of characterising surface defects, mechanoluminescence (ML) is perhaps the most pertinent example of the phenomenon, wherein light is emitted in response to mechanical stimuli such as stress, strain, friction, and fracture (Olawale *et al.*, 2011).

In particular, deformation mechanoluminescence (DML) involves light emission induced by the mechanical deformation of solids classified into elasto-mechanoluminescence (EML), plasto-mechanoluminescence, and fracto-mechanoluminescence induced by elastic deformation, plastic deformation and fracture, respectively. EML is particularly attractive due to the characteristics of linearity, reuse, durability, and non-destructive light emission for various applications including sensors, light sources, and coloured displays (Xu *et al.*, 1999)(Moon Jeong *et al.*, 2013)(Jha *et al.*, 2018).

In the present context, the use of mechano-luminescent species can be used as a sensing medium to detect the presence of cracks or stress concentrations in composite coatings. Kong *et al.* (Kong *et al.*, 2020) reported the preparation and characterisation of a polydimethylsiloxane (PDMS) composite containing a nonwoven polyetherimide (PEI) veil with ML phosphors based on micron-sized  $\text{SrAl}_2\text{O}_4:\text{Eu}^{2+}, \text{Dy}^{3+}$  (SAOED) particles. The mechanism of the SAOED emits light is shown in Figure 44. When the SAOED absorbs excitation source energies, due to stress, strain or light, SAOED is excited and pairs of holes and electrons are produced (Figure 44). Some of the free holes are captured by trap levels and electrons of  $\text{Eu}^{2+}$  are excited to the  $4f^6 5d^1$  level from the  $4f^7$  ground level. After the excitation is removed, the recombination at the metastable state of Eu occurs, with the trapped holes being released to the valence band, leading to luminescent light emission.

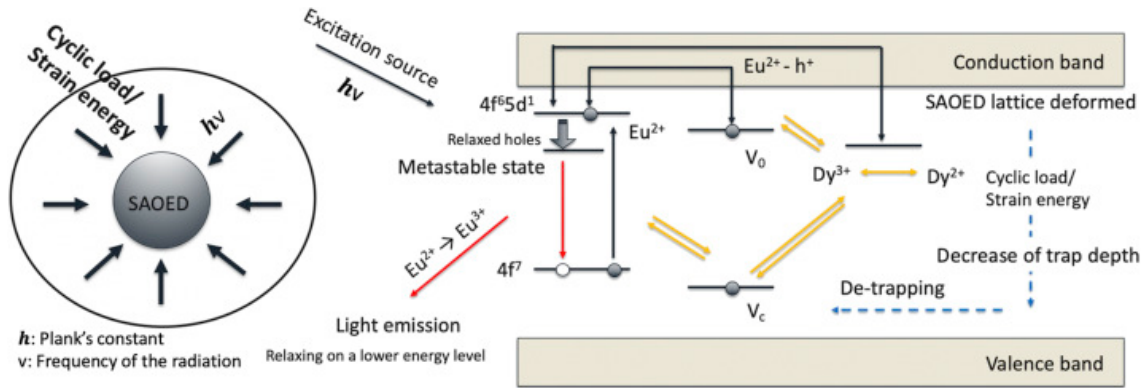


Figure 44: Mechanism of ML in SAOED ( $V_c$ : interstitial vacancy;  $V_o$ : oxygen vacancy). [Image courtesy of Dr Kyungil Kong, University of Bristol].

EML was characterised by observing the light emission under cyclic displacement testing. The composites were subjected to cyclic displacement testing (Figure 45), to mimic the loading pattern of a turbine blade. The spectral data, *i.e.* light intensity and wavelength, increased at the maximum extended deformation of the SAOED embedded in the PEI veil within the PDMS composite.

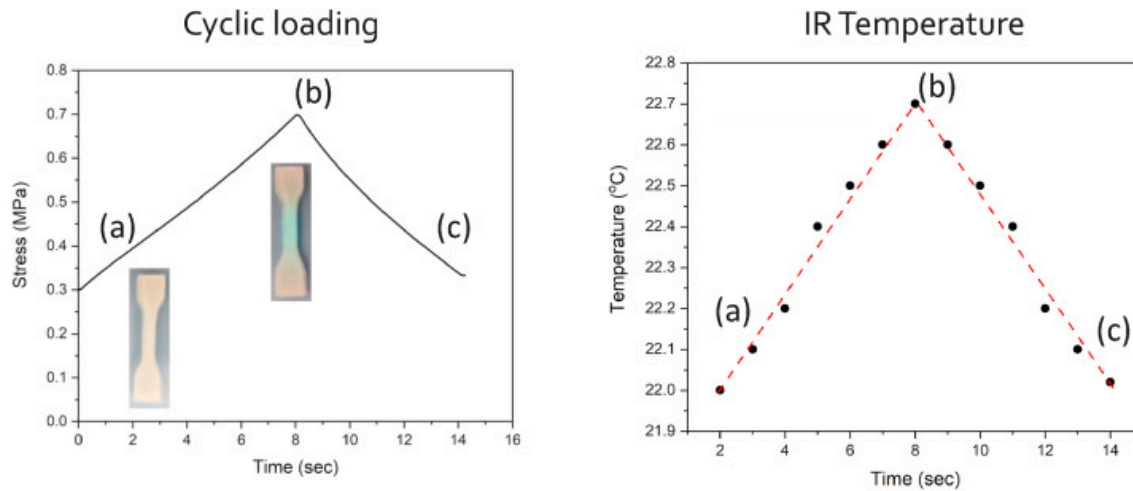


Figure 45: Cyclic loading along with measuring IR temperature; (a) initial position, (b) maximum position, (c) returning position. [image courtesy of Dr Kyungil, University of Bristol(Kong *et al.*, 2020)].

### 6.3.4 Scanning electron microscopy (SEM) and Energy Dispersive X-Ray spectroscopy (EDX)

Scanning electron microscopy (SEM) can be used to analyse cross-sectional samples (see section 6.3.1), evaluate the microstructure, surface characteristics (Goldstein *et al.*, 2017)(Reimer, 2000) as well as erosion damage and the main failure path. The technique is thus used as a surface characterisation technique as well as a cross-sectional technique. SEM is typically used at high magnifications to assess the micro/nano-structure. The principle of SEM is to use a focused beam of electrons to scan the surface of the sample, these electrons interact with the sample's atoms, producing various signals (secondary electrons, characteristics X-rays back-scattered electrons for example), caught by specific detectors and produce an image. The most common signal used is secondary electrons, which need

to be used with electrically conductive samples to avoid some artefacts and scanning faults on the picture. The solution is to coat the samples with a small layer of a conductive material, typically gold, on the surface needed to be scanned. Due to the gold sputtering, direct comparison of the samples using SEM before and after experimentation is not possible, as the gold layer would change the behaviour of coated samples. Typical failure that can be observed are fibre failure, matrix cracks, delaminations. While certain failures could not be observed with microscopy or mass loss measurements, SEM images revealed surface degradation in the work of Macdonald et al. (Macdonald, Nash and Stack, 2019).



**Figure 46: SEM image showing fibre breakage observed after 50 impacts of 20mm hailstones at a velocity around 90m/s [Source: Macdonald2019]**

Together with SEM, Energy Dispersive X-Ray spectroscopy (EDX) can be used. EDX is an analytical technique used for the elemental analysis or chemical characterization of a sample. It relies on an interaction of a source of X-ray excitation and the sample (Russ, 2013). Its characterization capabilities are due in large part to the fundamental principle that each element has a unique atomic structure allowing a unique set of peaks on its electromagnetic emission spectrum (which is the main principle of spectroscopy). It is considered to be a semi-quantitative method. The depth of penetration of the electrons is dependent on the material and accelerating voltage. X-rays may be produced over a significant fraction of the electron interaction volume. Whitehead et al. (Whitehead *et al.*, 2011) studied the depth dependent concentration of Si in the Ni matrix they investigated as a coating materials from EDX measurements by varying the accelerating voltages of a range 5–25 kV and fitting the data using a Monte Carlo simulation method. Mishnaevsky et al. (Mishnaevsky Jr *et al.*, 2020) investigated the chemistry of the top coating and the filler by EDX

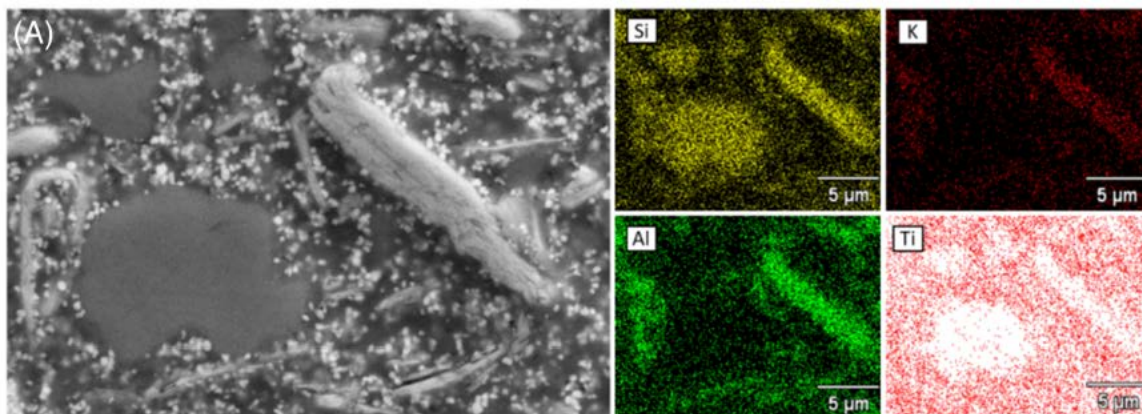


**Figure 47: SEM and EDX images: A, Scanning electron microscopy (SEM) image of the top coating with four energy-dispersive spectrometry (EDX) images of Si, K, Al, and Ti. [Modified from [Mishnaevsky2019]**

### 6.3.5 Nuclear magnetic resonance (NMR)

The application of nuclear magnetic resonance (NMR) spectral characterisation to determine character of the materials, and how it might be used to determine how they change, is included here for completeness. NMR spectroscopy involves observing the reactions of atomic nuclei when exposed to a strong constant magnetic field as they are perturbed by a weak oscillating magnetic field (in the near field). The nuclei respond by producing an electromagnetic signal with a frequency characteristic of the magnetic field at the nucleus. By recording the signals from the same nucleus in different electronic environments (in the molecule) yields a spectrum which enables the chemical structure to be determined. However, not all atomic nuclei are able to yield NMR spectra (the most commonly used are  $^1\text{H}$ ,  $^{13}\text{C}$ , and  $^{15}\text{N}$ ) and while the solution spectra may display relatively sharp chemical shifts. It is possible to perform analysis of solid (insoluble samples) using cross-polarisation-magic angle spinning  $^{13}\text{C}$  NMR, but the signals are comparatively more broad since the nuclei are less mobile and less able to respond to the weak oscillating magnetic field.

## 6.4 Non-destructive testing methods

### 6.4.1 Microscopy

Confocal, laser or light microscopes (discussed in Section 6.1.1) can also be used to assess the surface damage and surface topography non-destructively. For instance, the confocal microscope (Keyence VR-5000) can be used to evaluate the early forms of damage in tested samples. The microscope incorporates a 3D imaging and measurement system able to investigate the height-map of the damaged area. A low magnification with wide field of view can be used for the general evaluation of the damages. Height maps can be obtained and evaluated, see Figure 41. And the damaged area as well as damage volume can be measured from this. A higher magnification and resolution settings can be used to evaluate further specific damage features in more detail. Care should be taken to setting the base plane in the microscope. With a light microscope, the damage area can also be evaluated but part of the 3D information then is lost, see Figure 41.

### 6.4.2 C-scan

To check the homogeneity of the materials, or the porosity, damage or de-laminations in the materials, high frequency (10 MHz) ultrasonic C-scan can be used. A pulse-echo transducer sends a sound wave from one probe through the other. A single through transmission mode can be used to analyse the differences within the material, with water as a contact medium. The speed of the scans determines the grid length and width and thereby also the accuracy of the scans. The output data of the C-scan is given in dB (signal strength) values which need to be corrected for thickness differences between the samples if a comparison needs to be made between different samples. A typical C-scan image of a delaminated panel through impact is shown in Figure 48. The method can be used for the identification of locations of defects or damage and for thickness measurements. It is a fast and reliable method and has been used as quality control technique for several years.

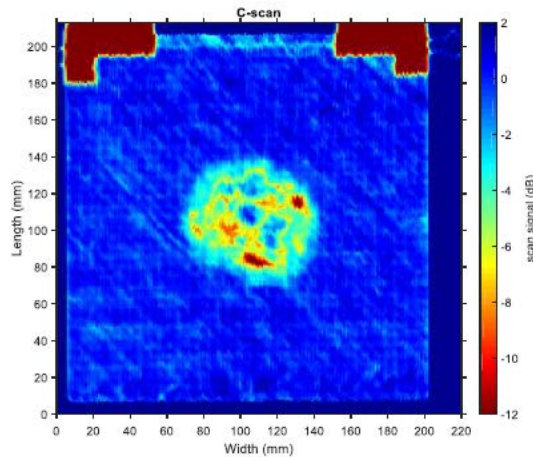
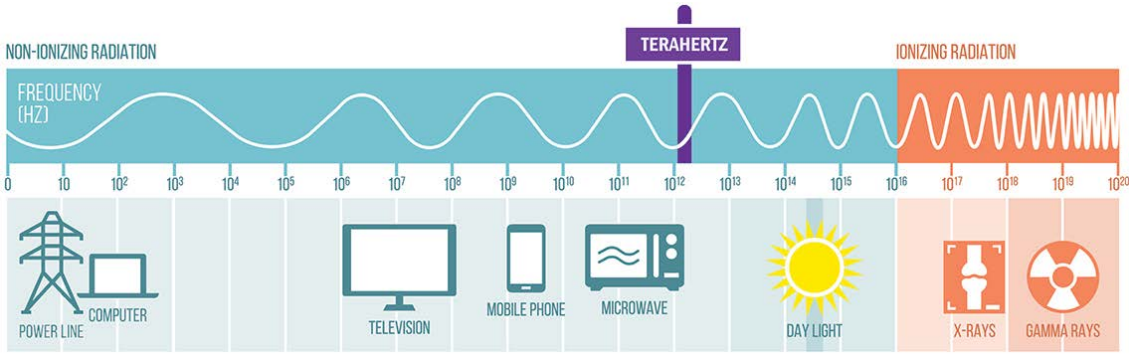


Figure 48: C-scan image of a sample with de-laminations due to hailstone impact [Courtesy of Huseyin Eryoruk, TUDelft].

### 6.4.3 Terahertz scanners

Terahertz (THz) waves (Figure 49) can be used to control the thickness of coating materials (single or multilayer) and to detect defects in the materials or at the interface. Most of dielectric materials are indeed semi-transparent to THz waves. The good spatial resolution (sub-mm) makes THz technology suitable for non-destructive testing, enabling a contactless and non-ionizing control of dielectric materials and coated metallic substrates.

The technique is already applied in automotive, marine, aerospace, semiconductor and pharmaceutical sectors (Zhong, 2019) and has been introduced in the wind industry a few years ago ([www.das-nano.com](http://www.das-nano.com)).



**Figure 49: TeraHertz waves are sub-millimetric waves in the electromagnetic spectrum.**

Picture from: <https://subterandt.com/company/about-terahertz/>

Several configurations of THz waves inspections exist, depending on the signal shape, used frequency range, power source level and beam capture technology (Zhong, 2019). **Time domain analysis of the reflection of pulsed waves (pulsed THz-TDS) technology** is advantageous in terms of thickness measurement and detection/localization of defects on samples that are only accessible from one side. Technology based on the evaluation of absorption in transmitted waves have an advantage through a lower complexity and cost, but lack capabilities in the localization of defects and are therefore not suited for the inspection of complex structures such as wind turbine blade leading edge systems.

THz waves are sensitive to change in refraction index, meaning that part of the incident signal will be reflected at the interface between layers. The principle of pulsed THz-TDS is described here below and illustrated in Figure 50.

- A pulse is sent to the sample to control,
- Discontinuities in the refraction index cause reflections,
- Reflections are separated in time due to the thickness of the layers,
- Analysing the position and amplitude of the reflections provides information about the thickness and type of layers.

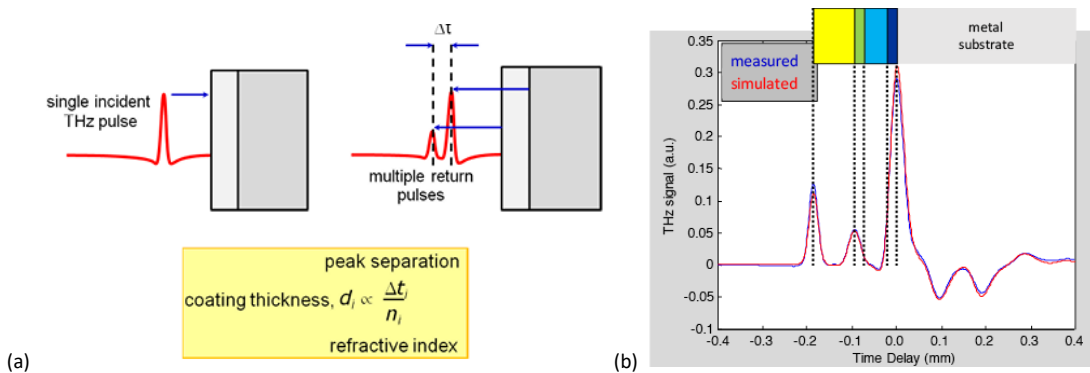


**Figure 50: Illustration of THz pulsed time-domain spectroscopy for single (a) and multilayer (b) coating on metallic substrate. The coating thickness is proportional to the separation between reflection peaks. There is**

**proportional relationship between the amplitude of individual reflections and the relative change in refractive index throughout the corresponding interface. From: [www.teraview.com](http://www.teraview.com)**

The company das-Nano, together with the Fraunhofer Institute, has developed a system called Notus that enables the inspection of coating layers on top of composite materials used in wind turbine blades (<https://das-nano.com/notus-system/#resources>). The full thickness of coating layers is measured. Moreover the systems offers another feature: the measurement of the adhesion between two layers in a non-destructive way, as opposed to pull-off test. The Notus system shown in Figure 51 has been developed to operate in lab, factory and field environment. The equipment is composed of a portable cart containing the THz core, electronics and vacuum systems, and a vacuum-powered measurement head that can be placed on the blade, containing the THz-transceiver module. The head has an extended position for leading edge inspection.



**Figure 51: (left) Notus system for non-destructive inspection of coating thickness and adhesion based on THz-TDS spectroscopy technology and (right) extended head position for leading edge inspection. On courtesy of das-Nano.**

Prior to the measurements, it is preferred to introduce information about the sample to be tested. Several sample configurations are pre-defined (Figure 52) and these includes the number of layers and associated thickness range (for pass/fail criteria).

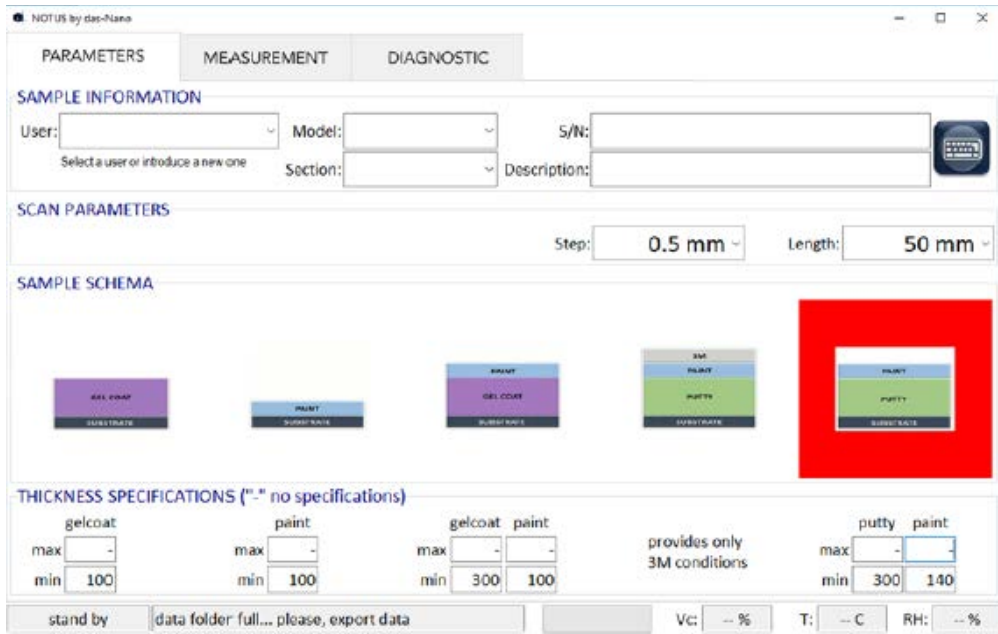


Figure 52: Configuration of sample parameters prior to measurement. Courtesy of das-Nano

As an example, results of inspections are displayed in Figure 53 for a gelcoat + pain system applied on a substrate. The thickness profile and statistics (min, max, avg, std values) are shown for the measured spot. Adhesion values are also given. This can of course be repeated along the blade leading edge at multiple spots.

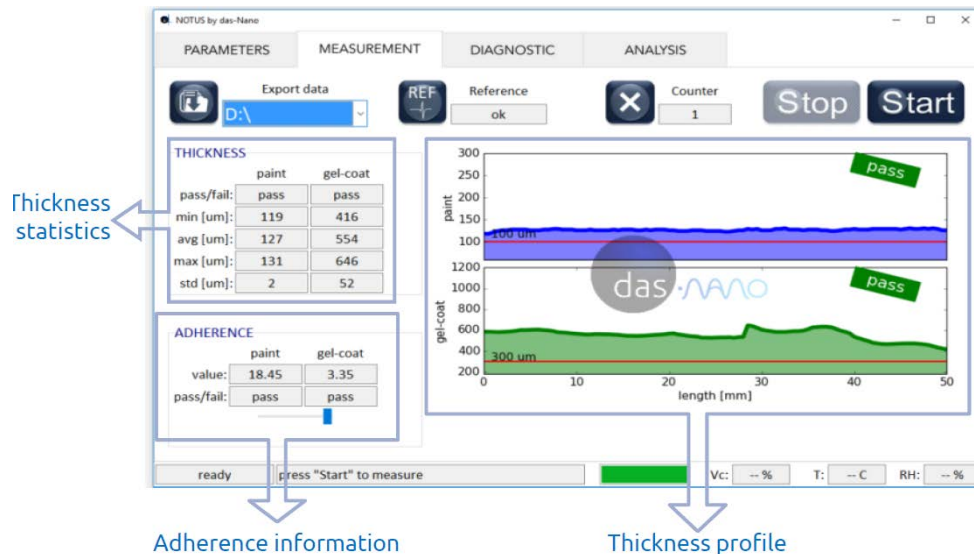


Figure 53: Overview of THz-TDS inspection results. Courtesy of das-Nano.

Terahertz (THz) scanners are based on mm waves and can be used for thickness measurements, as this can be done fairly quick and with very good penetration. The advantage is that it has many of the

same benefits of Optical coherence tomography (OCT) – see section 3.5 - but with much better penetration due to longer mm wavelength. The 3D imaging is however very time consuming and resolution is similar to high-frequency ultrasound, so small defects like bubbles are not seen.

#### 6.4.4 Optical coherence tomography

Optical coherence tomography (OCT) is an interferometric technique based on the scattering from internal microstructures and material interfaces. It was developed in 1991 for biomedical imaging and is widely used today as a diagnostic tool within ophthalmology, dermatology, and cardiology (Huang *et al.*, 1991)(Israelsen *et al.*, 2018). In recent years the technology has also found applications within non-destructive testing (NDT) and imaging. Since it is based on low-intensity laser light, it can reach a microscopic resolution, is non-destructive, and does not require a contact medium like ultrasound. The challenge of OCT is that light is gradually lost when propagating through a material due to scattering and absorption, which limits its penetration depth significantly compared to e.g. ultrasound.

There have been few reports on OCT applied for inspection of coatings, primarily for art and cultural heritage preservation, as well as automotive and pharmaceutical coatings. Within automotive coatings, OCT operating around the 830 to 930 nm central wavelength range has been used to map the thickness of individual coating layers with an axial resolution of around 4–6  $\mu\text{m}$ , but due to the short central wavelength, only the top clear coat layer was transparent, limiting the maximum penetration depth to about 100  $\mu\text{m}$  (Dong *et al.*, 2016)(Wang *et al.*, 2019)(Zhang *et al.*, 2016)(Zhang *et al.*, 2017). Zhang *et al.* (Zhang *et al.*, 2016) characterized automotive paints with metal flakes using OCT at 832 nm and were in some cases able to distinguish the clear coat, base coat, and primer layers, each around 20–60  $\mu\text{m}$  with a depth resolution of 5  $\mu\text{m}$ . In their system, a  $2 \times 2$  mm scan of  $1536 \times 600 \times 2048$  pixels was acquired in  $\sim 45$  s and took  $\sim 60$  s to process (Zhang *et al.*, 2016). Moving into the mid-infrared, Cheung *et al.* (2015) used a broadband SC laser to compare OCT at 930 and 1960 nm central wavelength for inspection of artistic oil paintings and found that despite the lower axial resolution of 13  $\mu\text{m}$ , the longer wavelength was able to penetrate the  $\sim 340$   $\mu\text{m}$  layer of yellow ochre pigmented paint and provide more structural information about the chalk base layer below (Cheung *et al.*, 2015). More recently, Zorin *et al.* presented improved penetration in oil paints using 4  $\mu\text{m}$  central wavelength, although with a poor axial (depth) resolution of 50  $\mu\text{m}$  and a slow line rate of 2.5 Hz (Zorin *et al.*, 2018). Fast scanning and high-resolution in the mid-infrared was first demonstrated by Israelsen *et al.*, achieving a 3 kHz line rate and 5.8  $\mu\text{m}$  axial resolution (Israelsen *et al.*, 2019)(Israelsen *et al.*, 2021). The first study to investigate industrial coatings in the mid-infrared was by Petersen *et al.* that demonstrated subsurface imaging in Marine coatings, including monitoring of wet film thickness during curing of a 210  $\mu\text{m}$  blue-pigmented anti-fouling coating based on cuprous oxide particles, and detection of substrate corrosion through 369  $\mu\text{m}$  white-pigmented high-gloss (HG) alkyd enamel (Petersen *et al.*, 2021). In this study, the surface roughness and large functional particles presented the main limitations in terms of penetration depth.

So far, there has been no work published with OCT in relation to wind turbine coatings. Liu *et al.* used OCT with a central wavelength of 1550 nm to monitor delamination growth in an uncoated fiber-glass epoxy composite used for the spar webs in wind turbine blades (Liu, Groves and Benedictus, 2014). They were able to image the delamination through 2 mm of the composite material with an axial resolution of 17  $\mu\text{m}$  and a scan speed of 4 mm/s. Figure 54 shows a proof-of-concept study on defect detection in leading edge coatings using OCT at 4  $\mu\text{m}$  central wavelength performed by DTU Fotonik

and DTU Wind Energy. In the study, a fiber-glass substrate was coated with a few mm thick coating designed to absorb and dissipate the impact energy of rain drops, potentially minimizing rain erosion. Impacts were simulated using spherical polymer projectiles propelled by a spring, and the resulting impact crater is shown in Figure 54(a). At the impact crater the coating was severely damaged, removing any sign of potential defects that could have led to coating failure. However, just at the rim of the crater a 3D OCT scan revealed several subsurface voids that were not visible from the surface (see Figure 54(d)-(f)). Due to the strong reflection from the interface between coating and air these defects are very easy to see using OCT. The large void in Figure 54(e), is estimated to be around 546  $\mu\text{m}$  in diameter, but because of strong scattering and absorption inside the coating the penetration depth was limited to about 2-300  $\mu\text{m}$ . To detect voids or other defects below this threshold requires further developments in terms of detection sensitivity, and longer wavelength lasers. Although published work within OCT for coatings inspection has been performed using stationary laboratory setups, the OCT technology can be implemented in field instruments that can operate in an industrial setting. Figure 55 shows a series of photos of a field prototype system developed at DTU Fotonik that was brought to a wharf to inspect marine coatings in the research project SHIP-COAT. OCT is therefore expected to be applicable for industrial inspection of wind turbine coatings as part of the post-fabrication quality assurance.

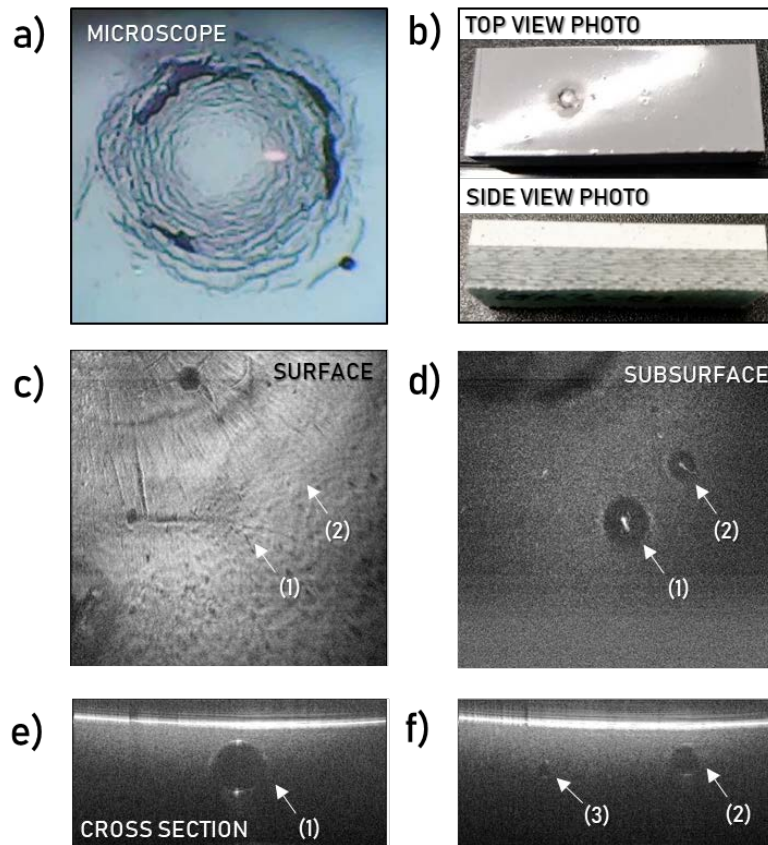


**Figure 54: (UNPUBLISHED) Proof-of-concept study on defect detection in leading edge coatings for wind turbine blades. (a) Projectile impact crater viewed under microscope. (b) Sample photographs. (c) OCT surface topography from the edge of the impact crater where the surface was still relatively intact. (d) OCT**

subsurface volume projection from the same area as (c), revealing subsurface voids. (e),(f) OCT cross sections of the voids.



Figure 55. (a) Photograph by Bax Lindhart © 2021 showing the prototype being tested at DTU Fotonik. (b,c) OCT prototype in action scanning marine coatings directly on marine vessels at the Yacht Service wharf in Copenhagen, Denmark.

## 6.5 Reflections on microstructure characterisation and non-destructive testing methods

For the microstructure characterisation of a coated surface, several non-destructive techniques are available that could give useful information on erosion damage, both from a surface topography (microscopy and AFM), appearance (gloss, visual inspection) as well as chemical point of view (Spectroscopy). These tests can be performed during the erosion testing to characterise the behaviour of the coated samples over time.

When more understanding is needed on the damage inside the sample due to rain erosion (testing), there are both destructive and non-destructive test techniques which could be interesting.

With the destructive testing, only the damage at one moment in time is captured, leading to multiple test samples to get a full overview of the damage progression over time. Established destructive testing methods are cross-sectional microscopy, X-ray tomography, luminescence microscopy, SEM/EDX and NMR. When performing cross-sectional microscopy, care needs to be taken in where the sample is cut and whether the 2D cross-section is representative for the 3D damage case being analysed. The resolution of X-ray tomography and SEM/EDX is a lot higher than the cross-sectional microscopy, but the size of the sample that can be analysed is rather small. X-ray tomography gives a full 3D image of the sample analysed, while SEM is again performed on a cross-section or damaged part, given limited 3D information, which could be relevant for rain erosion characteristics. Luminescence microscopy will give more information on the cracks on the surface of the coating, while providing limited information of subsurface phenomena. Looking at all the current destructive testing methods, it can be observed that only X-ray tomography provides a full 3D picture of the damaged coated sample (limited sample size, high resolution) while the other techniques gives

information mostly of a cross-section of the coated sample (large sample size, lower resolution) or cracks on the surface of the coating (lower sample size, higher resolution).

The non-destructive testing methods for the understanding of the damage inside the sample are the most interesting as information can be captured on the state of the sample during testing and thereby provide information on damage and damage progression during rain erosion (testing). Microscopy as discussed before provides only surface information, while C-scan can give more information about the different damage modes (matrix cracks, delamination and their location depending on the resolution of the technique). Interesting developments have been taken place to detect defects (size and location spatially) inside the multi-material samples through TeraHerz scanners, where depending on the mode (reflective/transmission) different type of information can be obtained through thickness of the sample/blade. The current drawbacks are the resolution (not able to detect small defects such as voids) and the time required for 3D scanning. Further research and development is needed to combine this technique with phase arrays. It however provides better depth penetration compared to Optical Coherence Tomography (OCT), which is also an interesting technique to obtain 3D damage information spatially. OCT can detect very small defects and phenomena happening close to the coating surface.

## 7 Conclusions and recommendations for future work

This report gives a review of the available technologies for laboratory erosion testing of wind turbine blades and coatings, under the following five categories:

1. Rain erosion tests
2. Impact tests and fatigue
3. Viscoelastic properties
4. Fracture mechanics of Layered structures
5. Microstructure & NDA

In order to advance the current technologies for testing of wind turbine blades and coatings, a number of potential research areas have been identified, which are discussed in the remainder of this chapter.

Many modern leading edge protection systems are viscoelastic and have time dependent behaviour. On a wind turbine rain periods are interspersed with dry periods, where there is potential for viscoelastic recovery to occur. This has been noted to influence the time to failure in rain erosion tests, via inspection periods or non-test periods over the weekends. The order of sequence in which they occur could also be critical if the embrittlement is sufficient to be unrecoverable. The influence of droplet size distribution is another area that is not well understood.

In terms of fatigue damage due to impacts, an investigation into the effect of impact rate in fatigue performance would be an area that needs further study. Results have been presented from trials using single point impact fatigue testing, where it would be beneficial to compare these results to with the results from water jet tests.

The tensile pull-off test and the double cantilever beam test, along with discussion on damage and fracture of filled elastomers and the fracture tests for adhesion between polymers and a composite substrate, have been presented in this report. However, further adaptations of these tests could be investigated to improve adhesion of leading edge protection systems to the wind blade substrate, along with incorporating impact testing for initial trials of materials for the next generation of leading edge protection systems.

For the microstructure characterisation of a coated surface, several non-destructive techniques are available that could give useful information on erosion damage, both from a surface topography (microscopy and AFM), appearance (gloss, visual inspection) as well as chemical point of view (spectroscopy). These tests can be performed during the erosion testing to characterise the behaviour of the coated samples over time. Interesting developments have been taken place to detect defects (size and location spatially) inside the multi-material samples through TeraHerz scanners, where depending on the mode (reflective/transmission) different type of information can be obtained through thickness of the sample/blade. The current drawbacks are the resolution (not able to detect small defects such as voids) and the time required for 3D scanning. Further research and development is needed to combine this technique with phase arrays. It however provides better depth penetration compared to Optical Coherence Tomography (OCT), which is also an interesting technique to obtain 3D damage information spatially. OCT can detect very small defects and phenomena happening close to the coating surface.

## References

- Adler, W. F. (1999) 'Rain impact retrospective and vision for the future', *Wear*, 233–235, pp. 25–38. doi: [https://doi.org/10.1016/S0043-1648\(99\)00191-X](https://doi.org/10.1016/S0043-1648(99)00191-X).
- Arabatzi, I. *et al.* (2019) 'Multi-criteria decision-making methodology for the selection of cargo hold coating for bulk carriers', *Ships and Offshore Structures*. Taylor & Francis, 14(6), pp. 609–630.
- ASTM (2010) 'G73-10: Standard Test Method for Liquid Impingement Erosion Using Rotating Apparatus', *Astm*, i, pp. 1–19. doi: 10.1520/G0073-10.2.
- ASTM, D. (2015) '5026-15, "Standard test method for plastics: Dynamic mechanical properties: In Tension,"' in *Am. Soc. Test. Mater.*
- Babin, P. *et al.* (2006) 'Fast X-ray tomography analysis of bubble growth and foam setting during breadmaking', *Journal of Cereal Science*. Elsevier, 43(3), pp. 393–397.
- Bech, J. I., Hasager, C. B. and Bak, C. (2018) 'Extending the life of wind turbine blade leading edges by reducing the tip speed during extreme precipitation events', *Wind Energy Science*. Copernicus GmbH, 3(2), pp. 729–748.
- Beda, T. *et al.* (2013) 'Viscoelastic Moduli of Materials Deduced from Harmonic Responses of Beams', *Mechanics of Viscoelastic Materials and Wave Dispersion*. Wiley Online Library, pp. 555–597.
- Borg, R., Nilsson, L. and Simonsson, K. (2004) 'Simulating DCB, ENF and MMB experiments using shell elements and a cohesive zone model', *Composites Science and Technology*. Elsevier, 64(2), pp. 269–278.
- Bowden, F. P. and Brunton, J. H. (1961) 'The deformation of solids by liquid impact at supersonic speeds', *Proceedings of the Royal Society of London. Series A. Mathematical and Physical Sciences*. The Royal Society London, 263(1315), pp. 433–450.
- Brinson, H. F. and Brinson, L. C. (2015) 'Stress and strain analysis and measurement', in *Polymer Engineering Science and Viscoelasticity*. Springer, pp. 15–55.
- Busch, H. *et al.* (1966) 'Rain erosion properties of materials', *Philosophical Transactions for the Royal Society of London. Series A, Mathematical and Physical Sciences*. JSTOR, pp. 168–181.
- Chen, J. H. *et al.* (1999) 'A modification of the mixed-mode bending test apparatus', *Composites Part A: applied science and manufacturing*. Elsevier, 30(7), pp. 871–877.
- Cherry, S. M. *et al.* (1979) 'Measurement of raindrop-size distributions using dual-polarisation radar', in *5th International Conference on Erosion by Solid and Liquid Impact, Cavendish Lab., Cambridge Univ., United Kingdom*.
- Cheung, C. S. *et al.* (2015) 'High resolution Fourier domain optical coherence tomography in the 2  $\mu$ m wavelength range using a broadband supercontinuum source', *Optics Express*. Optical Society of America, 23(3), pp. 1992–2001.
- Cho, J. U. *et al.* (2012) 'High-strain-rate fracture of adhesively bonded composite joints in DCB and TDCB specimens', *International Journal of Automotive Technology*. Springer, 13(7), pp. 1127–1131.
- Cook, S. S. (1928) 'Erosion by water-hammer', *Proceedings of the Royal Society of London. Series A, Containing Papers of a Mathematical and Physical Character*. The Royal Society London, 119(783), pp. 481–488.

- Cortés, E. *et al.* (2017) 'On the material characterisation of wind turbine blade coatings: The effect of interphase coating-laminate adhesion on rain erosion performance', *Materials*, 10(10). doi: 10.3390/ma10101146.
- Dashtkar, A. *et al.* (2019) 'Rain erosion-resistant coatings for wind turbine blades: A review', *Polymers and Polymer Composites*. SAGE Publications Sage UK: London, England, 27(8), pp. 443–475.
- Deom, A. and Balageas, D. L. (1995) 'Rain erosion resistance of infrared materials- Comparison of rotating arms and Multiple Impact Jet Apparatus(MIJA) measurements', in *European Electromagnetic Structures Conference, 8 th, Nottingham, United Kingdom, Sept. 6, 7*, p. 1995.
- DNV-GL (2018) 'DNVGL-RP-0171 Edition February 2018 Testing of rotor blade erosion protection systems'. DNV-GL.
- Domenech, L. *et al.* (2020) 'Top coating anti-erosion performance analysis in wind turbine blades depending on relative acoustic impedance. Part 1: Modelling approach', *Coatings*. MDPI, 10(7), p. 685.
- Dong, Y. *et al.* (2016) 'Nondestructive analysis of automotive paints with spectral domain optical coherence tomography', *Applied Optics*. Optica Publishing Group, 55(13), pp. 3695–3700.
- Eberlein, R., Fukada, Y. and Pasiaka, L. (2021) 'Fatigue Life Analysis of Solid Elastomer-Like Polyurethanes', *Advances in Polymer Science*, 286(December), pp. 179–202. doi: 10.1007/12\_2020\_68.
- Eisenberg, D., Laustsen, S. and Stege, J. (2018) 'Wind turbine blade coating leading edge rain erosion model: Development and validation', *Wind Energy*. Wiley Online Library, 21(10), pp. 942–951.
- Eskilsson, S. (1965) 'Rain erosion testing facilities at Saab and some test results', in *Proceeding of the Rain Erosion Conference*, pp. 43–48.
- Fæster, S. *et al.* (2021) 'Rain erosion of wind turbine blades and the effect of air bubbles in the coatings', *Wind Energy*, (November 2020), pp. 1–12. doi: 10.1002/we.2617.
- Fan, J. T., Weerheijm, J. and Sluys, L. J. (2015) 'High-strain-rate tensile mechanical response of a polyurethane elastomeric material', *Polymer*. Elsevier Ltd, 65, pp. 72–80. doi: 10.1016/j.polymer.2015.03.046.
- Fernandes, R. L. and Campilho, R. (2017) 'Testing different cohesive law shapes to predict damage growth in bonded joints loaded in pure tension', *The Journal of Adhesion*. Taylor & Francis, 93(1–2), pp. 57–76.
- Ferry, J. D. (1980) *Viscoelastic properties of polymers*. John Wiley & Sons.
- Field, J. E. (1991) 'The physics of liquid impact, shock wave interactions with cavities, and the implications to shock wave lithotripsy', *Physics in Medicine & Biology*. IOP Publishing, 36(11), p. 1475.
- Field, J. E. *et al.* (1994) *Studies of Rain Erosion Mechanisms in a Range of IR Transmitting Ceramics-Including Coated Samples*. CAMBRIDGE UNIV (UNITED KINGDOM) CAVENDISH LAB.
- Field, J. E., Lesser, M. B. and Dear, J. P. (1985) 'Studies of two-dimensional liquid-wedge impact and their relevance to liquid-drop impact problems', *Proceedings of the Royal Society of London. A. Mathematical and Physical Sciences*. The Royal Society London, 401(1821), pp. 225–249.
- Fraisse, A. *et al.* (2018) 'Impact fatigue damage of coated glass fibre reinforced polymer laminate', *Renewable Energy*, 126, pp. 1102–1112. doi: <https://doi.org/10.1016/j.renene.2018.04.043>.
- Fujisawa, N. *et al.* (2018) 'Experiments on liquid droplet impingement erosion on a rough surface',

- Wear. Elsevier B.V., 398–399(July 2017), pp. 158–164. doi: 10.1016/j.wear.2017.12.003.
- Fyall, A. A. (1965) ‘Meteorological parameters relevant to the phenomenon of rain erosion’, in *Proceedings of the First International Conference on Rain Erosion and Associated Phenomena, Meersburg, Germany*, pp. 5–7.
- Galeski, A. (2002) ‘Dynamic mechanical properties of crystalline polymer blends. The influence of interface and orientation’, *e-Polymers*. De Gruyter, 2(1).
- Garcea, S. C., Wang, Y. and Withers, P. J. (2018) ‘X-ray computed tomography of polymer composites’, *Composites Science and Technology*. Elsevier, 156, pp. 305–319.
- Geißler, G. and Kaliske, M. (2010) ‘Time-dependent cohesive zone modelling for discrete fracture simulation’, *Engineering Fracture Mechanics*. Elsevier, 77(1), pp. 153–169.
- Goldstein, J. I. *et al.* (2017) *Scanning electron microscopy and X-ray microanalysis*. Springer.
- Grate, J. W., Wenzel, S. W. and White, R. M. (1992) ‘Frequency-independent and frequency-dependent polymer transitions observed on flexural plate wave ultrasonic sensors’, *Analytical Chemistry*. ACS Publications, 64(4), pp. 413–423.
- Gunn, R. and Kinzer, G. D. (1949) ‘The terminal velocity of fall for water droplets in stagnant air’, *Journal of Atmospheric Sciences*, 6(4), pp. 243–248.
- Ha, C.-S. *et al.* (1998) ‘Fracture toughness and properties of plasticized PVC and thermoplastic polyurethane blends’, *Polymer*. Elsevier, 39(20), pp. 4765–4772.
- Hasager, C. *et al.* (2020) ‘Assessment of the rain and wind climate with focus on wind turbine blade leading edge erosion rate and expected lifetime in Danish Seas’, *Renewable Energy*, 149, pp. 91–102. doi: 10.1016/j.renene.2019.12.043.
- Hasager, C. *et al.* (2021) ‘How can we combat leading-edge erosion on wind turbine blades?’, in *DTU International Energy Report 2021: Perspectives on Wind Energy*. DTU Wind Energy, pp. 134–142.
- Herring, R. *et al.* (2019) ‘The increasing importance of leading edge erosion and a review of existing protection solutions’, *Renewable and Sustainable Energy Reviews*. Elsevier, 115, p. 109382.
- Heymann, F. J. (1967) ‘A survey of clues to the relation between erosion rate and impact parameters’, in *Second Rain Erosion Conference*, pp. 683–760.
- Heymann, F. J. (1970) ‘Toward quantitative prediction of liquid impact erosion’. ASTM International.
- Heymann, F. J. (1979) ‘Conclusions from the ASTM interlaboratory test program with liquid impact erosion facilities’, in *In: International Conference on Erosion by Liquid and Solid Impact*, pp. 20\_1-20\_10.
- Honegger, E. (1924) ‘Corrosion and erosion of steam turbine blading’, *Brown Boveri Rev*, 12, pp. 263–278.
- Honegger, E. (1927) ‘Tests on erosion caused by jets’, *Brown Boveri Rev*, 14(4), pp. 95–104.
- Hong, C. S. and Yoon, S. H. (1990) ‘Modified end notched flexure specimen for mixed mode interlaminar fracture in laminated composites’, *International Journal of Fracture*. Springer, 43, pp. R3–R9.
- Hu, W. *et al.* (2021) ‘A computational framework for coating fatigue analysis of wind turbine blades due to rain erosion’, *Renewable Energy*. Elsevier Ltd, 170, pp. 236–250. doi:

10.1016/j.renene.2021.01.094.

Huang, D. *et al.* (1991) 'Optical coherence tomography', *science*. American Association for the Advancement of Science, 254(5035), pp. 1178–1181.

Hurley, C. J. and Schmitt Jr, G. F. (1970) *Development and calibration of a Mach 1.2 rain erosion test apparatus*. DAYTON UNIV OH RESEARCH INST.

Israelsen, N. M. *et al.* (2018) 'The value of ultrahigh resolution OCT in dermatology-delineating the dermo-epidermal junction, capillaries in the dermal papillae and vellus hairs', *Biomedical optics express*. Optical Society of America, 9(5), pp. 2240–2265.

Israelsen, N. M. *et al.* (2019) 'Real-time high-resolution mid-infrared optical coherence tomography', *Light: Science & Applications*. Nature Publishing Group, 8(1), pp. 1–13.

Israelsen, N. M. *et al.* (2021) 'High-resolution mid-infrared optical coherence tomography with kHz line rate', *Optics Letters*. Optica Publishing Group, 46(18), pp. 4558–4561.

Jha, P. *et al.* (2018) 'Ball impact induced elastico-mechanoluminescence for impact sensor', *Journal of Luminescence*. Elsevier, 195, pp. 40–43.

Jiang, L. *et al.* (2021) 'A new model characterizing the fatigue delamination growth in DCB laminates with combined effects of fiber bridging and stress ratio', *Composite Structures*. Elsevier, 268, p. 113943.

Jones, D. M. A. (1959) 'The shape of raindrops', *Journal of Atmospheric Sciences*, 16(5), pp. 504–510.

Kanyanta, V. and Ivankovic, A. (2010) 'Mechanical characterisation of polyurethane elastomer for biomedical applications', *Journal of the mechanical behavior of biomedical materials*. Elsevier, 3(1), pp. 51–62.

Kastner, J. *et al.* (2010) 'A comparative study of high resolution cone beam X-ray tomography and synchrotron tomography applied to Fe-and Al-alloys', *Ndt & E International*. Elsevier, 43(7), pp. 599–605.

Katsivalis, I. *et al.* (2020) 'Development of cohesive zone models for the prediction of damage and failure of glass/steel adhesive joints', *International Journal of Adhesion and Adhesives*. Elsevier, 97, p. 102479.

Katsivalis, I. *et al.* (2022) 'Mechanical and interfacial characterisation of leading-edge protection materials for wind turbine blade applications', *Wind Energy*. Wiley Online Library.

King, R. B. and Gunn, N. J. F. (1970) 'The influence of rain erosion damage on subsequent fatigue strength of metals', in *Third rain erosion conference*, pp. 243–259.

Kinloch, A. J. *et al.* (2012) 'Using the simple peel test to measure the adhesive fracture energy, Ga', in *Proceedings of the 35th Annual Meeting of the US Adhesion Society*.

Kirols, H. S. *et al.* (2015) 'The effect of initial surface roughness on water droplet erosion behaviour', *Wear*. Elsevier, 342–343, pp. 198–209. doi: 10.1016/j.wear.2015.08.019.

Kong, K. *et al.* (2020) 'Experimental characterisation and micromechanical models for luminescent phosphors incorporated with nonwoven veil-polymer composites', *Composites Part B: Engineering*. Elsevier, 202, p. 108444.

LAPP, R. O. Y. R., STUTZMAN, R. H. and WAHL, N. E. (1954) *A study of the rain erosion of plastics and metals*. CORNELL AERONAUTICAL LAB INC BUFFALO NY.

Lapp, R. R., Stutzman, R. H. and Wahl, N. E. (1956) *Summary Report on the Rain Erosion of Aircraft Materiels*. Wright Air Development Center, Air Research and Development Command, United ...

Law, H. and Koutsos, V. (2020) 'Leading edge erosion of wind turbines: Effect of solid airborne particles and rain on operational wind farms', *Wind Energy*, 23(10), pp. 1955–1965. doi: 10.1002/we.2540.

Lee, D.-J. (2016) 'Fracture mechanical model for tensile strength of particle reinforced elastomeric composites', *Mechanics of Materials*. Elsevier, 102, pp. 54–60.

Lee, M. J. *et al.* (2010) 'Determination of cohesive parameters for a mixed-mode cohesive zone model', *International Journal of Adhesion and Adhesives*. Elsevier, 30(5), pp. 322–328.

Leishman, G. *et al.* (2022) 'A novel approach for wind turbine blade erosion characterization: an investigation using surface gloss measurement', *Coatings*. MDPI, 12(7), p. 928.

Leon, M., Fæster, S. and Rad, S. D. (2020) 'Mechanisms and computational analysis of leading edge erosion of wind turbine blades', in *IOP Conference Series: Materials Science and Engineering*. IOP Publishing, p. 12025.

Liu, P., Groves, R. M. and Benedictus, R. (2014) '3D monitoring of delamination growth in a wind turbine blade composite using optical coherence tomography', *Ndt & E International*. Elsevier, 64, pp. 52–58.

Macdonald, H., Nash, D. and Stack, M. M. (2019) 'Repeated impact of simulated hail ice on glass fibre composite materials', *Wear*. Elsevier, 432, p. 102926.

Malikov, A. K. ugli *et al.* (2021) 'Ultrasonic assessment of thickness and bonding quality of coating layer based on short-time fourier transform and convolutional neural networks', *Coatings*. MDPI, 11(8), p. 909.

Marrion, A. (2004) *The chemistry and physics of coatings*. Royal Society of Chemistry.

Marshall, J. S. (1948) 'The distribution of raindrops with size', *J. meteor.*, 5, pp. 165–166.

Mason, P. (1958) 'High-speed fracture in rubber', *Journal of Applied Physics*, 29(8), pp. 1146–1150. doi: 10.1063/1.1723392.

Menard, K. P. and Menard, N. R. (2020) *Dynamic mechanical analysis*. CRC press.

Methven, T. J. and Fairhead, B. (1960) 'A correlation between rain erosion of perspex specimens in flight and on a ground rig'.

Mishnaevsky Jr, L. *et al.* (2020) 'Micromechanisms of leading edge erosion of wind turbine blades: X-ray tomography analysis and computational studies', *Wind Energy*. Wiley Online Library, 23(3), pp. 547–562.

Mishnaevsky, L. *et al.* (2020) 'Micromechanisms of leading edge erosion of wind turbine blades: X-ray tomography analysis and computational studies', *Wind Energy*, 23(3), pp. 547–562. doi: 10.1002/we.2441.

Moon Jeong, S. *et al.* (2013) 'Mechanically driven light-generator with high durability', *Applied Physics Letters*. American Institute of Physics, 102(5), p. 51110.

de Moura, M. F. S. F. (2006) 'Numerical simulation of the ENF test for the mode-II fracture characterization of bonded joints', *Journal of Adhesion Science and Technology*. Taylor & Francis, 20(1), pp. 37–52.

- Nash, D. *et al.* (2021) 'A staged approach to erosion analysis of wind turbine blade coatings', *Coatings*. MDPI, 11(6), p. 681.
- O'Carroll, A. (2018) 'Correlation of mechanical properties to rain erosion resistance of polymeric materials'.
- O'Carroll, A. *et al.* (2018) 'Correlation of the rain erosion performance of polymers to mechanical and surface properties measured using nanoindentation', *Wear*. Elsevier B.V., 412–413(July), pp. 38–48. doi: 10.1016/j.wear.2018.07.008.
- Olawale, D. O. *et al.* (2011) 'Progress in triboluminescence-based smart optical sensor system', *Journal of Luminescence*. Elsevier, 131(7), pp. 1407–1418.
- Palmgren, A. (1924) 'Die lebensdauer von kugellagern', *Zeitschrift des Vereines Duetscher Ingenieure*, 68(4), p. 339.
- Petersen, C. R. *et al.* (2021) 'Non-destructive subsurface inspection of marine and protective coatings using near-and mid-infrared optical coherence tomography', *Coatings*. MDPI, 11(8), p. 877.
- Prayogo, G. *et al.* (2011) 'Impact fatigue damage of GFRP materials due to repeated raindrop collisions', *Transactions of the Indian Institute of Metals*. Springer, 64(4), pp. 501–506.
- Pugh, K. *et al.* (2021) 'On analytical tools for assessing the raindrop erosion of wind turbine blades', *Renewable and Sustainable Energy Reviews*. Elsevier Ltd, 137(November 2020), p. 110611. doi: 10.1016/j.rser.2020.110611.
- Ranade, S. R. *et al.* (2014) 'A tapered bondline thickness double cantilever beam (DCB) specimen geometry for combinatorial fracture studies of adhesive bonds', *International Journal of Adhesion and Adhesives*. Elsevier, 55, pp. 155–160.
- Reimer, L. (2000) 'Scanning electron microscopy: physics of image formation and microanalysis'. IOP Publishing.
- Reincke, K., Grellmann, W. and Heinrich, G. (2006) 'Engineering fracture mechanics for crack toughness characterisation of elastomers', in *Fracture of Nano and Engineering Materials and Structures - Proceedings of the 16th European Conference of Fracture*, pp. 763–764. doi: 10.1007/1-4020-4972-2\_377.
- Requena, G. *et al.* (2009) 'Sub-micrometer synchrotron tomography of multiphase metals using Kirkpatrick–Baez optics', *Scripta Materialia*. Elsevier, 61(7), pp. 760–763.
- Robertson, R. M., Lobisser, R. J. and Stein, R. E. (1946) 'High speed rain abrasion of glass cloth laminates', *Industrial & Engineering Chemistry*. ACS Publications, 38(6), pp. 590–591.
- Russ, J. C. (2013) *Fundamentals of energy dispersive X-ray analysis: Butterworths monographs in materials*. Butterworth-Heinemann.
- Sasmita, F. *et al.* (2019) 'Study of Elastic Modulus Determination of Polymers with Ultrasonic Method', *Int. J. Adv. Sci. Eng. Inf. Technol*, 9, p. 874.
- SCHMITT, G. F. (1979) 'The subsonic rain erosion response of composite and honeycomb structures', *SAMPE Journal*, 15, pp. 6–13.
- Schmitt Jr, G. F. (1968) *Flight test-whirling arm correlation of rain erosion resistance of materials*. AIR FORCE MATERIALS LAB WRIGHT-PATTERSON AFB OH.
- Schmitt Jr, G. F. (1974) 'Rain droplet erosion mechanisms in transparent plastic materials', *NBS The*

*Role of Cavitation in Mech. Failures.*

Schroder, H. W. (1979) 'RAIN EROSION OF LIGHTNING PROTECTION COATINGS FOR CARBON FIBRE COMPOSITES'.

da Silva, L. F. M., Öchsner, A. and Adams, R. D. (2011) *Handbook of adhesion technology*. Springer.

Sinha, M. and Buckley, D. J. (2007) 'Acoustic properties of polymers', in *Physical properties of polymers handbook*. Springer, pp. 1021–1031.

Siviour, C. R. *et al.* (2005) 'The high strain rate compressive behaviour of polycarbonate and polyvinylidene difluoride', *Polymer*, 46(26), pp. 12546–12555. doi: 10.1016/j.polymer.2005.10.109.

Siviour, C. R. and Jordan, J. L. (2016) 'High Strain Rate Mechanics of Polymers: A Review', *Journal of Dynamic Behavior of Materials*. Springer International Publishing, 2(1), pp. 15–32. doi: 10.1007/s40870-016-0052-8.

Sørensen, B. F. (2002) 'Cohesive law and notch sensitivity of adhesive joints', *Acta Materialia*, 50(5), pp. 1053–1061. doi: 10.1016/S1359-6454(01)00404-9.

Standard, A. (2012) 'D3433-99: Standard Test Method for Fracture Strength in Cleavage of Adhesives in Bonded Metal Joints, ASTM International, West Conshohocken, PA'.

Tayfun, U. *et al.* (2017) 'Mechanical, electrical, and melt flow properties of polyurethane elastomer/surface-modified carbon nanotube composites', *Journal of Composite Materials*. SAGE Publications Sage UK: London, England, 51(14), pp. 1987–1996.

Tcharkhtchi, A. *et al.* (2014) 'Thermal aging effect on mechanical properties of polyurethane', *International Journal of Polymer Analysis and Characterization*. Taylor & Francis, 19(7), pp. 571–584.

Tobin, E. F. *et al.* (2011) 'Comparison of liquid impingement results from whirling arm and water-jet rain erosion test facilities', *Wear*. Elsevier, 271(9–10), pp. 2625–2631.

Tobin, E. F. *et al.* (2015) 'Surface topography parameters as a correlation factor for liquid droplet erosion test facilities', *Wear*. Elsevier, 328, pp. 318–328.

Tobin, E. F., Young, T. M. and Raps, D. (2012) 'Evaluation and correlation of inter-laboratory results from a rain erosion test campaign', in *Proceedings of 28th international congress of the aeronautical sciences*.

Uijlenhoet, R. (2001) 'Raindrop size distributions and radar reflectivity–rain rate relationships for radar hydrology', *Hydrology and Earth System Sciences*. Copernicus GmbH, 5(4), pp. 615–628.

Ulbrich, C. W. (1983) 'Natural variations in the analytical form of the raindrop size distribution', *Journal of climate and applied meteorology*. JSTOR, pp. 1764–1775.

Valeur, B. and Berberan-Santos, M. N. (2011) 'A brief history of fluorescence and phosphorescence before the emergence of quantum theory', *Journal of Chemical Education*. ACS Publications, 88(6), pp. 731–738.

Verma, A. S. *et al.* (2021) 'Minimum leading edge protection application length to combat rain-induced erosion of wind turbine blades', *Energies*, 14(6). doi: 10.3390/en14061629.

Villermaux, E. and Bossa, B. (2009) 'Single-drop fragmentation determines size distribution of raindrops', *Nature physics*. Nature Publishing Group, 5(9), pp. 697–702.

Wahl, N. E. (1965) *Investigation of the phenomena of rain erosion at subsonic and supersonic speeds*.

BELL AEROSYSTEMS CO BUFFALO NY.

Wang, C. *et al.* (2019) 'Recovering hidden sub-layers of repainted automotive paint by 3D optical coherence tomography', *Australian Journal of Forensic Sciences*. Taylor & Francis, 51(3), pp. 331–339.

Wen, M. and Dušek, K. (2017) *Protective Coatings*. Springer.

Whitehead, A. H. *et al.* (2011) 'Rain erosion characteristics of electrodeposited Ni–SiC metal-matrix composite layers', *Wear*. Elsevier, 270(9–10), pp. 695–702.

Williams, C. R. and Gage, K. S. (2009) 'Raindrop size distribution variability estimated using ensemble statistics', in *Annales geophysicae*. Copernicus GmbH, pp. 555–567.

Xie, F. *et al.* (2019) 'Degradation and stabilization of polyurethane elastomers', *Progress in Polymer Science*. Elsevier Ltd, 90, pp. 211–268. doi: 10.1016/j.progpolymsci.2018.12.003.

Xu, C. N. *et al.* (1999) 'Artificial skin to sense mechanical stress by visible light emission', *Applied Physics Letters*. American Institute of Physics, 74(9), pp. 1236–1238.

Zhang, J. *et al.* (2017) 'Non-destructive analysis of flake properties in automotive paints with full-field optical coherence tomography and 3D segmentation', *Optics Express*. Optica Publishing Group, 25(16), pp. 18614–18628.

Zhang, J. *et al.* (2021) 'Non-Destructive Evaluation of Coating Thickness Using Water Immersion Ultrasonic Testing', *Coatings*. MDPI, 11(11), p. 1421.

Zhang, N. *et al.* (2016) 'Characterization of automotive paint by optical coherence tomography', *Forensic science international*. Elsevier, 266, pp. 239–244.

Zhang, S. *et al.* (2015) 'Rain erosion of wind turbine blade coatings using discrete water jets: Effects of water cushioning, substrate geometry, impact distance, and coating properties', *Wear*. Elsevier, 328–329, pp. 140–148. doi: 10.1016/j.wear.2015.01.079.

Zhang, Z. *et al.* (2021) 'An experimental study of rain erosion effects on a hydro-/ice-phobic coating pertinent to Unmanned-Aerial-System (UAS) inflight icing mitigation', *Cold Regions Science and Technology*. Elsevier, 181, p. 103196.

Zhao, C. *et al.* (2021) 'Dynamic behavior of impact hardening elastomer: A flexible projectile material with unique rate-dependent performance', *Composites Part A: Applied Science and Manufacturing*. Elsevier Ltd, 143(August 2020), p. 106285. doi: 10.1016/j.compositesa.2021.106285.

Zhong, S. (2019) 'Progress in terahertz nondestructive testing: A review', *Frontiers of Mechanical Engineering*. Springer, 14(3), pp. 273–281.

Zorin, I. *et al.* (2018) 'Mid-infrared Fourier-domain optical coherence tomography with a pyroelectric linear array', *Optics express*. Optica Publishing Group, 26(25), pp. 33428–33439.